

# **Supersymmetry search using $Z^0$ bosons produced in neutralino decays at the ATLAS detector**

Front cover: simulated decay of supersymmetric particles in the ATLAS detector.

# **Supersymmetry search using $Z^0$ bosons produced in neutralino decays at the ATLAS detector**

EEN WETENSCHAPPELIJKE PROEVE OP HET GEBIED VAN  
NATUURWETENSCHAPPEN, WISKUNDE EN INFORMATICA

PROEFSCHRIFT

TER VERKRIJVING VAN DE GRAAD VAN DOCTOR  
AAN DE RADBOUD UNIVERSITEIT NIJMEGEN  
OP GEZAG VAN DE RECTOR MAGNIFICUS PROF. MR. S.C.J.J. KORTMANN,  
VOLGENS BESLUIT VAN HET COLLEGE VAN DECANEN  
IN HET OPENBAAR TE VERDEDIGEN OP MAANDAG 11 APRIL 2011  
OM 12.30 UUR PRECIES

DOOR

**Eric Jansen**

GEBOREN OP 21 JULI 1981  
TE ZEVENAAR

Promotor:	Prof. dr. N. de Groot
Manuscriptcommissie:	Prof. dr. A.N.J.J. Schellekens
	Prof. dr. R. Snellings
	Prof. dr. P.M. Watkins
	Dr. S. Caron
	Dr. I.B. van Vulpen
	Universiteit Utrecht
	University of Birmingham
	Universität Freiburg
	Universiteit van Amsterdam

ISBN: 978-90-9026080-8

The work described in this thesis is part of the research program of the National Institute for Subatomic Physics (Nikhef) in Amsterdam, the Netherlands. The author was financially supported by the Foundation for Fundamental Research on Matter (FOM).

# Contents

<b>1</b>	<b>Introduction</b>	<b>1</b>
<b>2</b>	<b>Theoretical background</b>	<b>5</b>
2.1	The Standard Model . . . . .	5
2.1.1	Quantum electrodynamics . . . . .	7
2.1.2	Electroweak sector . . . . .	8
2.1.3	Higgs mechanism . . . . .	9
2.2	Open issues . . . . .	12
2.3	Supersymmetry . . . . .	13
2.4	Minimal Supersymmetric Standard Model . . . . .	14
2.5	Minimal supergravity . . . . .	16
2.6	Higgs mass constraints in the MSSM . . . . .	20
<b>3</b>	<b>The LHC and the ATLAS experiment</b>	<b>21</b>
3.1	Large Hadron Collider . . . . .	21
3.2	Physics requirements . . . . .	23
3.3	Detector overview . . . . .	24
3.4	Inner detector . . . . .	27
3.4.1	Pixel detector . . . . .	28
3.4.2	Semiconductor tracker . . . . .	28
3.4.3	Transition radiation tracker . . . . .	29
3.5	Calorimeters . . . . .	31
3.5.1	Electromagnetic calorimeter . . . . .	32
3.5.2	Hadronic calorimeter . . . . .	33
3.5.3	Forward calorimeter . . . . .	33
3.6	Muon spectrometer . . . . .	34
3.6.1	Monitored drift tube chambers . . . . .	35
3.6.2	Cathode strip chambers . . . . .	36

3.6.3	Resistive plate chambers . . . . .	36
3.6.4	Thin gap chambers . . . . .	37
3.7	Trigger system . . . . .	37
<b>4</b>	<b>Offline software</b>	<b>39</b>
4.1	Athena framework overview . . . . .	39
4.2	Simulation . . . . .	41
4.3	Reconstruction . . . . .	42
4.3.1	Electrons and photons . . . . .	43
4.3.2	Muons . . . . .	44
4.3.3	Jets . . . . .	47
4.3.4	B-tagging . . . . .	50
4.3.5	Tau leptons . . . . .	51
4.3.6	Missing transverse energy . . . . .	51
4.4	Analysis frameworks . . . . .	54
<b>5</b>	<b>Atlantis event display</b>	<b>55</b>
5.1	Event display requirements . . . . .	56
5.2	Visualization methods . . . . .	57
5.3	Data oriented projections . . . . .	57
5.3.1	$Y/X$ and $\phi/\rho$ . . . . .	58
5.3.2	$\rho/Z$ and $X'/Z$ . . . . .	59
5.3.3	$\phi/Z$ . . . . .	61
5.3.4	V-Plot . . . . .	62
5.4	Interactive analysis . . . . .	65
5.4.1	Invariant mass calculation . . . . .	65
5.4.2	Vertex fitting . . . . .	66
5.4.3	Hit filtering . . . . .	67
5.5	Technical implementation . . . . .	68
5.5.1	Program structure . . . . .	68
5.5.2	Event data access . . . . .	70
5.6	Visualization of the first collisions at 7 TeV . . . . .	71
5.7	Conclusions and outlook . . . . .	76
<b>6</b>	<b>Search for supersymmetry using <math>Z^0</math> bosons</b>	<b>77</b>
6.1	Introduction . . . . .	77
6.2	Monte Carlo datasets . . . . .	78

6.3	Parameter space analysis . . . . .	80
6.4	Event selection . . . . .	82
6.5	Trigger efficiency . . . . .	83
6.6	Signal characteristics . . . . .	85
6.7	Counting method . . . . .	89
6.7.1	Cut optimization . . . . .	89
6.7.2	Systematic uncertainties . . . . .	90
6.7.3	Obtained significance . . . . .	93
6.8	Simultaneous background fit . . . . .	94
6.8.1	Irreducible backgrounds . . . . .	94
6.8.2	Data-driven background estimation . . . . .	94
6.8.3	Fitting procedure . . . . .	95
6.8.4	Systematic uncertainties . . . . .	99
6.8.5	Obtained significance . . . . .	101
6.9	Dependence on $\tan \beta$ . . . . .	101
6.10	Conclusions . . . . .	103
	<b>References</b>	<b>105</b>
	<b>Summary</b>	<b>113</b>
	<b>Samenvatting</b>	<b>117</b>
	<b>Curriculum vitae</b>	<b>121</b>



# Chapter 1

## Introduction

The fundamental questions about the origin and composition of the Universe have always intrigued people. Mankind has always felt a desire to describe and predict the surrounding world. In ancient Greece, philosophers already reasoned about matter being composed of smaller and indivisible elements. They referred to these elementary constituents as atoms (from atomos, Greek for indivisible). However, further progress on this idea did not occur until modern day chemistry started to develop in the late 18th century. The idea of the atom, until then purely philosophical, was adopted to explain chemical properties. This eventually led to the publication of the periodic table of the elements by Mendeleev in 1869. Not only did the periodic table reveal patterns in the chemical properties of elements, it could also predict the existence and properties of elements that had not yet been discovered. This made the periodic table one of the major achievements in science.

Nevertheless, the idea of atoms being indivisible was abandoned in 1897, when Thomson discovered the electron. Thomson showed that the cathode rays, discovered 30 years earlier, were actually composed of negatively charged particles. But more importantly, he discovered that these subatomic particles were the same regardless of what atom they originated from. Thomson postulated that these light electrons swirled around a uniformly distributed positive charge, much like planets around the sun.

About a decade later, Rutherford performed his famous gold foil experiment. He bombarded a thin gold foil with  $\alpha$ -rays, or Helium nuclei. The deflection pattern of the  $\alpha$ -rays that scattered from the gold atoms in the foil could not be explained by Thomson's model. The results indicated that the positively charged nucleus was not distributed uniformly at all, it was very small and concentrated in the center of the atom.

This image of the atom was further refined in 1932, when the study of isotopes led

to the discovery of the neutron and proton structure of the atomic nucleus. By then, also the theory of electron orbitals had developed to explain spectral patterns, leading to the present day picture of what we still, incorrectly, call the atom.

In the decades that followed, experimentalists discovered more and more new, unstable, particles: the muon, the pions, the kaons... By the 1960s, so many new particles had been found that people colloquially referred to them as the “particle zoo”. Nevertheless, careful categorization of all the species in this zoo is what eventually led to the discovery of the quarks. Initially, the quark model contained only three quarks: the flavors up, down and strange. A fourth quark, the charm, was added later to allow for a better description of the weak interaction. In 1973 the quarks of the third generation, the top and bottom, were introduced in order to explain  $CP$  violation [1].

The Standard Model in its current form originated in the 1960s, when the electromagnetic and weak interactions were combined [2, 3]. This was later followed by the incorporation of the Higgs mechanism into the theory. The model became widely accepted in 1983, when the  $W$  and  $Z$  bosons it predicted were found by the UA1 and UA2 experiments at CERN’s SPS collider [4–6].

Then in 1995, more than 20 years after it was introduced into the theory, the top quark was discovered by the DØ and CDF experiments at the Tevatron in Chicago [7, 8]. The third generation of the Standard Model was completed 5 years later, when the DONUT experiment discovered the  $\tau$  neutrino [9]. This left only one more particle that had not been observed experimentally: the Higgs boson.

The mass of the Higgs boson is a free parameter in the theory. As its decay modes are strongly mass dependent, the absence of a theoretical mass prediction makes the experimental discovery notoriously difficult. To date, the LEP collider at CERN has set a lower limit on the mass of  $114.4 \text{ GeV}/c^2$  [10] and the Tevatron has recently excluded the range of  $158\text{--}175 \text{ GeV}/c^2$  [11]. Precision fits to the electroweak data show that the preferred Higgs mass is low, likely close to the LEP exclusion [12].

While the Tevatron experiments are continuing their search, the LEP collider at CERN has made way for the Large Hadron Collider (LHC). After a successful startup in 2009 (and a not so successful one in 2008), the LHC is now gathering physics data at higher collision energies than ever before. The LHC should be able to provide a definitive answer on the existence of the Higgs particle, which has been in hiding ever since its theoretical conception in 1964.

Even though the Higgs boson is certainly a major motivation, it is by no means the only reason to study the LHC data. Once fully operational, this accelerator will provide collisions at more than seven times the center of mass energy of the current experiments.

With all the discoveries made at colliders in the past, it seems unthinkable that this vast new energy regime will not yield answers to open questions and possibly open up many new questions at the same time.

One of the new theories that could show itself at the LHC is supersymmetry. This theory, in its simplest form, predicts that the particles that have been observed so far must all have a supersymmetric partner particle. None of these particles have been observed yet, but the theory can provide elegant answers to some of the questions the Standard Model has left behind. The lightest supersymmetric particle can, for example, provide an explanation for the mysterious dark matter. Also, the extra particles that are introduced can facilitate a unification of the three fundamental coupling constants. In section 2.3, these subjects will be discussed in more detail.

This thesis will discuss the prospects for the discovery of supersymmetry using the ATLAS detector at the LHC. Chapter 2 provides an overview of the theoretical ideas behind the Standard Model and some of the open issues. It concludes with the introduction of the Minimal Supersymmetric Standard Model as a solution to some of these issues. Chapter 3 discusses the experimental setup; the operational parameters of the LHC accelerator as well as a detailed description of the ATLAS detector and its performance will be presented. Translating the detector measurements into concrete information about the particles that traversed the detector is the domain of the reconstruction software, which is described in chapter 4. Part of the ATLAS software, the Atlantis event display, will be reviewed in-depth in chapter 5. Chapter 6, finally, documents a method that uses the channel  $\tilde{\chi}_2^0 \rightarrow Z^0 \tilde{\chi}_1^0 \rightarrow \mu^+ \mu^- \tilde{\chi}_1^0$  to search for evidence of supersymmetry in ATLAS.



# Chapter 2

## Theoretical background

### 2.1 The Standard Model

The elementary particles and three of the four fundamental forces are described by the Standard Model (SM) of particle physics. This theory contains two types of particles: fermions and bosons. The half-integer spin fermions are the matter particles, while the integer-spin bosons mediate the fundamental forces. The forces that are described by the Standard Model are the strong interaction, the weak interaction and the electromagnetic interaction. The theory does not include the fourth fundamental force, gravity.

The Standard Model contains twelve fermions, organized in three generations. This organization is detailed in table 2.1. For every fermion there is also an anti-fermion. The anti-fermion has the same quantum numbers, but is oppositely charged. These anti-particles are denoted by a bar (e.g.  $\bar{u}$ ) or by explicitly writing the charge (e.g.  $e^+$ ).

**Table 2.1:** The three fermion generations in the Standard Model. The charge is given in units of absolute electron charge.

	Generation			Charge
	I	II	III	
Quarks	$u$ (up)	$c$ (charm)	$t$ (top)	+2/3
	$d$ (down)	$s$ (strange)	$b$ (bottom)	-1/3
Leptons	$\nu_e$ ( $e$ -neutrino)	$\nu_\mu$ ( $\mu$ -neutrino)	$\nu_\tau$ ( $\tau$ -neutrino)	0
	$e^-$ (electron)	$\mu^-$ (muon)	$\tau^-$ (tau)	-1

The fermions are divided into two groups. The quarks, that carry a color charge, interact via the strong interaction. There are three possible colors, denoted by red, green and blue. The anti-quarks carry an anti-color. The color confinement makes it impossible to isolate a single quark. Quarks are bound in color-neutral composite particles called hadrons. Hadrons can be composed of a quark and an anti-quark, which is called a meson, or three (anti-)quarks, called a baryon. In addition to color charge, quarks also carry a weak isospin and an electric charge. This means that they also interact via the weak and electromagnetic interaction. Leptons do not interact via the strong interaction. The charged electron, muon and tau leptons interact weakly and electromagnetically. The three neutrinos are electrically neutral and only interact via the weak interaction.

The particles in the different generations have similar properties, but their mass increases with generation number. All the ordinary matter is composed only of fermions of the first generation. The proton contains two up and one down quark and the neutron contains one up and two down quarks. Atoms are composed of protons, neutrons and electrons.

Interactions between the fermions are described by the exchange of a boson. These bosons are the eight massless gluons that mediate the strong force, the massive  $W^+$ ,  $W^-$  and  $Z^0$  bosons that mediate the weak force and the massless photon that mediates the electromagnetic force.

The Standard Model describes the elementary particles and forces in the mathematical framework of a gauge theory. A gauge theory is a type of quantum field theory where the dynamics of the system, characterized by the Lagrangian, are required to be invariant under local transformations that belong to the symmetry or gauge group of the theory. In the case of the Standard Model, the symmetry group is:

$$SU(3)_C \times SU(2)_L \times U(1)_Y.$$

Here, the subscript  $C$  denotes color and the  $SU(3)_C$  group corresponds to the strong nuclear force. The subscripts  $L$  and  $Y$  denote the weak isospin and weak hypercharge respectively. These two groups correspond to the electroweak part of the theory, which is a combination of the weak and electromagnetic forces.

This chapter will provide a brief overview of the Standard Model, some of the remaining issues and the possible solutions provided by supersymmetric extensions. A more in-depth treatment can be found in textbooks such as [13] or [14]. From this point onward, all quantities will be expressed in natural units; the speed of light and Planck's constant are set to unity,  $\hbar \equiv c \equiv 1$ .

### 2.1.1 Quantum electrodynamics

An instructive example of a gauge theory is the case of quantum electrodynamics (QED), describing the electromagnetic interaction. Requiring the Lagrangian to be invariant under the symmetry group of QED,  $U(1)_Q$ , inevitably leads to the introduction of the photon field.

The free Lagrangian for a fermion field  $\psi$  with mass  $m$  is given by:

$$\mathcal{L} = \bar{\psi} (i\gamma^\mu \partial_\mu - m) \psi, \quad (2.1)$$

with  $\bar{\psi}$  the conjugate of the field  $\psi$  and  $\gamma^\mu$  the Dirac matrices. These matrices are defined by the anticommutation relation:

$$\{\gamma^\mu, \gamma^\nu\} = 2g^{\mu\nu}, \quad (2.2)$$

where  $g^{\mu\nu}$  is the metric tensor.

The elements of the group  $U(1)_Q$  are phase rotations of the field  $\psi$ . When applying a local  $U(1)$  transformation, it transforms the terms in the Lagrangian according to:

$$\psi \rightarrow e^{ie\Lambda(x)} \psi, \quad (2.3a)$$

$$\partial_\mu \psi \rightarrow e^{ie\Lambda(x)} \partial_\mu \psi + ie \partial_\mu \Lambda(x) e^{ie\Lambda(x)} \psi. \quad (2.3b)$$

Since, for a local transformation, the rotation angle  $\Lambda$  is dependent on the position  $x$ , the second term in 2.3b does not vanish. To maintain an invariant Lagrangian, this extra term has to be canceled in some way. It turns out that such a cancelation can be achieved by the introduction of the covariant derivative,  $D_\mu$ , which contains an additional field  $A_\mu$ :

$$D_\mu \equiv \partial_\mu + ieA_\mu. \quad (2.4)$$

After replacing the normal derivative by the covariant derivative, a method which is known as minimal substitution, the terms in the Lagrangian transform according to:

$$\begin{aligned} (\partial_\mu + ieA_\mu)\psi &\rightarrow (\partial_\mu + ieA'_\mu)e^{ie\Lambda(x)}\psi \\ &= e^{ie\Lambda(x)} (\partial_\mu + ie(A'_\mu + \partial_\mu \Lambda(x)))\psi. \end{aligned} \quad (2.5)$$

Provided that the gauge field  $A_\mu$  transforms as:

$$A_\mu \rightarrow A'_\mu = A_\mu - \partial_\mu \Lambda(x), \quad (2.6)$$

the Lagrangian now has the desired invariance under local  $U(1)$  transformations.

After also adding a kinetic term for the new field  $A_\mu$ , the expression for the QED Lagrangian reads:

$$\mathcal{L}_{QED} = \bar{\psi} (i\gamma^\mu D_\mu - m) \psi - \frac{1}{4} F^{\mu\nu} F_{\mu\nu}, \quad (2.7)$$

with  $F_{\mu\nu}$  the field tensor, defined as:

$$F_{\mu\nu} = \partial_\mu A_\nu - \partial_\nu A_\mu. \quad (2.8)$$

A mass term for the gauge field cannot be added, since a term of the form  $m_A^2 A_\mu A^\mu$  would break the invariance of the Lagrangian again. The boson mediating the electromagnetic force, the photon, is massless.

The other gauge bosons in the Standard Model can be introduced in a similar way. The eight generators of the  $SU(3)_C$  symmetry, for example, give rise to eight massless gluons, the mediators of the strong nuclear force. Since  $SU(3)$  is a non-Abelian group, the gluons will also interact with each other. This leads to quantum chromodynamics (QCD).

### 2.1.2 Electroweak sector

The Glashow-Weinberg-Salam model [2, 3] unifies the weak interaction with quantum electrodynamics. This is referred to as the electroweak sector of the Standard Model, which is represented by the group  $SU(2)_L \times U(1)_Y$ . The previously discussed symmetry of quantum electrodynamics is a subgroup of the electroweak group,  $U(1)_Q \subset SU(2)_L \times U(1)_Y$ . The electric charge in the electroweak group is given by the Gell-Mann-Nishijima equation:

$$Q = T_3 + \frac{Y}{2}, \quad (2.9)$$

where  $T_3$  is the third component of the weak isospin and  $Y$  is the weak hypercharge.

Analogous to the case of quantum electrodynamics, imposing gauge invariance on the Lagrangian (and leaving out the strong interaction for now) leads to the covariant derivative:

$$D_\mu = \partial_\mu - \frac{1}{2} i g_2 \sigma^a W_\mu^a - \frac{1}{2} i g_1 B_\mu, \quad (2.10)$$

where the index  $a$  runs from 1 to 3 and the  $\sigma^a$  can be chosen equal to the Pauli spin matrices. This covariant derivative results in three gauge bosons  $W_\mu^a$  with a coupling constant  $g_2$  and one boson  $B_\mu$  with a coupling constant  $g_1$ .

The physical gauge bosons are linear combinations of the gauge fields, namely:

$$W_\mu^\pm = \frac{1}{\sqrt{2}} (W_\mu^1 \mp i W_\mu^2), \quad (2.11a)$$

$$Z_\mu^0 = \frac{1}{\sqrt{g_1^2 + g_2^2}} (g_2 W_\mu^3 - g_1 B_\mu) \equiv \cos \theta_w W_\mu^3 - \sin \theta_w B_\mu, \quad (2.11b)$$

$$A_\mu = \frac{1}{\sqrt{g_1^2 + g_2^2}} (g_1 W_\mu^3 + g_2 B_\mu) \equiv \sin \theta_w W_\mu^3 + \cos \theta_w B_\mu, \quad (2.11c)$$

leading to the  $W^+$ ,  $W^-$ ,  $Z^0$  bosons and the photon  $\gamma$  ( $A_\mu$ ). The parameter  $\theta_w$  introduced here is called the weak mixing angle or Weinberg angle.

**Table 2.2:** Quantum numbers of the electroweak chiral doublets and singlets.  $T$  is the weak isospin,  $T_3$  the third component of  $T$  and  $Y$  is the weak hypercharge.

			$T$	$T_3$	$Y$
Quarks	$\begin{pmatrix} u \\ d \end{pmatrix}_L$	$\begin{pmatrix} c \\ s \end{pmatrix}_L$	$\begin{pmatrix} t \\ b \end{pmatrix}_L$	1/2	$\begin{pmatrix} +1/2 \\ -1/2 \end{pmatrix}$
	$u_R$	$c_R$	$t_R$	0	0
	$d_R$	$s_R$	$b_R$	0	-2/3
Leptons	$\begin{pmatrix} \nu_e \\ e \end{pmatrix}_L$	$\begin{pmatrix} \nu_\mu \\ \mu \end{pmatrix}_L$	$\begin{pmatrix} \nu_\tau \\ \tau \end{pmatrix}_L$	1/2	$\begin{pmatrix} +1/2 \\ -1/2 \end{pmatrix}$
	$e_R$	$\mu_R$	$\tau_R$	0	-2

The weak interaction distinguishes between left- and right-handed particles. These two chirality states are defined by the projection operators  $P_L$  and  $P_R$  as:

$$P_L \psi = \frac{1}{2} (1 - \gamma^5) \psi \equiv \psi_L, \quad P_R \psi = \frac{1}{2} (1 + \gamma^5) \psi \equiv \psi_R. \quad (2.12)$$

The left-handed particles and the right-handed anti-particles form weak isospin doublets, while the right-handed particles and left-handed anti-particles are singlets and do not carry weak isospin. These chiral fermion doublets and singlets are listed in table 2.2. The weak interaction involves only the weak isospin doublets.

### 2.1.3 Higgs mechanism

As mentioned already for the case of quantum electrodynamics, adding a mass term for the gauge bosons to the Lagrangian is not possible without breaking gauge invariance.

However, the  $W$  and  $Z$  bosons are known to be massive, so something in the theory has to provide their mass. A possible solution is to let the  $W$  and  $Z$  bosons acquire their mass through spontaneous symmetry breaking. This method was independently invented by Peter Higgs [15–17], Brout-Englert [18] and Guralnik-Hagen-Kibble [19]. It is most commonly referred to as the Higgs mechanism.

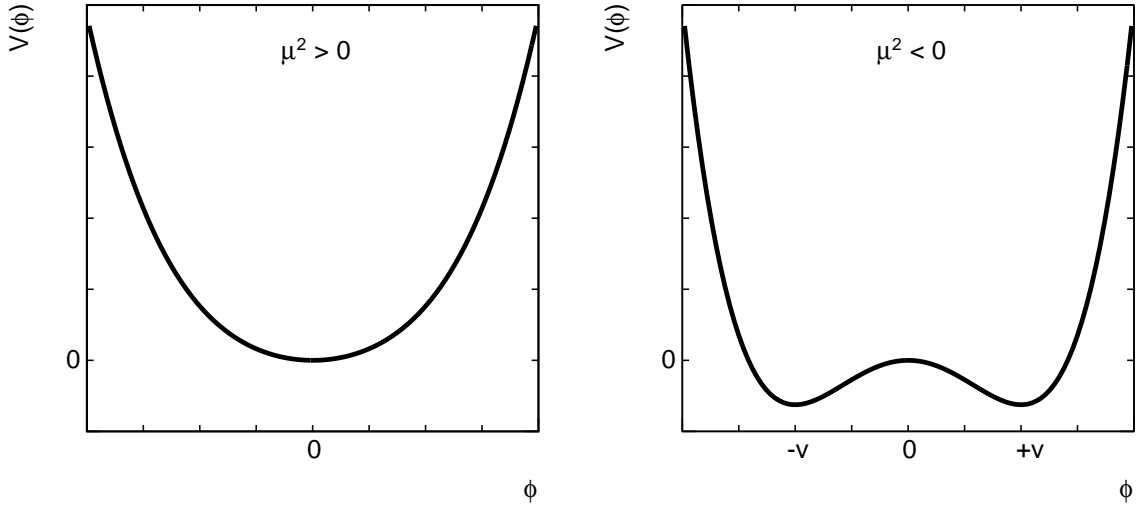


**Figure 2.1:** The Higgs potential for the cases of  $\mu^2 > 0$  and  $\mu^2 < 0$ .

Introducing the Higgs mechanism in the Standard Model requires the addition of a complex  $SU(2)_L$  doublet of scalar fields:

$$\Phi = \begin{pmatrix} \phi^+ \\ \phi^0 \end{pmatrix} = \frac{1}{\sqrt{2}} \begin{pmatrix} \phi_1 + i\phi_2 \\ \phi_3 + i\phi_4 \end{pmatrix}, \quad (2.13)$$

carrying weak hypercharge  $Y = +1$ . This field adds the following terms to the electroweak Lagrangian:

$$\mathcal{L}_H = |D_\mu \Phi|^2 - V(\Phi), \quad (2.14a)$$

$$V(\Phi) = \mu^2 |\Phi|^2 + \lambda |\Phi|^4, \quad (2.14b)$$

where  $V(\Phi)$  is the most general invariant expression for the potential. In order for the potential to be bounded from below, the parameter  $\lambda$  has to be positive. As a result, the potential has a simple parabolic shape around its minimum when  $\mu^2 > 0$ . However, for  $\mu^2 < 0$  the shape of the potential changes to something resembling a Mexican hat. This is shown in figure 2.1. In this case, the minimum of the potential is no longer at 0

and the field  $\phi^0$  obtains a vacuum expectation value:

$$\langle \Phi \rangle_0 \equiv \langle 0 | \Phi | 0 \rangle = \frac{1}{\sqrt{2}} \begin{pmatrix} 0 \\ v \end{pmatrix}, \quad \text{with} \quad v = \sqrt{-\frac{\mu^2}{\lambda}}. \quad (2.15)$$

The charged component,  $\phi^+$ , has to have a vacuum expectation value of 0 to preserve the  $U(1)_Q$  electromagnetic symmetry. Now, the simplest choice for a new ground state is  $\phi_1 = \phi_2 = \phi_4 = 0$  and  $\phi_3 = v$ . Expanding the field  $\Phi(x)$  around this point leads to:

$$\Phi(x) = \frac{1}{\sqrt{2}} \begin{pmatrix} 0 \\ v + H(x) \end{pmatrix}, \quad (2.16)$$

with the  $H(x)$  field corresponding to a new boson in the theory: the Higgs boson. Expanding the first term in the Lagrangian  $\mathcal{L}_H$  now results in the terms:

$$|D_\mu \Phi|^2 = \frac{v^2}{8} \left( g_2^2 (W_\mu^1)^2 + g_2^2 (W_\mu^2)^2 + (-g_2 W_\mu^3 + g_1 B_\mu)^2 \right) + \dots, \quad (2.17)$$

which correspond to the masses:

$$m_W = \frac{1}{2} g_2 v \quad (2.18a)$$

$$m_Z = \frac{1}{2} \sqrt{g_2^2 + g_1^2} v \quad (2.18b)$$

for the  $W^\pm$  and  $Z^0$  bosons respectively. The fourth gauge boson, the photon, remains massless. The Higgs boson itself is also massive, but the theory provides no prediction for its mass.

The fermions in the Standard Model can acquire mass via Yukawa couplings to the Higgs doublet field  $\Phi(x)$ . For this, the following terms can be added to the Lagrangian:

$$\mathcal{L}_f = -\lambda_e \bar{L} \Phi e_R - \lambda_d \bar{Q} \Phi d_R - \lambda_u \bar{Q} \bar{\Phi} u_R + \text{h.c.}, \quad (2.19)$$

where  $L$  and  $Q$  are the lepton and quark doublets of the first generation. Furthermore, the anti-fermions obtain their masses by adding the Hermitian conjugate (h.c.) of this expression to the Lagrangian. After spontaneous symmetry breaking, the fermions will then acquire the masses:

$$m_e = \frac{\lambda_e v}{\sqrt{2}}, \quad m_u = \frac{\lambda_u v}{\sqrt{2}}, \quad m_d = \frac{\lambda_d v}{\sqrt{2}}, \quad (2.20)$$

for the electron, the up quark and the down quark respectively. Analogously, mass terms can be generated for the other two generations of fermions.

At this point, the theory provides a mathematical framework that can successfully describe the fermions and the strong, weak and electromagnetic interactions between them.

## 2.2 Open issues

The Standard Model has proven to be an enormously successful theory that can provide very accurate predictions for many phenomena. Nevertheless, there are still some issues that it does not address. This does not imply that the theory is wrong in any way, but merely that the Standard Model is only a limiting case of a larger theory. Some of the arguments for theories beyond the Standard Model include:

- The model describes only three of the four fundamental forces of nature. Attempts to unite it with the fourth, gravity, have been unsuccessful so far.
- The three neutrinos in the Standard Model are assumed to be massless. However, from oscillation experiments [20] it is now known that their masses are not equal. Therefore at least two of the three neutrinos should have a nonzero mass.
- The theory contains many free parameters and there seems to be no deeper reason behind the values they have. The masses of the heaviest and the lightest quark differ by five orders of magnitude. When compared to the Planck scale, on the other hand, all the particle masses are essentially zero. This seems ad hoc and inelegant.
- Theoretical computations of the mass of a scalar particle include higher order corrections that might become arbitrarily large. Yet the Higgs boson is expected to have a mass below the TeV scale. The higher order corrections need to cancel each other very precisely for this to happen. The Standard Model provides no theoretical arguments why this would be the case.
- Cosmological measurements [21] have shown that the Standard Model only describes 4.4 % of the Universe. Another 21.4 % is composed of the so-called dark matter, matter that interacts gravitationally but is not observed otherwise. The remainder is some unknown form of energy, dark energy, responsible for the expansion of the Universe.

Many different theories for what lies beyond the Standard Model exist, ranging from simple extensions to address a single problem to exotic new theories that are orders of magnitude more complicated.

## 2.3 Supersymmetry

One of the more popular theories beyond the Standard Model is that of supersymmetry. The following sections will focus on the concepts and phenomenological consequences of supersymmetry. For an in-depth mathematical treatment, see for example [22–25].

Supersymmetry introduces a symmetry that relates bosonic and fermionic fields to each other. Much like the  $SU(2)$  doublets that group up- and down-type quarks, supersymmetry organizes fermions and bosons in supermultiplets. The Standard Model particles are paired with so-called superpartners, particles that have the same quantum numbers, but differ in spin by half a unit. A chiral doublet of quarks, for example, will be partnered with a set of scalars, or squarks. This immediately illustrates the nomenclature of supersymmetry. For bosonic superpartners the name of the Standard Model counterpart is prepended with an ‘s-’: squarks, sleptons, stop, smuon, etc. The fermionic superpartners are named by appending ‘-ino’ to the Standard Model name, for example the photino, the gluino and the Higgsino.

In the Standard Model, the interactions (approximately) conserve lepton and baryon number, which are defined by:

$$L = N_\ell - N_{\bar{\ell}}, \quad B = \frac{1}{3} (N_q - N_{\bar{q}}), \quad (2.21)$$

with the  $N$  denoting the number of leptons, anti-leptons, quarks and anti-quarks respectively. These conservation laws, for example, forbid the decay of the proton. When adding supersymmetry to the model,  $B$  and  $L$  are not conserved anymore, which would allow the proton to decay rapidly. However, measurements indicate that the lifetime of the proton is at least  $2.1 \cdot 10^{29}$  years [26], consistent with the approximate conservation of  $B$  and  $L$  in the Standard Model. In supersymmetric theories this situation is often resolved by introducing another conserved quantity: R-parity, which is defined as:

$$R_p = (-1)^{3B+L+2S}, \quad (2.22)$$

with  $S$  the spin of the particle. All Standard Model particles have  $R_p = +1$  and all supersymmetric particles have  $R_p = -1$ . Conservation of R-parity therefore implies that supersymmetric particles can only be produced in pairs and that they cannot decay into only Standard Model particles.

Since none of the Standard Model particles can be each other’s superpartner, the introduction of supersymmetry at least doubles the number of particles in the theory. Furthermore, since none of the supersymmetric partner particles have ever been observed, supersymmetry has to be a broken symmetry. Such breaking would make it

possible for the superpartners to have much higher masses than their Standard Model counterparts. This higher mass range could be accessible by the LHC, making supersymmetry an interesting new theory to search for.

Supersymmetry can provide plausible answers to some of the remaining questions in the Standard Model. For example, the conservation of R-parity implies that the lightest supersymmetric particle (LSP) cannot decay into any other particles. This means that the LSP has to be stable, making it a good candidate constituent for dark matter.

Furthermore, the superpartners result in additional higher order corrections to the Higgs mass. These additional terms are equal to those of their Standard Model counterparts, but have opposite sign. In this way, the large corrections are canceled and the Higgs mass remains naturally small.

Also a unification of the strong, weak and electromagnetic forces could be facilitated by supersymmetry. The energy scale dependence of these interactions is such that the coupling constants seem to approach each other at some higher energy scale. However, the coupling constants do not converge in a single point. It is argued that the almost-convergence is unlikely to be a coincidence, therefore something is needed to improve the convergence. The extra particles introduced by supersymmetry can provide this improvement. This is illustrated in figure 2.2, where the case of the Standard Model is compared with the Minimal Supersymmetric Standard Model. This model will be discussed in the next section.

## 2.4 Minimal Supersymmetric Standard Model

The Minimal Supersymmetric Standard Model (MSSM) is the smallest possible extension to the Standard Model that realizes supersymmetry. For every Standard Model particle, it adds one superpartner to the theory. Only in the Higgs sector the MSSM needs a few additional particles.

In the Standard Model, the down-type quarks obtain their mass by coupling to the Higgs field  $\Phi$ , while the up-type couples to the conjugate of the Higgs field  $\bar{\Phi}$ . In supersymmetric theories, this coupling with  $\bar{\Phi}$  is not allowed. This means that an extra doublet of Higgs particles is needed in the theory. This doublet has opposite hypercharge and couples to the up-type quarks. As a result of this extra doublet, supersymmetric models contain a total of five Higgs bosons. These are denoted by  $h^0$ ,  $H^0$ ,  $A^0$ ,  $H^-$  and  $H^+$ .

Except for the gluinos, the gaugino and Higgsino fields mix, resulting in mass eigenstates that are referred to as charginos and neutralinos. These mass eigenstates are

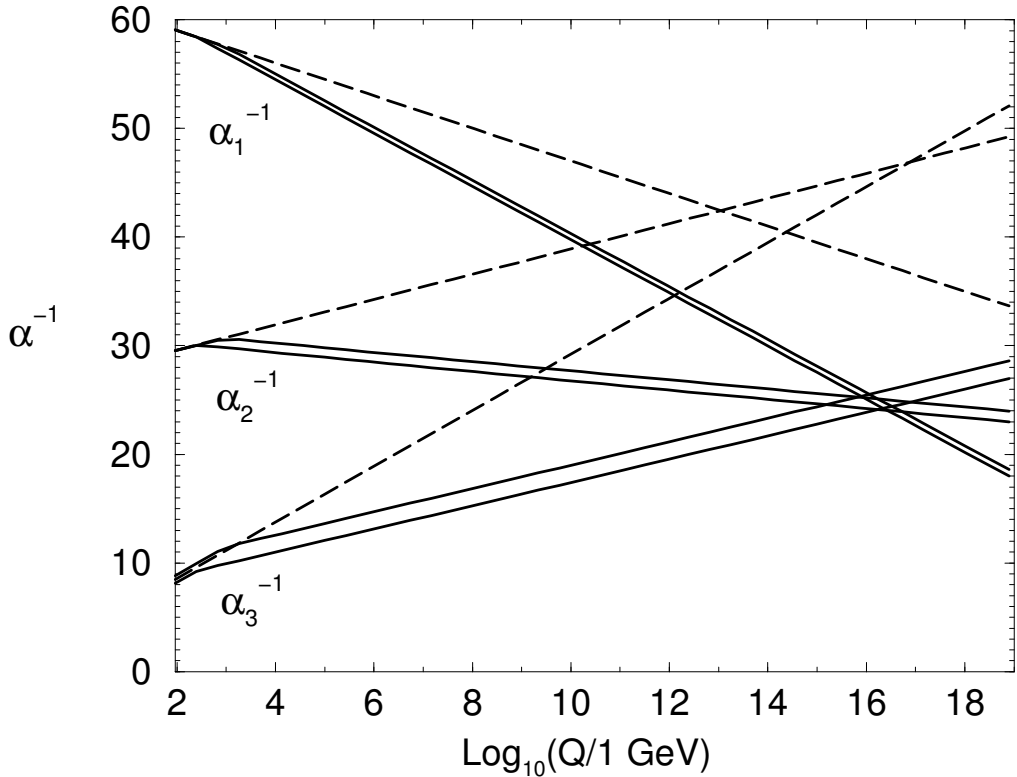


**Figure 2.2:** Running of the inverse of the electromagnetic, weak and strong coupling constants in the Standard Model (dashed) and the Minimal Supersymmetric Standard Model (solid). (Here the coupling constants are denoted by  $\alpha$  instead of  $g$ .) For the Minimal Supersymmetric Standard Model, the sparticle masses are varied between 250 GeV and 1 TeV. [24]

numbered in order of increasing mass. The two charginos,  $\tilde{\chi}_1^\pm$  and  $\tilde{\chi}_2^\pm$ , are a linear combination of a wino and a charged Higgsino. The neutralinos,  $\tilde{\chi}_1^0$ ,  $\tilde{\chi}_2^0$ ,  $\tilde{\chi}_3^0$  and  $\tilde{\chi}_4^0$ , are a linear combination of the photino, the zino and the neutral Higgsinos.

In supersymmetry, the masses of particles and their superpartners are equal. If this were the case, then the superpartners of the light fermions would have been discovered long ago. The fact that no experimental evidence has been found yet, means that supersymmetry has to be a broken symmetry. The mechanism for this breaking is not known, but it can be parameterized by adding the so-called soft breaking terms to the Lagrangian. The term soft refers to the fact that these terms break supersymmetry while at the same time preserving the basic properties of the theory. However, due to this parameterization, the minimal supersymmetric extension adds a total of 105 new parameters to the model. This severely limits the predictive power of the theory.

## 2.5 Minimal supergravity

In general, it is assumed that supersymmetry breaking originates in some hidden sector, containing only particles that interact very weakly with the Standard Model particles. The breaking is then propagated through radiative corrections. Several ideas exist about the source of this breaking. One of these ideas is a coupling to gravity, leading to supergravity.

In minimal supergravity (mSUGRA) it is argued that, since gravity is universal, many of the couplings and masses in the model converge at a higher energy scale. At the scale of this unification, only five free parameters remain:

- The unified mass of the scalars,  $m_0$ ;
- The unified mass of the gauginos,  $m_{1/2}$ ;
- The unified trilinear coupling constant,  $A_0$ ;
- The ratio of the vacuum expectation values of the two Higgs doublets,  $\tan \beta$ ;
- The sign of the coupling between the two Higgs fields, sign  $\mu$ .

The energy dependence of the parameters in the theory is governed by the renormalization group equations (RGE) [27]. Using the renormalization group equations, the mSUGRA parameters can be extrapolated from the unification scale back to the low energy spectrum. For example, the RGE evolution of the sparticle masses for one point in mSUGRA parameter space is shown in figure 2.3. Several programs [28–31] exist that can perform this evolution, transforming the five free parameters at the unification scale into a low energy spectrum that can be used to predict the mSUGRA phenomenology.

The strongest experimental constraint on supersymmetry is currently provided by measurements of the dark matter relic density. Assuming that the lightest supersymmetric particle is a dark matter constituent, the measured density provides an upper limit on the total neutralino mass in the Universe. This rules out many regions in parameter space that would result in dark matter relic densities that are much higher than the measured value of  $\Omega_c h^2 = 0.1123 \pm 0.0035$  [32].

The dark matter relic density constrains only the total neutralino mass, i.e. the number of LSPs times the mass of the LSP. As a result, there are two possible ways to satisfy this constraint: either the LSP has to be light, or the number of LSPs has to be low. Low-mass supersymmetry, which would yield an LSP which is light enough, is in many cases ruled out by existing experimental bounds. For example because the model

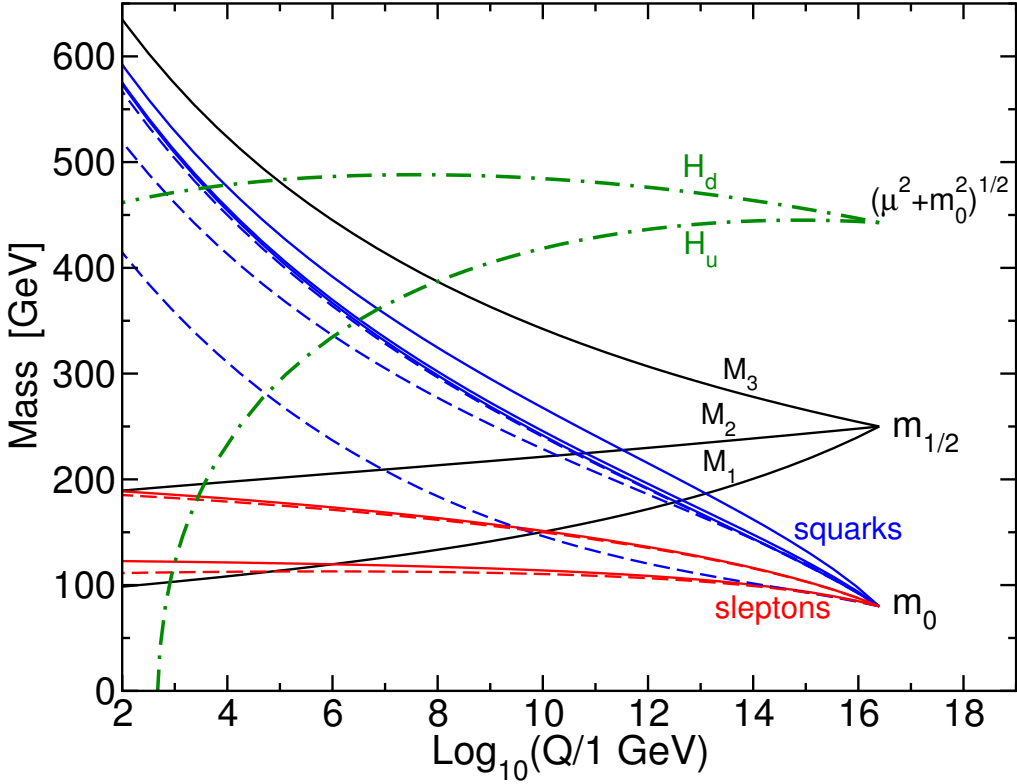


**Figure 2.3:** RGE evolution of the SUSY masses in the MSSM, when boundary conditions  $m_0 = 80 \text{ GeV}$ ,  $m_{1/2} = 250 \text{ GeV}$ ,  $A_0 = -500 \text{ GeV}$ ,  $\tan \beta = 10$  and  $\text{sign } \mu > 0$  are imposed at an energy scale  $Q_0 = 2.5 \cdot 10^{16} \text{ GeV}$ . [24]

contains a Higgs boson with a mass below the LEP exclusion. The number of LSPs in the Universe, on the other hand, is determined by the thermodynamics of the early Universe and their annihilation cross section. Even though conservation of R-parity forbids the decay of the LSP, it is still possible for the LSP to annihilate by interacting with another supersymmetric particle. The annihilation cross sections are determined by the model parameters. The different processes that can enhance the annihilation of the LSP therefore lead to a couple of preferred regions in parameter space, as shown in figure 2.4 [34, 35]:

**Focus point**, in the focus point region the  $\tilde{\chi}_1^0$  has a large Higgsino component, resulting in large cross sections for processes such as  $\tilde{\chi}_1^0 \tilde{\chi}_1^0 \rightarrow W^+ W^-$ .

**Coannihilation region**, here the mass of the lightest stau is close to the mass of the LSP, suppressing the decay  $\tilde{\tau} \rightarrow \tilde{\chi}_0^1 \tau$ . The coexistence of the LSP and the stau made it possible for them to annihilate in the early Universe. The cross section of

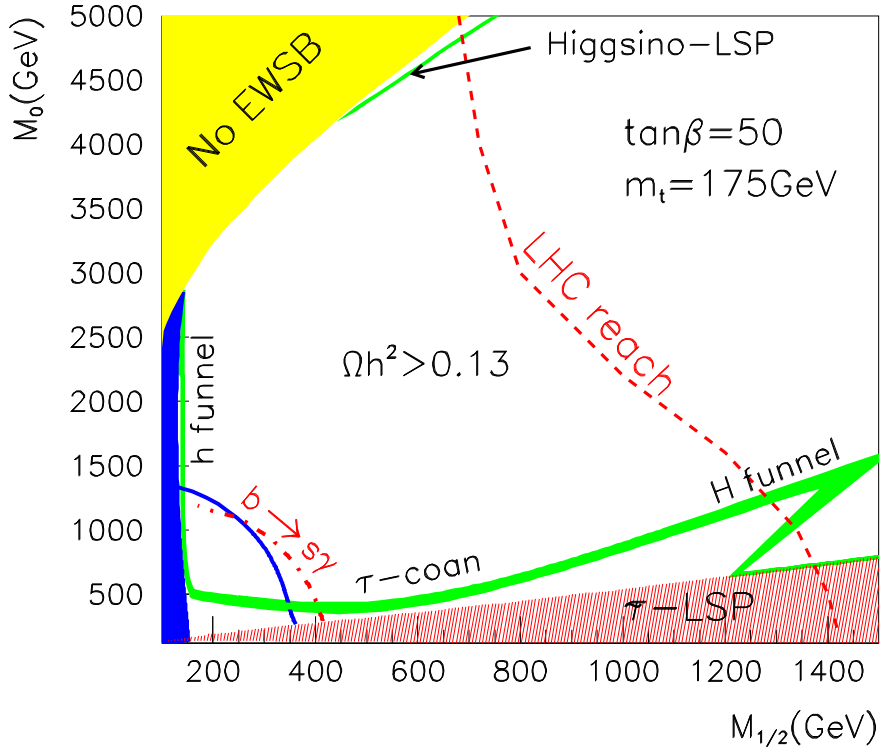


**Figure 2.4:** The  $m_0$ - $m_{1/2}$  plane for  $A_0 = 0$ ,  $\text{sign } \mu > 0$  and  $\tan \beta = 50$ . The region compatible with the dark matter relic density measurements is indicated by the green area, which shows the region where  $0.09 < \Omega_c h^2 < 0.13$ . The yellow region is excluded because there is no electroweak symmetry breaking, the blue region on the left is excluded because of direct searches at LEP and the red region in the bottom is excluded because the stau becomes the LSP. The Higgs mass limit of 114 GeV is indicated by the solid blue line. The red dash-dotted line is the exclusion from measurements of the  $b \rightarrow s\gamma$  branching ratio [33]. Also indicated in the plot is the LHC discovery reach for  $100 \text{ fb}^{-1}$ . Figure from [34].

this process is much higher than for neutralino-neutralino interactions, leading to a reduced number of LSPs.

**Funnel region,** in the funnel region the mass of the neutralino is such that a neutralino pair can efficiently annihilate through a resonance of another particle:  $2m_{\tilde{\chi}_1^0} \sim m_A, m_h, m_H$ .

**Bulk region,** in the bulk region both  $m_0$  and  $m_{1/2}$  are relatively low, resulting in many light sparticles. These light sparticles can enhance the annihilation cross section of the lightest neutralino.

Another experimental hint is provided by measurements of the anomalous magnetic moment of the muon,  $(g - 2)_\mu$ , which seems to slightly favor sign  $\mu > 0$  [35].

Even though the exact dependence of the mass spectrum on the mSUGRA parameters is far from trivial, some general effects can be observed in most regions in parameter space [36]:

- Increasing the gaugino mass,  $m_{1/2}$ , increases all the masses.
- Increasing the scalar mass,  $m_0$ , increases the masses of the squarks and sleptons. The parameter has very little effect on the masses of the gauginos and the lightest Higgs particle.
- Increasing the trilinear coupling constant,  $A_0$ , decreases the mass of the lightest Higgs boson  $h^0$ . When changing  $A_0$  over the range of  $\pm 1$  TeV,  $m_{h^0}$  can change by as much as 10 GeV. Furthermore,  $|A_0|$  has a decreasing effect on the mass of the third generation sfermions. This can lead to an additional region compatible with the dark matter relic density measurements due to stop coannihilation [37]. For moderate values of  $A_0$ , however, the effect on the mSUGRA phenomenology is limited.
- The parameter  $\tan \beta$  has little effect on the masses of the first two generations of sfermions and the gauginos. The masses of the third generation sfermions decrease with large  $\tan \beta$ . This also increases the mass splitting, especially for the  $\tilde{\tau}_1$  and  $\tilde{\tau}_2$ .
- The parameter sign  $\mu$  has relatively little effect on the mass spectrum. Because of this, the parameter is taken positive in most mSUGRA analyses, as this is favored by the  $(g - 2)_\mu$  measurements.

Since the mass spectrum determines the supersymmetric decays that are kinematically allowed, the above effects determine to a large extent the mSUGRA phenomenology. The most important influence on the phenomenology stems from the parameters  $m_0$  and  $m_{1/2}$ , followed by  $\tan \beta$ .

## 2.6 Higgs mass constraints in the MSSM

One common prediction among supersymmetric models is the presence of a relatively light Higgs boson, the  $h^0$ . In the Minimal Supersymmetric Standard Model, the mass of the  $h^0$  is constrained at tree-level by [38]:

$$m_h \leq \min(m_A, m_Z) \cdot |\cos(2\beta)| \leq m_Z,$$

with  $m_A$  the mass of the  $A^0$  Higgs boson,  $m_Z$  the mass of the Standard Model  $Z^0$  boson and  $\tan \beta$  the ratio of the vacuum expectation values of the two SUSY Higgs doublets. This means that at three-level, the  $h^0$  boson should be lighter than the  $Z^0$  boson. If this was the case, the MSSM would have been ruled out by the LEP Higgs limit of 114.4 GeV. Radiative corrections, however, can still increase the mass of the  $h^0$  by several tens of GeV's, bringing it back into agreement with the present exclusion limits. Nevertheless, this remains a very powerful constraint.

In order to provide an upper limit on the predicted mass of the  $h^0$ , scans of the MSSM parameter space have been performed to determine the absolute maximal value of the radiative corrections to the Higgs mass. For the unconstrained MSSM, this leads to an upper limit of [39]:

$$m_h < 152 \text{ GeV}.$$

In the constrained models, such as mSUGRA, the parameters that enter into the radiative corrections are not all independent. In the case of mSUGRA, this lowers the limit on the mass of the lightest Higgs boson to [39]:

$$m_h < 136 \text{ GeV}.$$

Therefore if the searches for the Higgs boson at the LHC and Tevatron exclude the mass region between 114.4 GeV and 136 GeV, this will effectively also exclude the mSUGRA model.

# Chapter 3

## The LHC and the ATLAS experiment

### 3.1 Large Hadron Collider

The Large Hadron Collider (LHC) [40] is a proton-proton collider at the CERN (European Organization for Nuclear Research) laboratory near Geneva, Switzerland. It was inaugurated in September 2008 and the first collisions took place at the end of 2009. LHC occupies the tunnel previously used for the LEP accelerator. This tunnel has a circumference of 26.7 km and lies at a depth varying between 45 and 170 m beneath the surface. Four detectors surround the interaction points along the accelerator, these belong to the ATLAS, CMS, LHCb and ALICE experiments.

As the LHC collides two proton beams, separate beam pipes are needed for the clockwise and anti-clockwise beam. Because of the limited amount of space available in the 3.7 m wide tunnel, installing two separate proton rings was not deemed feasible. It was opted to go for a design where two beam channels are contained in a single magnet assembly. Only near the interaction points, on the straight sections, the two beams share a common beam pipe. The bending of the protons is achieved by a total of 1232 superconducting dipole magnets, each about 15 m in length and capable of producing a magnetic field of up to 8.33 T.

The proton beams will consist of 2808 bunches, each containing  $10^{11}$  protons. The spacing between the bunches is only 25 ns, resulting in 40 million bunch crossings per second. Initially, the machine will operate at a luminosity of  $10^{32} \text{ cm}^{-2}\text{s}^{-1}$ . During this period an integrated luminosity of around  $1 \text{ fb}^{-1}$  per year is expected to be recorded. Later the luminosity will be increased to  $10^{34} \text{ cm}^{-2}\text{s}^{-1}$ , increasing the integrated lumi-

nosity to approximately  $100 \text{ fb}^{-1}$  per year.

When the LHC is operating at high luminosity, an average of 23 inelastic collisions is expected to occur at every bunch crossing. So for every selected event there will be a multitude of superimposed events, which are referred to as minimum bias or pileup events.

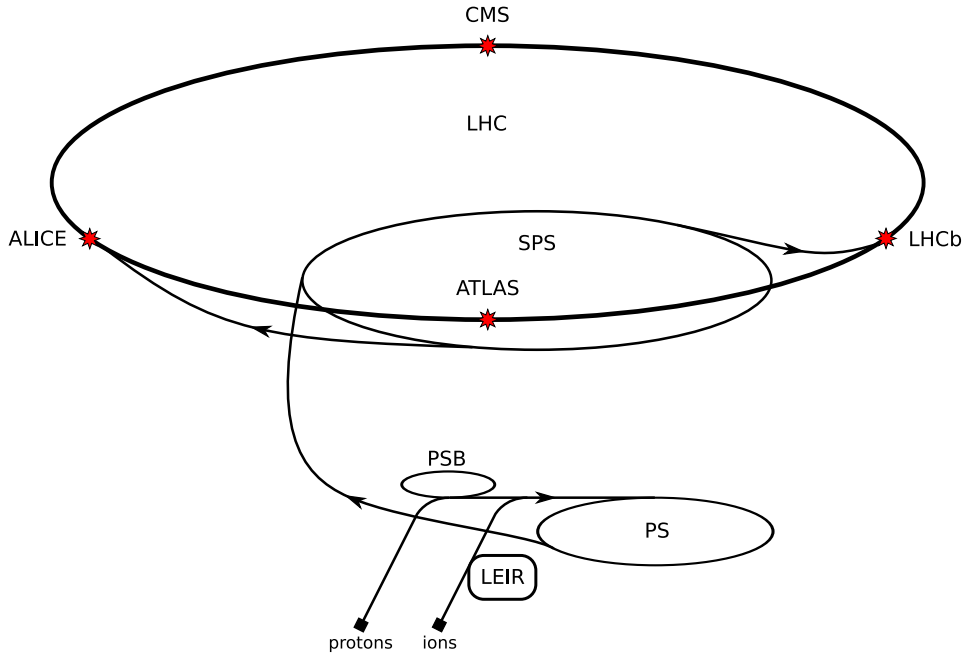


**Figure 3.1:** A schematic view of the CERN accelerator complex.

Figure 3.1 shows the layout of the CERN accelerator complex. Before being injected into the LHC, the protons traverse several other accelerators. The acceleration starts in a linear accelerator which delivers bunches of protons to the PS Booster (PSB) at an energy of 50 MeV. Here the energy is increased to 1.4 GeV before the protons are injected into the Proton Synchrotron (PS). The acceleration continues and at an energy of 26 GeV the beam is sent into the Super Proton Synchrotron (SPS). In the SPS the energy is increased further, until the LHC injection energy of 450 GeV is reached. At this energy the bunches are injected, clockwise and anti-clockwise, into the two beam pipes of the LHC. The LHC then accelerates the protons until they reach their final energy of 7 TeV.

The LHC can also accelerate ion beams, but they follow a slightly different path. The ion beams are injected from a separate linear accelerator into the Low Energy Ion Ring (LEIR), where the ions are grouped into bunches. The ions are then sent, via the PS and SPS, to the LHC. Their final energy in the LHC is 2.76 TeV per nucleon.

Two of the detectors, ATLAS [41] and CMS [42], are general purpose detectors. They are designed to provide, as much as possible, a full geometric coverage around the interaction point and are capable of measuring a very broad spectrum of physics processes. Their main focus will be to discover the elusive Higgs boson and establish its parameters, but they will also provide insight into a yet unknown energy regime where new physics is expected to be found.

The other LHC experiments are more focused on specific measurements. The LHCb experiment [43] uses a single arm spectrometer to study heavy flavor physics. It is dedicated to precision measurements of  $CP$  violation and rare decays of  $B$  hadrons.  $CP$  symmetry is the product of charge conjugation ( $C$ ), the exchange of particles and anti-particles, and parity inversion ( $P$ ), the exchange of left and right. This symmetry is known to be violated by certain Standard Model processes, but the level of violation is not enough to explain the observed asymmetry between matter and anti-matter in the Universe. LHCb will examine the possibilities for new sources of  $CP$  violation beyond the Standard Model.

Contrary to the other experiments, the interest of ALICE [44] lies in collisions of heavy ions instead of protons. Every year, the LHC will dedicate a few weeks to operating with beams of lead ions. Such heavy ion collisions will create a so-called quark-gluon plasma, a state in which the quarks are no longer confined. By studying the properties of this plasma, ALICE seeks to provide more insight into the physics of the strong interaction.

Finally, there are two small experiments located in the accelerator tunnel itself. The first is TOTEM [45], which will measure the total proton-proton cross section by looking at elastic proton scattering in the very forward direction at CMS. The other experiment is LHCf [46]. LHCf measures neutral particles in the forward direction at ATLAS for calibrating hadron interaction models used to describe extremely high energy cosmic rays.

In the remainder of this chapter a more in-depth description of the ATLAS detector and its performance will be given.

## 3.2 Physics requirements

The search for the Higgs boson has had a major influence on the design of the ATLAS detector. Depending on the Higgs mass, different decay channels will be used for its discovery. A dominant decay mode for the Higgs will be the decay into hadrons, but this decay alone will be very hard to detect because of the large QCD background.

Associated production, such as  $t\bar{t}H$ ,  $WH$  or  $ZH$ , where the decay of one of the top quarks or vector bosons produces a lepton, would provide a way to trigger on such an event and reject a significant portion of the background. Another method is to look for Higgs bosons produced by vector boson fusion, where the tagging of very forward jets is important. For a Higgs mass above approximately 130 GeV the decay into two  $Z$  bosons, which in turn decay into oppositely charged leptons, becomes important. This is one of the cleanest possible Higgs decay channels.

Searches for additional Higgs bosons, for example the  $A^0$  and  $H^\pm$  that are predicted by the minimal supersymmetric extension to the Standard Model, require good reconstruction of  $\tau$  leptons and good tagging of  $b$ -jets.

Other exotic new particles that could potentially be discovered at the LHC are the  $W'$  and  $Z'$ . These new heavy gauge bosons could have a mass of up to several TeV, hence their leptonic decays will involve very high  $p_T$  leptons [47].

Then there are also the decays of heavy supersymmetric particles. If R-parity is conserved these decays will produce a cascade of high momentum jets and leptons, eventually decaying into the stable lightest supersymmetric particle (LSP). The LSP will escape the detector unseen, thus causing a significant amount of missing transverse energy.

Being able to accurately measure the quantities of interest in all these processes, while being subjected to the high particle flux at the LHC, imposes very strict requirements on the detector. The ATLAS detector combines many different technologies in a layered design in order to obtain the required performance for all these measurements.

### 3.3 Detector overview

The ATLAS (A Toroidal LHC ApparatuS) detector [41] is a general purpose detector which was designed to make full use of the discovery potential of the LHC. An overview of the experimental site in Meyrin, Switzerland, is depicted in figure 3.2. The detector itself is located 100 m underground in the UX15 cavern. The detector is constructed in cylindrical layers around the beam axis, combined with discs perpendicular to the beam axis to fill the openings at both ends. These are referred to as the barrel and the endcaps, respectively. An illustration of the detector is shown in figure 3.3.

The first 1.15 m around the beam pipe is occupied by the inner detector, which is a tracking detector. It measures the trajectories of charged particles created in the collision. This detector is embedded in a homogeneous solenoidal magnetic field of 2 T. The bending of a trajectory in this field provides a measure for the momentum of a

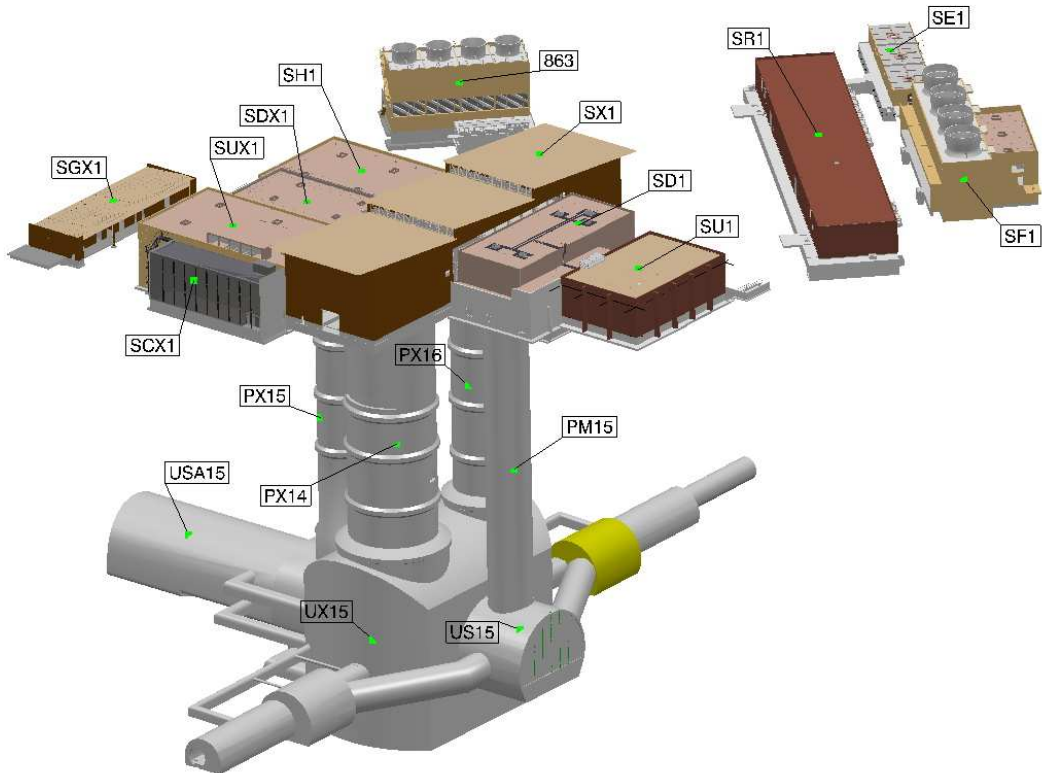


**Figure 3.2:** The ATLAS experimental site in Meyrin, Switzerland. A section of the LHC tunnel can be seen running from the bottom left to the top right of the picture. The detector is located in the UX15 cavern. Most of the readout electronics are located in the adjacent counting room and service cavern USA15. A total of four shafts connect the underground area to the surface buildings. These buildings house for example the control rooms (SCX1) and data acquisition computer farms (SDX1).

particle.

Situated directly outside the solenoid are the calorimeters. These are designed to measure the energy of charged and neutral particles coming from the collision. The calorimeters consist of an electromagnetic calorimeter on the inside, surrounded by a hadronic calorimeter. The barrel calorimeters extend up to a radius of 4.25 m.

The muon spectrometer forms the outer region of the detector. It consists of several layers of precision tracking chambers embedded in an air-core toroidal magnetic field with an average strength of 0.5 T in the barrel and 1.0 T in the endcaps. The bending of muons in this magnetic field will again provide a momentum measurement, but the distance traveled through the toroidal field is much larger. Since the momentum resolution is

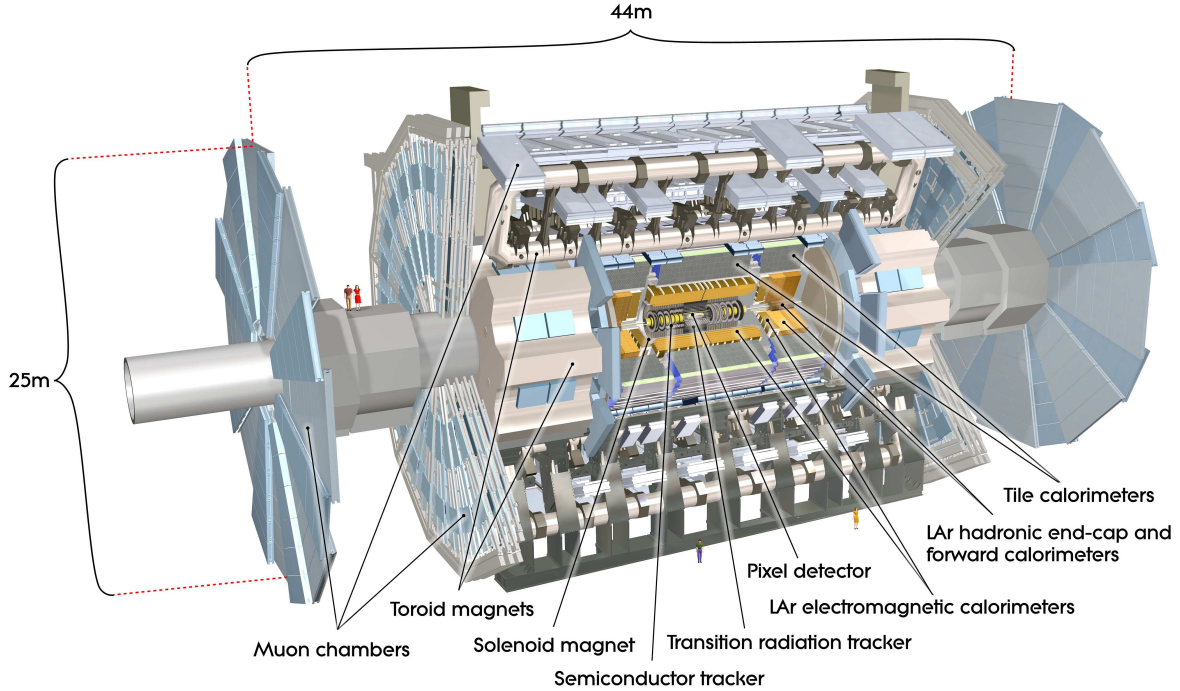


**Figure 3.3:** An illustration of the ATLAS detector, using a cut-away perspective view to show the different subdetectors.

proportional to the square of this distance, it significantly improves the momentum measurement for high momentum muons. In addition, the endcap toroids allow the momentum measurement of muons in the forward direction, beyond the acceptance of the inner detector.

The cylindrical geometry of the detector makes a description in cylindrical coordinates the most practical choice. The origin of the coordinate system is chosen as the nominal interaction point. The  $x$ -axis is defined as pointing to the center of the LHC ring, the  $y$ -axis is pointing upwards and the  $z$ -axis is pointing along the beam in the direction of LHCb. The radius  $\rho$  and azimuthal angle  $\phi$ , the angle with respect to the  $x$ -axis, are defined in the  $x$ - $y$  plane.

Usually, the event data itself is best described in spherical coordinates. In this case, the polar angle  $\theta$  is defined as the angle with the  $z$ -axis. Instead of  $\theta$  the pseudo-rapidity  $\eta$  is often used, which is defined as:

$$\eta = -\ln \left( \tan \left( \frac{\theta}{2} \right) \right) \quad (3.1)$$

where pseudo refers to the fact that in the limit of massless particles this approaches

the relativistic rapidity  $y$ :

$$y = \frac{1}{2} \ln \left( \frac{E + p_z}{E - p_z} \right). \quad (3.2)$$

The main benefit of using  $\eta$  instead of  $\theta$  is that the particle multiplicity as a function of  $\eta$  is approximately constant.

### 3.4 Inner detector

The tracking system has to cope with around a thousand tracks going through the central part of the detector at every bunch crossing. Achieving the required momentum and vertex resolution in such a very crowded environment requires high precision measurements with a very fine detector granularity. In ATLAS, this is provided by an inner detector consisting of pixel and silicon microstrip detectors in conjunction with a straw tracker. These are embedded in a 2 T homogeneous solenoidal magnetic field which provides the bending of charged particle trajectories. The layout of the inner detector is illustrated in figure 3.4.

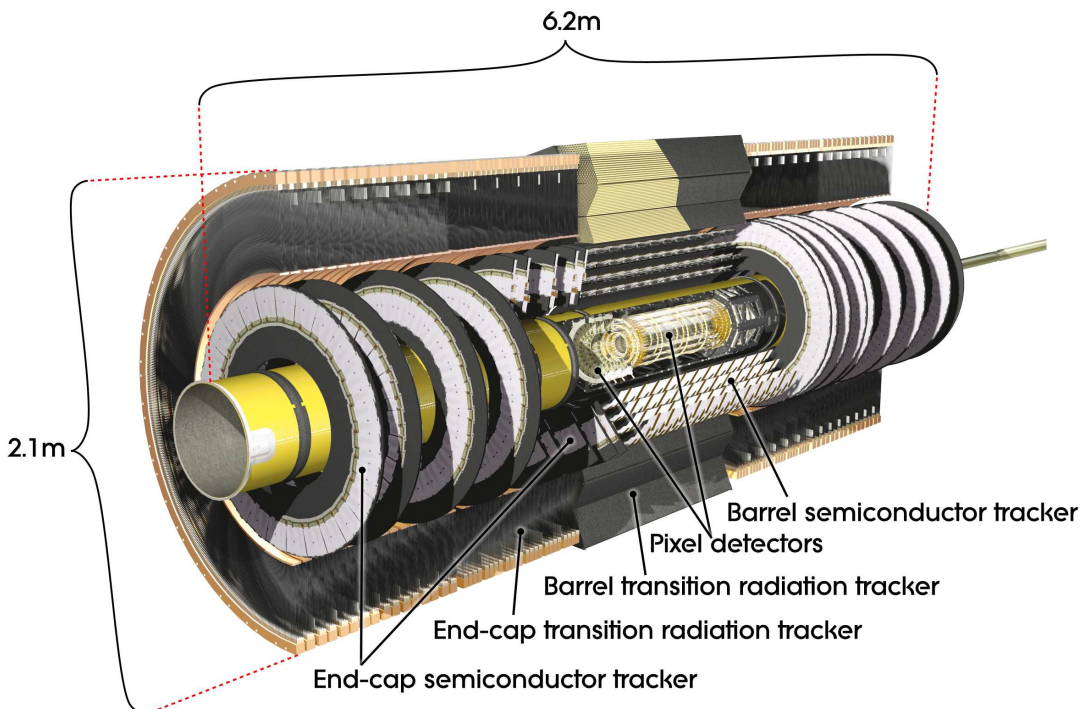


**Figure 3.4:** The ATLAS inner detector, showing the pixel, SCT and TRT detectors.

### 3.4.1 Pixel detector

High granularity tracking close to the interaction point is provided by the silicon pixel detector. This detector uses pixel sensors of  $50\text{ }\mu\text{m}$  by  $400\text{ }\mu\text{m}$  in size, providing an intrinsic accuracy of  $10\text{ }\mu\text{m}$  in the  $r\text{-}\phi$  plane and  $115\text{ }\mu\text{m}$  in the  $z$ -direction. The charge signal from a pixel sensor is amplified and compared to a programmable discriminator threshold in the front-end electronics. This digitized amplitude is then read out as the time over threshold.

The pixel sensors are arranged in three cylindrical layers, occupying the space between 5 and 25 cm from the beam axis. In either endcap region there are three layers of sensors perpendicular to the beam axis, making the total length of the detector about 1.3 m. The pixel detector provides about 80 million readout channels.

The high-radiation environment imposes strict requirements on the silicon sensors. The innermost layer of the pixel detector is removable and has to be replaced after approximately three years of running at design luminosity. The outer two layers must withstand a 1 MeV neutron equivalent fluence of up to  $F_{\text{neq}} = 8 \cdot 10^{14} \text{ cm}^{-2}$  over the ten year design lifetime of the experiment. In order to maintain an adequate noise performance after radiation damage, the silicon sensors are operated at a temperature between  $-5$  and  $-10^\circ \text{ C}$ .

### 3.4.2 Semiconductor tracker

The semiconductor tracker (SCT) is located outside the pixel detector and extends up to a radius of 55 cm from the beam axis. The SCT contains four layers of silicon strip sensors. These sensors are 6.4 cm long and positioned parallel to the beam axis at a pitch of  $80\text{ }\mu\text{m}$ . Every layer consists of two sets of strips which are at a 40 mrad stereo angle with respect to each other. By combining the measurements from the two sets of strips, the SCT can also provide a  $z$ -coordinate measurement. Space points in the SCT can be reconstructed with an accuracy of  $17\text{ }\mu\text{m}$  in the  $r\text{-}\phi$  plane and  $580\text{ }\mu\text{m}$  in the  $z$ -direction.

The endcap regions are covered by SCT discs perpendicular to the beam axis. In the endcaps, the sensors are arranged in the radial direction and the radial coordinate measurement is derived using the stereo angle. Nine of these discs are positioned on either side, bringing the total length of the SCT to 5.5 m.

The SCT uses a binary readout. The signals from the 1536 channels per module are amplified and passed through a tunable discriminator. The output is then serialized and read out using a redundant serial link. In total, the SCT barrel and endcap discs

provide approximately 6.3 million readout channels.

The SCT is much further away from the beam pipe than the pixel detector, but the inner layers must still be able to cope with a radiation dose of up to  $F_{\text{neq}} = 2 \cdot 10^{14} \text{ cm}^{-2}$ . In order to meet the performance requirements in this environment, the SCT is also operated at a temperature between  $-5$  and  $-10^\circ \text{C}$ . In order to maintain this temperature, an evaporative cooling system is adopted for both the pixel and SCT, which uses octafluoropropane ( $\text{C}_3\text{F}_8$ ) as the coolant. This coolant is non-flammable, electrically non-conductive, chemically inert in case of leaks and stable against the expected radiation doses. The liquid octafluoropropane is delivered to the detector at room temperature, where it enters into small-diameter capillaries and the pressure starts to fall. Emerging from the capillaries, the fluid starts to boil, lowering the temperature of the cooling structure that is connected to the detector modules. Using pneumatically-controlled valves, the pressure at the inlets and exhausts can be regulated, allowing to control the detector temperature. The outgoing fluid, generally at a temperature of  $-25^\circ \text{C}$ , is used to pre-cool the incoming fluid to maximize the cooling capacity. In order to avoid condensation on the pipes, the exhaust fluid is heated to room temperature before leaving the inner detector volume. The outer radius of the SCT is fitted with heater pads to keep the surrounding TRT at room temperature. A more rigorous treatment of the construction and commissioning of the SCT can be found in [48, 49].

### 3.4.3 Transition radiation tracker

The transition radiation tracker (TRT) occupies the volume between 55 cm and 1.10 m in radius and just as the SCT it is 5.5 m long. It was designed to provide a large number of hits at relatively low cost. In the barrel region the TRT uses straw tubes with a diameter of 4 mm and a length of 1.44 m, arranged parallel to the beam axis. The straws measure a drift radius in the  $r\text{-}\phi$  plane with an intrinsic accuracy of  $130 \mu\text{m}$ . The ambiguity that results from the radius measurement is later resolved by the pattern recognition software. The straws do not provide a measurement of the  $z$ -coordinate. In the endcap regions the straws are 37 cm long and point radially outwards, hence providing position measurements in only  $\phi$  and  $z$ . The 73 straw planes in the barrel and 160 straw planes in the endcaps provide a total of 351,000 readout channels. Typically, a track traversing the TRT produces 36 hits.

In addition to this, the volume between the straws in the barrel is filled with  $19 \mu\text{m}$  diameter polypropylene fibers, which stimulate the emission of transition radiation by electrons. Transition radiation is radiation produced by relativistic charged particles that cross between media with different dielectric properties. The radiation photons can

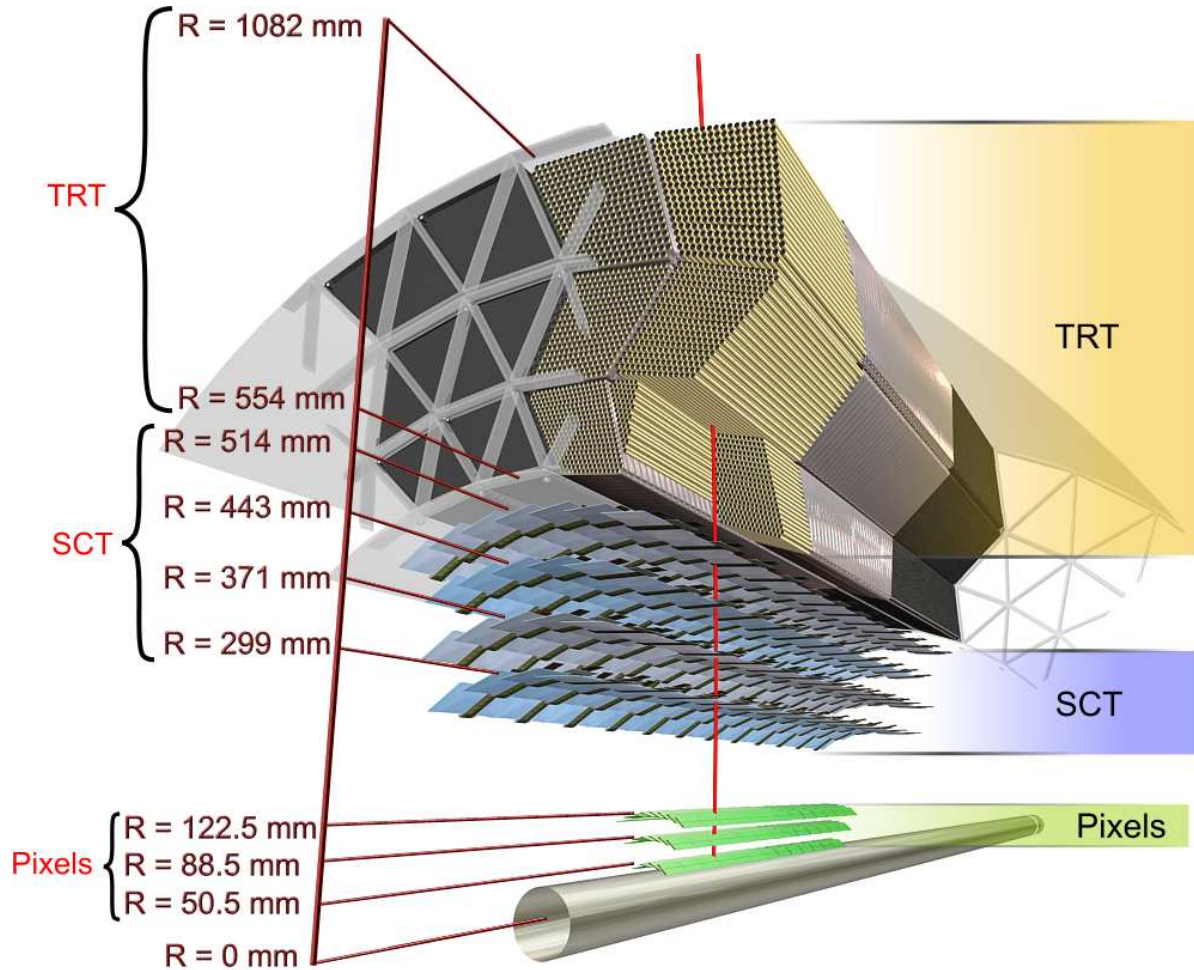


**Figure 3.5:** Illustration of a  $p_T = 10 \text{ GeV}$  track traversing the inner detector at  $\eta = 0.3$ .

be detected by the straws and are used to enhance electron identification. In the endcaps, the emission of transition radiation is achieved by adding a  $15 \mu\text{m}$  thick polypropylene foil in between the straw planes.

Figure 3.5 illustrates a  $p_T = 10 \text{ GeV}$  track passing through the inner detector, consecutively traversing three layers of pixel sensors, four layers of SCT sensors and the 73 TRT straw planes.

The performance requirements for the ATLAS inner detector are more stringent than for other tracking detectors built so far. The high detector granularity, electronics, readout services and the cooling system bring the weight of the inner detector to about 4.5 tonnes. Depending on  $\eta$ , the material can amount up to 2.5 radiation lengths or 0.7 interaction lengths. This poses additional complications for the reconstruction, since

this material needs to be carefully modeled and corrected for.

## 3.5 Calorimeters

The next layer of ATLAS consists of the calorimeters. In the  $\eta$  region corresponding to the inner detector, the electromagnetic calorimeter uses a very fine granularity for precision measurements of electrons and photons. The remainder of the calorimeter uses a more coarse granularity and covers the range up to  $|\eta| = 4.9$ . This ensures a good jet reconstruction and measurement of the transverse missing energy. The layout of the calorimeters is illustrated in figure 3.6 and a summary of the dimensions is given in table 3.1.

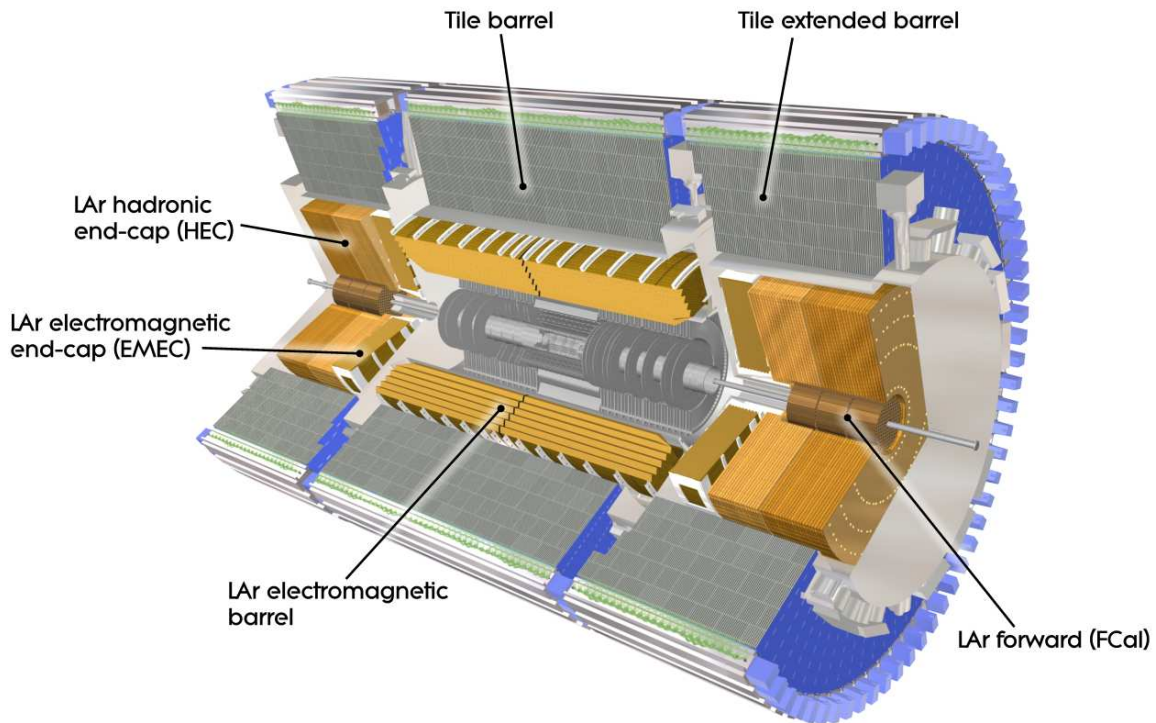


**Figure 3.6:** The ATLAS calorimeters, showing the location of the different calorimeter types with respect to the inner detector.

The calorimeters used in ATLAS are so-called sampling calorimeters. In such a calorimeter, a dense absorber material is interleaved with an active material for detection. The absorber material causes incoming particles to shower, these showers then produce a measurable signal in the active material. An important requirement for the calorimeter

is the containment of electromagnetic and hadronic showers with limited punch-through into the muon system.

**Table 3.1:** Dimensions of the ATLAS calorimeters [50, 51].

	$r$ (cm)	$z$ (cm)	$\eta$
EM barrel	$138 < r < 203$	$ z  < 340$	$ \eta  < 1.475$
EM endcap	$30 < r < 203$	$370 <  z  < 421$	$1.375 <  \eta  < 3.2$
Tile barrel	$228 < r < 425$	$ z  < 282$	$ \eta  < 1.0$
Tile ext. barrel	$228 < r < 425$	$320 <  z  < 611$	$0.8 <  \eta  < 1.7$
Hadronic endcap	$37 < r < 203$	$426 <  z  < 612$	$1.5 <  \eta  < 3.2$
Forward	$8 < r < 46$	$466 <  z  < 605$	$3.1 <  \eta  < 4.9$

### 3.5.1 Electromagnetic calorimeter

The liquid argon (LAr) electromagnetic (EM) calorimeter uses lead absorber plates and liquid argon as the active material. Particles traversing the liquid argon create charge by ionization, which is then collected on accordion shaped kapton electrodes. This accordion shape allows for a full coverage in  $\phi$  without any azimuthal cracks. The barrel part of the calorimeter extends up to  $|\eta| = 1.475$  and the endcap covers the region  $1.375 < |\eta| < 3.2$ . Both  $\Delta\eta$  and  $\Delta\phi$  range from 0.025 in the central region up to 0.1 in the forward direction. The thickness of the electromagnetic calorimeter corresponds to at least 22 radiation lengths in the barrel and at least 24 radiation lengths in the endcaps.

A thin layer of liquid argon calorimeter, the presampler, is placed in front of the main electromagnetic calorimeter to correct for energy lost in the support structure. The thickness of this layer is 1.1 cm in the barrel and 0.5 cm in the endcap region. It extends up to  $|\eta| = 1.8$ .

Based on measurements made in a testbeam setup, using electrons in the energy range of 20–250 GeV, the expected resolution of the electromagnetic calorimeter is [41]:

$$\frac{\sigma_E}{E} = \frac{(10.1 \pm 0.4)\%}{\sqrt{E(\text{GeV})}} \oplus (0.2 \pm 0.1)\%,$$

with first the stochastic term, representing fluctuations in the shower development, and

second the systematic term, representing non-uniformities in the calorimeter response. The noise level, with an uncertainty of  $\sigma_{\text{noise}} = 170 \text{ MeV}$ , has been subtracted.

### 3.5.2 Hadronic calorimeter

The hadronic calorimeter uses steel absorber plates interleaved with scintillating tiles as the active material. This calorimeter extends from 2.28 m to 4.25 m in radius and consists of three layers. The hadronic calorimeter uses a barrel section up to  $|\eta| = 1.0$  and two extended barrel sections covering the range  $0.8 < |\eta| < 1.7$  on either side. The calorimeter is divided into 64 azimuthal modules. By grouping readout fibers together, the tiles are combined in towers of  $\Delta\eta = 0.1$  in the first two and  $\Delta\eta = 0.2$  in the outer layer. The total thickness of the ATLAS calorimeter is 11 interaction lengths.

For the hadronic calorimeter the resolution has a significant dependence on  $\eta$ . Based on testbeam results, the expected energy resolution at  $\eta = 0.35$  is given by [41]:

$$\frac{\sigma_E}{E} = \frac{(56.4 \pm 0.4)\%}{\sqrt{E(\text{GeV})}} \oplus (5.5 \pm 0.1)\%.$$

The resolution of the calorimeter improves with increasing  $\eta$ , because of the increase in effective depth.

In the endcap region,  $1.5 < |\eta| < 3.2$ , hadronic calorimetry is provided by a liquid argon sampling calorimeter interleaved with copper plates. It consists of four layers divided into 32 azimuthal modules. The hadronic endcap calorimeter is located directly behind the electromagnetic endcap calorimeter, sharing the same cryostat vessel. From testbeam measurements, using pions with an energy up to 200 GeV, the resolution of the hadronic endcap calorimeter was found to be [41]:

$$\frac{\sigma_E}{E} = \frac{(70.6 \pm 1.5)\%}{\sqrt{E(\text{GeV})}} \oplus (5.8 \pm 0.2)\%.$$

### 3.5.3 Forward calorimeter

The coverage of the calorimeters is further extended up to  $|\eta| = 4.9$  by the forward calorimeter, positioned inside the hadronic endcap calorimeter. It shares its cryostat with both endcap calorimeters. The forward calorimeter is a liquid argon sampling calorimeter, segmented into three modules along the beam pipe. The innermost module is optimized for electromagnetic measurements, using copper as the absorber material, while the other two modules use tungsten absorbers and are designed to measure the energy of forward hadrons. The modules are approximately 45 cm long and consist of a

metal matrix with regularly spaced channels, aligned parallel to the beam axis. Inside these channels are metal rods that serve as the readout electrodes, with the gap between the rods and the matrix filled with liquid argon.

The resolution of the forward calorimeter was also measured in a testbeam setup [41]. For electrons, the measured energy resolution is:

$$\frac{\sigma_E}{E} = \frac{(28.5 \pm 1.0)\%}{\sqrt{E(\text{GeV})}} \oplus (3.5 \pm 0.1)\%$$

and for pions:

$$\frac{\sigma_E}{E} = \frac{(94.2 \pm 1.6)\%}{\sqrt{E(\text{GeV})}} \oplus (7.5 \pm 0.4)\%.$$

In this measurement, the energies were corrected from the electromagnetic to the hadronic scale using a single weight per module. The energy resolution for pions can be improved using radial weights, exploiting the fine transverse segmentation of the forward calorimeter. This reduces the stochastic term to  $70\%/\sqrt{E}$  and the systematic term to 5.8%.

## 3.6 Muon spectrometer

The muon spectrometer occupies the outer 5 m of the detector and is the largest of the detector systems. It uses large air-core toroids to provide a toroidal magnetic field with an average strength of 0.5 T. However, this field is not homogeneous and 1800 Hall sensors are placed throughout the muon spectrometer to provide an accurate map of the magnetic field.

Four different detector technologies are used in the muon system. Monitored drift tube chambers (MDT) and cathode strip chambers (CSC) provide precision measurements in the bending plane of the magnetic field. These are complemented by resistive plate chambers (RPC) and thin gap chambers (TGC) which function as trigger chambers and provide information on the coordinate perpendicular to the bending plane.

The layout of the muon system is illustrated in figure 3.7. The muon system is organized in three layers, referred to as the inner, middle and outer stations. In the barrel the stations are positioned at approximately 5 m, 7.5 m and 10 m from the beam axis. The endcap wheels are spaced apart a bit further and are located at roughly 7.5 m, 11 m and 21 m from the interaction point.

Muons with high momentum form an important component of new physics signatures. To be able to measure momenta of 1 TeV puts very stringent requirements on the precision of the muon detector. The bending of the trajectory of such a muon would

translate to a sagitta of only 500 µm. The design goal of a 10% momentum resolution therefore demands a measurement resolution of 50 µm.

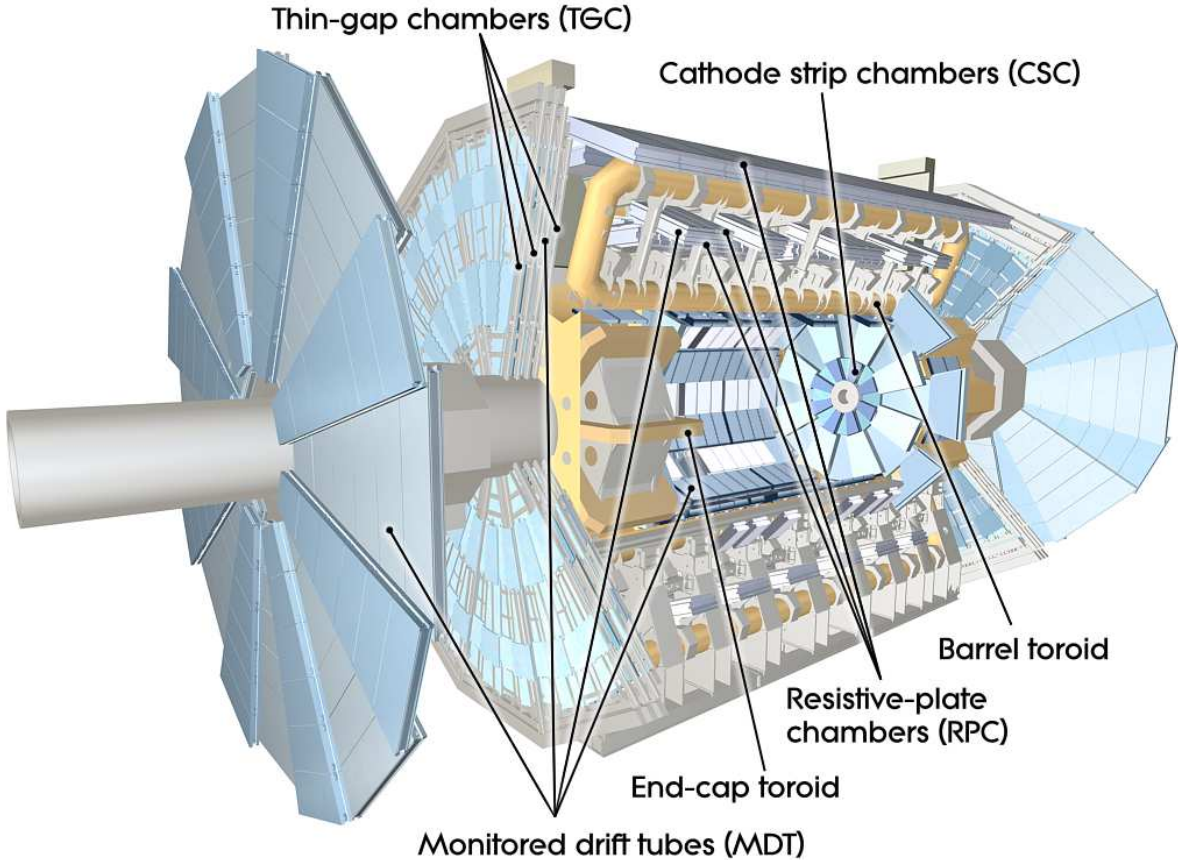


**Figure 3.7:** The ATLAS muon spectrometer. The inner detector and calorimeters have been hidden in order to show the position of the cathode strip chambers.

### 3.6.1 Monitored drift tube chambers

A monitored drift tube chamber (MDT) consists of a support frame with three or four layers of aluminum tubes on either side. The tubes are approximately 3 cm in diameter and vary in length between roughly 1 m and 5 m, depending on the chamber type. They are filled with a pressurized 93 % Ar and 7 % CO<sub>2</sub> gas mixture. In the center of the tubes is a tungsten-rhenium pickup wire at an electrical potential of 3 kV. This setup provides a gas gain of  $2 \times 10^4$ , but the drift times of the ionization electrons can range up to 700 ns. A single tube can measure a drift radius with an accuracy of 80 µm. This leads to a resolution of 35 µm for the six layer and 30 µm for the eight layer MDT chambers.

The tubes are oriented perpendicular to the  $\rho$ - $z$  plane, which is the bending plane of the toroidal magnetic field. MDT chambers cover the range up to  $|\eta| = 2.0$  in the inner station and up to  $|\eta| = 2.7$  in the middle and outer stations.

### 3.6.2 Cathode strip chambers

In the inner station, the coverage for  $2.0 < |\eta| < 2.7$  is provided by cathode strip chambers (CSC). Because of the long drift times, the MDT chambers would not be able to cope with the high counting rates in this region. A CSC is a multi-wire proportional chamber. The anode wires are pointing in the radial direction, while the cathode strips are parallel on one side and perpendicular to the anode wires on the other. This enables a CSC plane to measure both  $\phi$  and  $\eta$ . Electron drift times in the gas volume are less than 40 ns. Four CSC planes are used in either endcap. A cathode strip chamber provides measurements with a resolution of 40  $\mu\text{m}$  in the bending plane and 5 mm in the  $\phi$ -direction. The time resolution is 7 ns.

### 3.6.3 Resistive plate chambers

In the barrel region,  $|\eta| < 1.05$ , the triggering and  $\phi$ -coordinate measurement are provided by the resistive plate chambers (RPC). The basis of an RPC is formed by two thin phenolic-melaminic plastic laminate plates, separated by a 2 mm gas gap. The outer surface of the plates is covered with a layer of graphite paint followed by a layer of insulation. The graphite films are connected to a high voltage power supply to create a uniform electric field inside the gas gap. On the outside of this structure, insulated from the graphite layer, are the pick up strips. On one side these strips are oriented parallel to the MDT tubes (the longitudinal or  $\eta$  strips) and on the other side they are oriented perpendicular to the tubes (the transversal or  $\phi$  strips). Ionization charge accumulated on the plates can be detected by the capacitive effect on the pick up strips.

Two of these layers are clamped together to form a resistive plate chamber. The MDT chambers in the middle station are equipped with RPCs on both sides. This provides the triggering for low  $p_T$  muons. Also one side of the outer station is covered. In coincidence with the inner RPC layers, this provides the trigger for high  $p_T$  muons. The spatial resolution of an RPC is 10 mm and it provides a time resolution of 1.5 ns.

### 3.6.4 Thin gap chambers

In the endcap stations,  $1.05 < |\eta| < 2.7$ , triggering and measurement of the  $\phi$ -coordinate is done by thin gap chambers (TGC). The basic structure of a TGC consists of two plates covered with a graphite layer that functions as the cathode plane. Located in the middle of the gas gap is a series of anode wires oriented parallel to the MDT tubes. Two or three of these structures are bonded together to form a thin gap chamber. The  $\phi$ -coordinate measurement is provided by radial copper strips on the outer cathode planes. These strips measure the charge accumulation on the cathode plane using the capacitive effect, similar to the RPCs. The spatial resolution ranges from 2 to 6 mm in the radial and 3 to 7 mm in the azimuthal direction. The time resolution of a TGC is 4 ns.

## 3.7 Trigger system

Since bunch crossings at the LHC occur every 25 ns, events are produced 40 million times per second in ATLAS. At a size of approximately 1.3 MB per event it is obvious that only a very small fraction of the events can be stored. The trigger system is designed to make a very fast decision whether an event might contain interesting physics or not. On average only 1 in 200,000 events can be retained. This is complicated further by the fact that 25 ns are not enough to process or even read out the data from the detector. The readout systems use buffers to temporarily store data and processing the data has to be done in parallel. ATLAS uses a trigger design with three levels, referred to as level 1 (L1), level 2 (L2) and event filter (EF). Each level rejects a considerable fraction of the events. The reduced rate then allows the next level to use more time for a decision, enabling it to take more data into consideration.

At level 1 the trigger searches for leptons, photons and jets with high transverse momentum as well as large missing and total transverse energy. It uses the information from the calorimeters, but with a reduced granularity, combined with the trigger chambers in the muon spectrometer. Furthermore it defines so-called regions of interest, areas in the detector where interesting features have been found. To further reduce the event rate the trigger can also apply prescaling. In that case a fixed fraction of events passing a certain trigger is rejected, regardless of its properties. Analyses using such a prescaled trigger can incorporate this known reduction factor to calculate the total number of events passing the trigger. The level 1 trigger has been designed to make a decision in less than 2.5  $\mu$ s. It reduces the event rate to about 75 kHz.

The level 2 trigger is seeded by the regions of interest provided by the level 1 trigger. At level 2 all available detector data within these regions are used as input for the

decision. This means that about 2% of the total event data is read out at full granularity and precision. The event processing time at level 2 is about 40 ms. The output event rate is roughly 3.5 kHz.

The final stage in the trigger is the event filter. The events that were accepted by the level 2 trigger are sent to a processing farm where they are reconstructed by a slimmed down version of the offline reconstruction software. This step takes approximately 4 seconds per event. The events that are accepted by the event filter, about 200 per second, are written to permanent storage.

# Chapter 4

## Offline software

The ATLAS offline software is the part of the software concerned with processing the data after they have been recorded. Most of the offline software uses the Athena framework [52], which provides common services and interfaces to facilitate a modular design.

### 4.1 Athena framework overview

The Athena framework is written in the C++ programming language and is based on the GAUDI framework [53], which was originally developed for the LHCb experiment. The basis of Athena is formed by a series of classes from which the software in the framework inherits. These contain a basic level of functionality for a certain type of task. In this way, little code needs to be duplicated and the software developers can concentrate on implementing the physics algorithms. For a physicist, involved in reconstruction and analysis, the most important base classes are the following:

`Algorithm` provides the base for classes that will be run once per event to perform a specific task. The algorithms form the main ingredients of a reconstruction or analysis job, while being supported by the other two categories listed here. First, all algorithms will be initialized by calling their `initialize()` method; then they will be executed in the right order by calling the `execute()` method once per event; and when event processing is finished the `finalize()` method will be called to allow the algorithms to free any resources they have allocated.

`Service` provides functionality that might be required at any stage of the software execution. Classes inheriting from `Service` provide, for example, access to event data, geometry data or output histograms.

`AlgTool` is the base class for the “helper tools”. These lightweight tools are in general used multiple times per event and perform simple operations. They can be shared between multiple algorithms. `AlgTool` classes are used, for example, to build clusters from a group of silicon hits or to extrapolate tracks.

For practical reasons, the software within the Athena framework is divided into packages. Controlling a computing job and defining what packages need to be loaded is done using the job options. These are written in Python [54], an object oriented scripting language. The job options script sets the runtime parameters of the algorithms and defines which algorithms are to be run and in what order.

One of the most important services in Athena, and a vital element in its modular design, is StoreGate [55]. StoreGate provides software running within the framework with the ability to record objects into the so-called transient data store. Once recorded, other software can retrieve the objects again at a later stage.

Two transient data stores are available in Athena: the event store, which is retained for the duration of an event, and the detector store, which is retained for the entire job. As the name suggests, the event store is used for storing event data. In the track reconstruction for example, a segment finding algorithm would read hits from the event store and record the segments it finds. The segments would in turn be read by the track fitting algorithm, which continues the reconstruction by combining the segments into tracks. The detector store, on the other hand, contains objects such as the detector geometry and information needed for calibration. These objects are recorded during the initialization of the Athena job and will be the same for every event in a run.

Over the course of an Athena reconstruction job a variety of file formats is used. Most of these formats differ merely in the level of detail that is stored. For an end-user analysis only the following file types will be of interest:

**Event Summary Data (ESD)** files contain detailed output of the reconstruction.

The information content is such that particle identification, refitting of tracks or recalibration of jets can be done using the ESD as input. The target size for this file type is 500 kB per event.

**Analysis Object Data (AOD)** files can be produced from ESD files and contain only the information relevant for common analyses. Nevertheless, a back navigation mechanism is present that allows retrieval of certain information from the ESD while working on the AOD. The target size for an AOD file is 100 kB per event.

**Derived Physics Data (DPD)** is in principle the same as the AOD format, but with even more information removed to further reduce the event size. Information removal in DPD files is done by removing certain details from data objects, removing entire data objects or even removing full events from the AOD. DPD files are tailored towards specific analyses and no ATLAS-wide definition of their content exists.

## 4.2 Simulation

Simulation of proton-proton collisions is done in several steps and each of these can be done in many different ways [56]. A common approach is to start with a tree level matrix element generator, such as ALPGEN [57]. This type of generator will simulate the outcome of a collision by computing a tree level matrix element with a fixed number of outgoing partons. This is usually based on a direct computation of the relevant Feynman diagrams. The output of such a generator consists of bare quarks and gluons. Generators are usually optimized for specific processes, so different generators are used depending on the required final states.

The output of the initial event generator is interfaced with a program that performs showering and hadronization, such as PYTHIA [58], HERWIG [59] or ISAJET [28]. These programs use parton showers to incorporate higher order effects into the initial process. The initial partons are allowed to split into pairs of other partons, which are subsequently grouped into hadrons by the hadronization step. Matrix element generators that include next-to-leading order corrections also exist, making the showering step redundant. An example of such a generator is MC@NLO [60].

In the next step, the traversal of the generated particles through the detector is simulated. Using the GEANT4 [61] program, the particles are propagated through the magnetic field and detector materials. Meanwhile, their interactions with the materials, such as multiple scattering and photon conversions, are simulated. GEANT4 also simulates the decays of unstable particles.

The final step is to simulate the response of the detector to the generated particles. For this, the GEANT4 description of the detector geometry defines sensitive volumes, for example calorimeter cells or silicon strips. Whenever a simulated particle traverses such a volume, it will register a hit. The hits are then processed by a simulation of the detector electronics and collected. At this point, the normal event reconstruction can be performed. The simulated particles are retained in the event data for debugging and performance studies at a later stage.

Because the simulation of many particles is a very time consuming operation, simplifications have been made to speed up this process. The ATLFAST-II [62] simulation uses parametrized electromagnetic and hadronic calorimeter showers to model the energy deposit in the ATLAS calorimeters. The calorimeter simulation is the most CPU intensive part of the simulation. By using the parameterized showers, the CPU time needed for the calorimeter simulation can be reduced from several minutes to a few seconds [63]. For tracking in the inner detector as well as in the muon spectrometer, a full GEANT4 simulation is performed. The lower CPU time requirements of ATLFAST-II allow the simulation of larger data samples.

### 4.3 Reconstruction

Before track reconstruction in the inner detector can begin, the raw hits have to be processed. For the SCT this means that clusters of strips need to be built, which can be translated into three dimensional space points. Also the TRT hits have to be calibrated; the drift times have to be converted into drift radii that can be used to fit tracks.

The actual track finding can be done using different strategies. The default strategy uses seeds provided by space points in the pixel detector and the innermost layer of the SCT. The seed tracks are extended to pick up hits in the other layers of the SCT. The tracks are then fitted to form track candidates, followed by several quality cuts to reject fake tracks. The good tracks are extended further, through the TRT, where they are associated with TRT drift circles. This is followed by one more refit using all the hits from the pixel, SCT and TRT subdetectors.

To find tracks resulting from conversions or decays of long-lived particles, tracks that do not originate from the primary interaction region, back tracking is used to complement this strategy. In the case of back tracking, the reconstruction starts by finding segments in the TRT that are not yet associated to a track. These segments are then extended back into the SCT and pixel where they are associated to silicon space points and fitted.

After the track reconstruction is complete, the tracks are used to find the position of the primary vertex. When the primary vertex is found, tracks originating from a secondary vertex or conversion can be identified and the position of the secondary vertices can be fitted.

The next step in the reconstruction process is the combination of the particle trajectories found in the inner detector with information from the rest of the detector and the identification of particles and their properties.

### 4.3.1 Electrons and photons

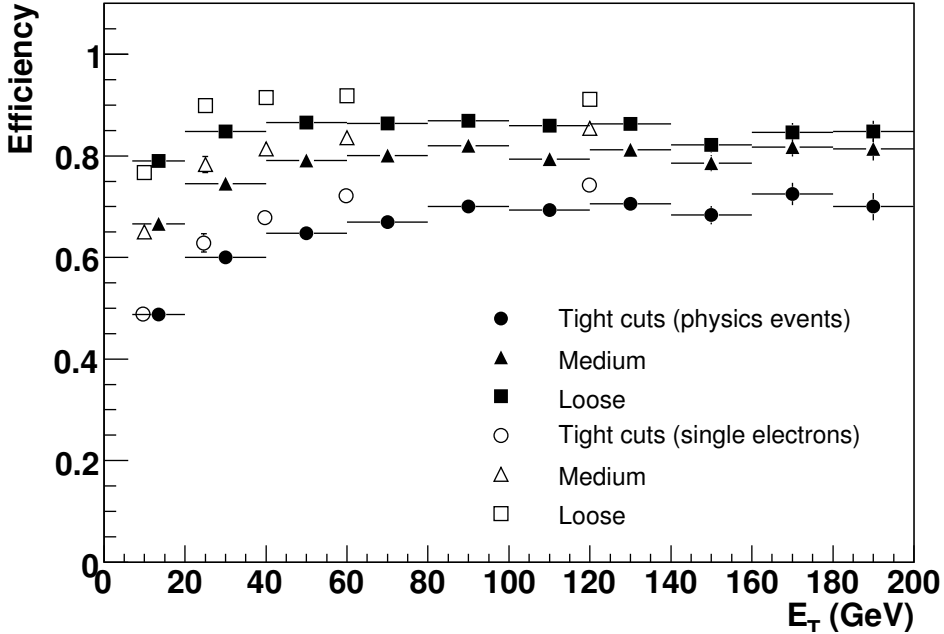


**Figure 4.1:** Reconstruction efficiency as a function of transverse energy for the three classes of electrons. This plot shows the efficiency obtained from Monte Carlo simulation of physics events (closed symbols) and single electrons (open symbols). [41]

Reconstruction of electrons and photons in ATLAS is quite challenging. Depending on  $\eta$ , electrons may have lost up to half of their energy when exiting the SCT. At that point also up to half of the photons has converted into an electron-positron pair. The TRT therefore plays an important role in the identification of electrons. The transition radiation photons produced in the TRT generate a much higher signal amplitude than charged particles. The amount of these high threshold TRT hits is used by the reconstruction software to refine the electron selection.

The search for electrons and photons starts by matching a cluster in the electromagnetic calorimeter to an inner detector track. Clusters that match a photon conversion in the inner detector are flagged as conversions. Electrons are then defined as clusters with an associated track but not flagged as a photon conversion, while photons are defined as clusters without an associated track.

For electrons, further selection is then carried out based on properties such as the longitudinal and lateral profile of the electromagnetic shower, the energy to momentum

ratio, the distance in  $\eta$  and  $\phi$  between the calorimeter cluster and the track and the ratio of high to low threshold hits in the TRT. Based on these properties, three classes of electrons are defined:

**Loose electrons** are electrons that pass simple cuts on longitudinal leakage and the shower shape in the middle layer of the electromagnetic calorimeter. Furthermore they require only a loose matching between the calorimeter cluster and the inner detector track.

**Medium electrons** also pass shower shape cuts in the first layer of the electromagnetic calorimeter. In addition to this, cuts are imposed on the quality of the associated reconstructed track.

**Tight electrons** have tighter cuts on the track matching and a cut on the energy to momentum ratio. Furthermore, they require a hit in the innermost layer of the pixel detector and a high ratio of high to low threshold TRT hits. Tight electrons can also include isolation cuts on the calorimeter cluster. These are referred to as tight isolated electrons.

The reconstruction efficiency for the different types of electrons is shown by the filled symbols in figure 4.1. The efficiency ranges from 50–70 % for tight electrons to 80–90 % for loose electrons, depending on  $E_T$ .

For photons, all information has to be derived from the calorimeter cluster. The fine granularity in  $\eta$  allows a determination of the  $\eta$ -direction of the photon by comparing the information in subsequent layers of the electromagnetic calorimeter. For determining the  $\phi$ -direction of the photon, the position of the primary vertex is taken as the point of origin.

### 4.3.2 Muons

ATLAS is capable of measuring muons with momenta ranging from around 3 GeV all the way up to 3 TeV. To achieve optimal performance over this large range, several complementary approaches to track reconstruction are used: a standalone reconstruction using only the muon spectrometer, a combined reconstruction using also the inner detector and the tagging of inner detector tracks using track segments found in the muon spectrometer [64] or using calorimeter information [65].

Before track reconstruction in the muon spectrometer can commence, the drift times in the MDT chambers have to be calibrated to determine the drift radii. Furthermore

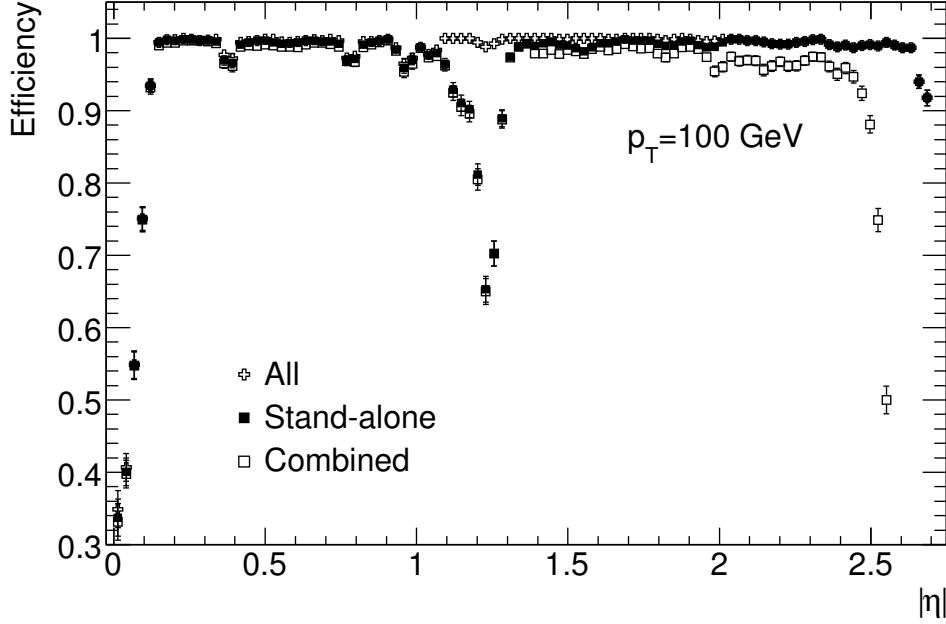


**Figure 4.2:** Muon reconstruction efficiency for a simulated  $p_T = 100 \text{ GeV}$  muon as a function of pseudorapidity. Muons reconstructed using only the muon spectrometer (standalone), the muon spectrometer and inner detector combined (combined) and muons reconstructed using any of the methods, including muon spectrometer based tagging (all) are shown separately. [41]

the raw hits in the other chambers have to be combined into clusters. These clusters have fully determined spatial coordinates.

In the first step of the track reconstruction, pattern recognition software reconstructs segments in the precision chambers. These segments are straight lines, fitted to the hits in a single chamber. The search for segments is seeded by the information in the trigger chambers, which also provide the  $\phi$ -coordinate measurement.

Starting from the outer and middle stations these segments are then extrapolated through the magnetic field and combined with segments in the other stations to form track candidates. In the final step the track candidates are refitted, taking into account the amount of material that is traversed and the detailed map of the magnetic field. At this point the reconstruction of standalone muon tracks is complete. A more detailed description of the pattern recognition and track finding algorithms used in the ATLAS muon spectrometer can be found in [66].

To create combined tracks, the tracks that were found are propagated from the inner muon station back to the interaction point, while being corrected for the energy lost in

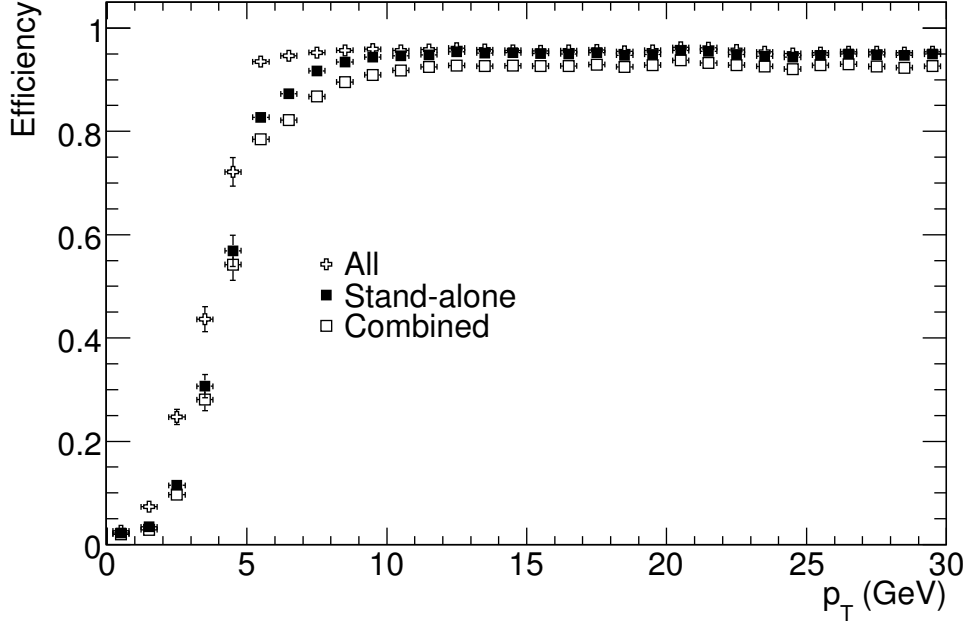


**Figure 4.3:** Monte Carlo muon reconstruction efficiency as a function of transverse momentum. Muons reconstructed using only the muon spectrometer (standalone), the muon spectrometer and inner detector combined (combined) and muons reconstructed using any of the methods, including muon spectrometer based tagging (all) are shown separately. [41]

the calorimeters and inner detector. In the region corresponding to the inner detector acceptance ( $|\eta| < 2.5$ ), a matching will be performed between muon and inner detector tracks. This improves the momentum resolution for low momentum tracks and reduces the background of muons from pion and kaon decays.

For the tagging methods, the inner detector tracks are extrapolated and matched to calorimeter clusters or muon segments. The tagging methods form an important complement to the normal reconstruction in situations where a muon does not (fully) traverse the muon system. This can occur for muons with low momentum, but also in regions where there are gaps in the detector coverage because of cabling or support structures.

Figure 4.2 shows the reconstruction efficiency for a  $p_T = 100$  GeV muon as a function of pseudorapidity. The improvement provided by the tagging methods can be clearly seen for low  $p_T$  muons and muons in the pseudorapidity region  $1.1 < |\eta| < 1.3$ . The figure does not include the calorimeter based muon tagging, which can provide an additional improvement of the efficiency for low values of  $|\eta|$  [65]. The  $p_T$  dependence of the

efficiency is illustrated in figure 4.3.

### 4.3.3 Jets

A schematic overview of the jet reconstruction and calibration is shown in figure 4.4. The first step in jet reconstruction is translating the energy deposits in the calorimeter cells into four-momentum vectors that can be used by the jet finding algorithms. This can be done in two ways, either by building signal towers or by topological cell clustering.

The method of signal tower building creates a grid in  $\eta$  and  $\phi$  with bin sizes of  $\Delta\eta \times \Delta\phi = 0.1 \times 0.1$ . The energy deposits in the cells are then summed in the corresponding bins. For cells that span multiple bins, a fraction of the energy deposit is counted, proportional to the overlap with the bin. The bins, or towers, are created from the raw cell energies which might have negative values due to noise. Whenever a tower has a negative energy content it will be combined with a neighboring tower to create a new tower with a net positive energy. These towers are also called protojets. No further combination is done at this stage. All towers are translated into four-momentum vectors which serve as input for the jet finding algorithms.

The second method, topological cell clustering, aims to reconstruct the energy deposits in three dimensions. This method uses three cell energy threshold values. Cells with an energy above the highest threshold are considered a cluster seed. All cells neighboring the cluster seed (in three dimensions) are then considered and added to the cluster if their energy is above the middle threshold. These cells are referred to as secondary seeds. The search continues with the neighbors of the secondary seeds and, if any were found, their neighbors. The search ends when no more secondary seeds exist around the cluster. The procedure then finishes by adding cells that neighbor a secondary seed and have an energy above the lowest threshold to the cluster. After the cluster has been found it is checked for local maximums and split if any are found. Just as with the signal tower method the clusters are translated into four-momentum vectors.

For jet finding there are also several algorithms available in ATLAS. The most commonly used are the fixed cone and  $k_T$  algorithms. These will be discussed here briefly.

The fixed cone jet finder is an iterative algorithm that starts from the input object with the highest  $p_T$ . This object is used as the seed. A cone of fixed radius  $R_{\text{cone}}$  is constructed around it in the  $\eta\text{-}\phi$  plane. Every object inside the cone, with  $\Delta R = \sqrt{\Delta\eta^2 + \Delta\phi^2} < R_{\text{cone}}$  is added to the seed. The combined four-momentum of the objects in the cone is then calculated and the search is repeated using this new momentum four-vector as the seed. The procedure stops when the four-momentum converges. Once the

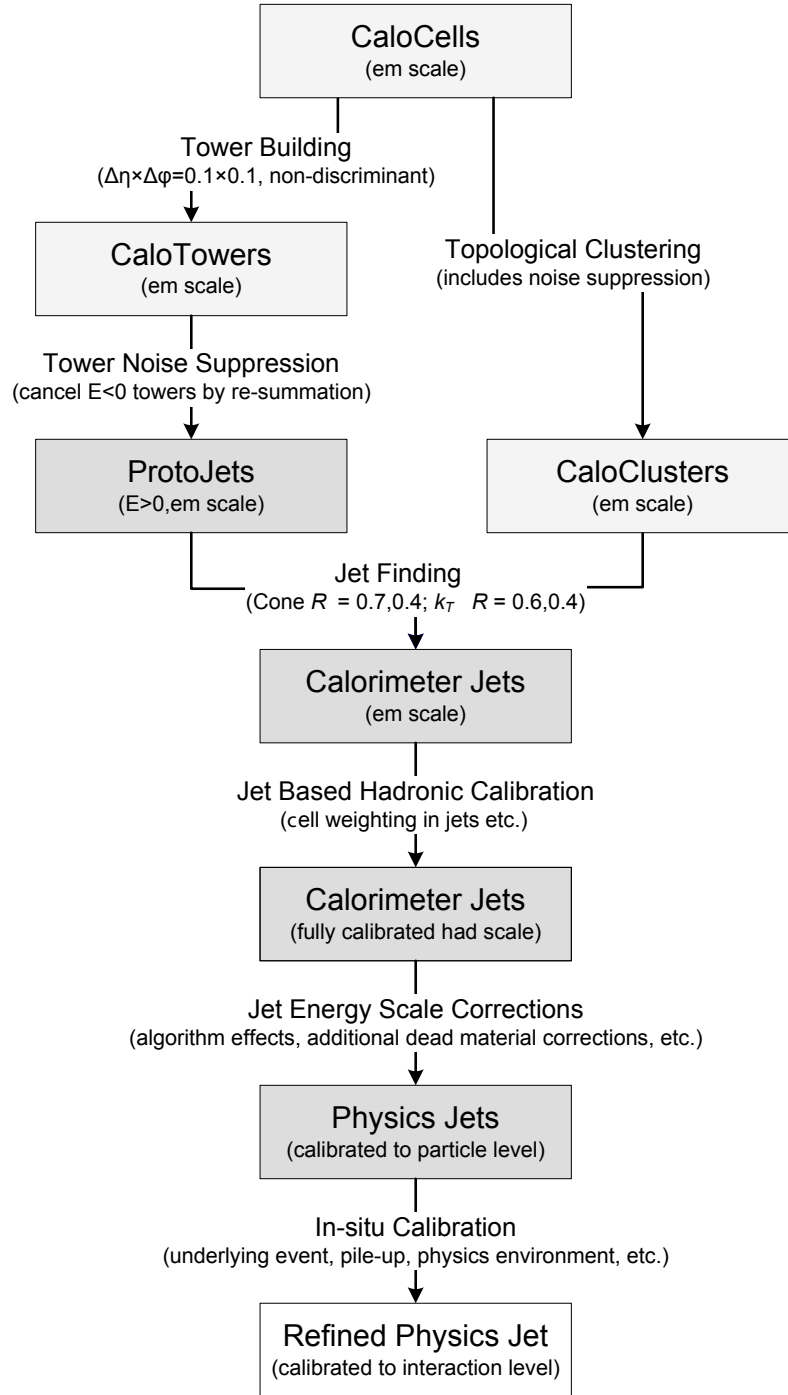


**Figure 4.4:** Flow chart of the jet reconstruction process, leading from energy deposits in the calorimeter cells to refined physics jets [41].

first jet is found, the algorithm takes the next highest  $p_T$  input object as the seed and starts again, until there are no more input objects above a certain  $p_T$  threshold left. In the final step, jets that share constituents which amount to more than half of their  $p_T$  are merged to form a larger jet. In the ATLAS cone jet finder the seed  $p_T$  threshold is 1 GeV and two cone sizes are used:  $R_{\text{cone}} = 0.4$  for narrow and  $R_{\text{cone}} = 0.7$  for wide cone jets.

The  $k_T$  algorithm, a sequential recombination jet finder, uses a slightly different approach. For every four-momentum vector  $i$  and  $j$  in the collection of input objects it defines the variables:

$$d_i = p_{T,i}^n, \quad (4.1a)$$

$$d_{ij} = \min(p_{T,i}^n, p_{T,j}^n) \frac{\Delta R_{ij}^2}{R^2}, \quad (4.1b)$$

with  $n = 2$ ,  $\Delta R_{ij}$  the distance between the two objects and  $R$  a distance parameter comparable to the cone size in the fixed cone jet finder. All values of  $d_i$  and  $d_{ij}$  are then put in a sorted list and the algorithm will start from the lowest value. If this lowest value is a pseudo-distance  $d_{ij}$  then input objects  $i$  and  $j$  will be merged. If the lowest value is a  $d_i$  the object  $i$  is considered to be a jet by itself and it is removed from the input. This process is repeated until no more input objects are available. At that point every input object will have become either a jet or a constituent of a jet. The distance parameters used in ATLAS are  $R = 0.4$  for narrow jets and  $R = 0.6$  for wide jets.

A relatively new development in jet finding algorithms is the anti- $k_T$  algorithm [68]. This algorithm is similar to the normal  $k_T$  algorithm, but the relative power between momentum and spatial distance is modified by setting the parameter  $n = -2$  in equation 4.1. As a result, the boundary of the jet is rigid with respect to neighboring soft jets, but flexible with respect to hard jets. This combines the good properties of the rigid cone and the flexible  $k_T$  algorithm. Due to its better performance, the anti- $k_T$  algorithm will become the new default algorithm in future ATLAS analyses.

Calibration of the jet energies is done by re-summing the calorimeter cells with weighting functions. These depend on the signal density (signal height divided by cell volume) and the position of the cell in the calorimeter. The weighting functions are fitted using simulated dijet QCD events. Validation of the jet calibration on real data will be done by studying known decay channels.

The performance of the jet reconstruction on Monte Carlo simulation is illustrated in figure 4.5. This figure shows the jet reconstruction efficiency as a function of the true jet  $p_T$ . The matching between truth jets and reconstructed jets is performed within a cone of  $\Delta R \leq 0.2$ .

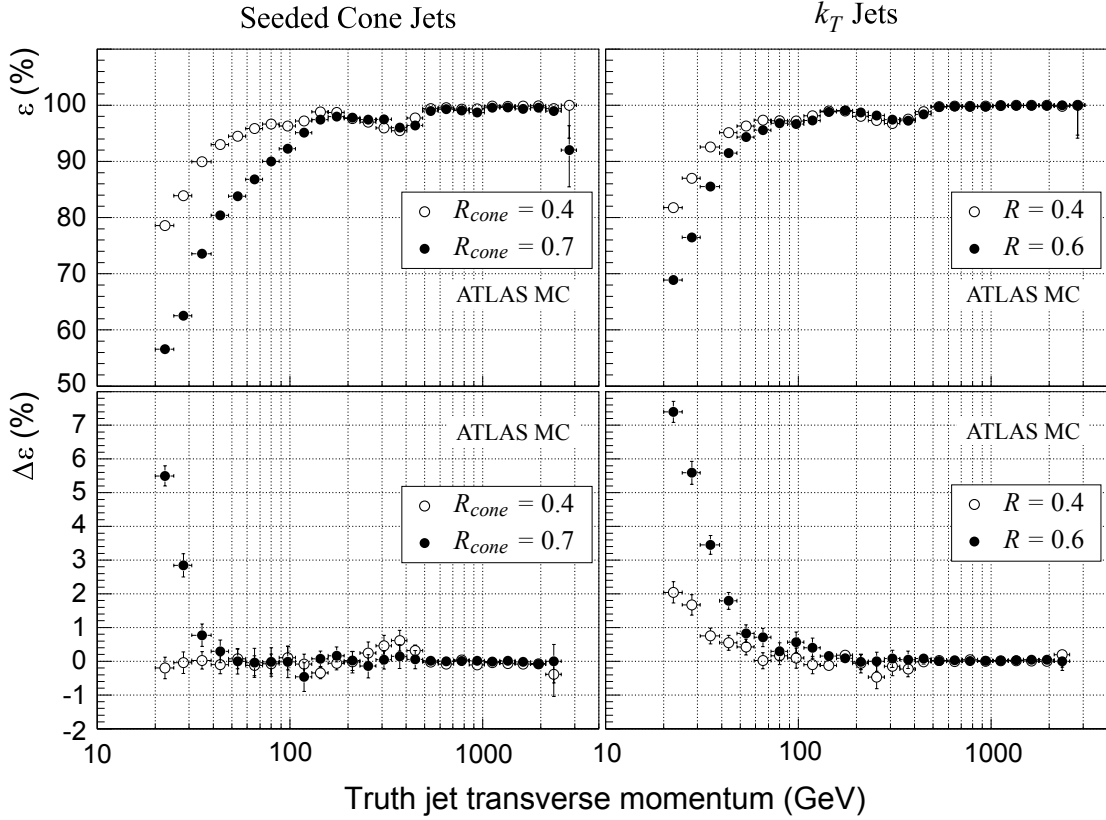


**Figure 4.5:** Monte Carlo jet reconstruction efficiency  $\varepsilon$  for cone jets (left) and  $k_T$  jets (right) in the rapidity region  $0.2 < |y| < 0.4$ . Cell clustering was done using the signal tower method. The bottom two plots show the difference in efficiency  $\Delta\varepsilon$  between the signal tower method and topological cell clustering for both algorithms. [67]

#### 4.3.4 B-tagging

Identifying jets containing  $b$  quarks is done by  $b$ -tagging algorithms. A distinctive feature of  $b$ -jets is that the  $b$  quark hadronizes into a  $B$  meson with a relatively long lifetime, typically of the order of 1.5 ps. When the  $b$  quark is produced with a considerable Lorentz boost, the decay products of the  $B$  meson can be identified as tracks that are not pointing to the primary vertex. In many cases, a secondary vertex can be reconstructed from these tracks. Most  $b$  quarks decay via a  $c$  quark, but the shorter lifetime of the  $c$  quark often does not allow a separate reconstruction of the tertiary vertex. The  $b$ -tagging algorithms in ATLAS are mostly based on identifying the tracks resulting from a  $B$  meson decay using impact parameter based variables.

The presence of a soft lepton from the semi-leptonic decay of the  $b$ -quark, or the subsequently produced  $c$  quark, is another property that can be used for  $b$ -tagging. But even though this tagging method provides a very high purity, it is intrinsically limited by the fraction of  $b$  quarks that decays semileptonically, which is only about 21%.

The default  $b$ -jet weight assigned to jets is a combination of the results from multiple tagging algorithms.

### 4.3.5 Tau leptons

Another type of jet that is identified separately are jets that originate from the hadronic decay of  $\tau$  leptons. Hadronic  $\tau$ -decays result in a very collimated jet with a low track multiplicity. Two complementary algorithms for  $\tau$  identification are used in ATLAS. The first is a track-based identification, optimized for processes such as  $W \rightarrow \tau\nu$  and  $Z \rightarrow \tau\tau$ . For higher transverse energy  $\tau$ -decays, a calorimeter based algorithm exists. This uses calorimeter clusters to identify  $\tau$  leptons from, for example, heavy Higgs boson decays. Roughly two-thirds of the  $\tau$  leptons will decay hadronically. The remainder decays leptonically and will be measured in the detector as an electron or muon.

### 4.3.6 Missing transverse energy

The only Standard Model particle that cannot be detected by the ATLAS detector is the neutrino. It can only be detected indirectly via the energy imbalance it leaves in the detector, which is referred to as the missing transverse energy ( $\cancel{E}_T$ ). New theories, such as supersymmetry, predict additional particles that will go undetected and often rely heavily on the missing transverse energy reconstruction for their discovery. This makes it a very important quantity to reconstruct.

The reconstruction of missing energy is challenging, since it requires a very precise knowledge of all the energy deposited in the calorimeter. Mismeasurements in any of these energies will translate in a mismeasurement of the missing energy. Some of the difficulties in reconstructing the missing transverse energy include:

**Noise** Because of the large number of readout channels in the calorimeters, the noise from these 200,000 channels alone contributes about 13 GeV to the width of the  $\cancel{E}_T$  distribution. Suppressing this noise is of crucial importance since the in-situ calibration of the missing energy scale will be performed using channels such as  $Z \rightarrow \tau\tau$  [69], where the amount of missing energy is relatively small. In order to suppress the noise, two methods can be used. The standard method is based on

only using calorimeter cells with an energy above a certain threshold. The threshold is optimized using Monte Carlo simulation. A symmetric threshold of  $2\sigma$  is generally used, so only cells with  $|E_{\text{cell}}| > 2\sigma_{\text{noise}}$  are taken into account. An alternative method is to base the  $\cancel{E}_T$  on topological cell clusters (see section 4.3.3). The seeded reconstruction of energy deposits in three dimensions inherently suppresses noise.

**Mismeasurement of jets** Even though the calorimeters were designed to provide as full as possible coverage around the interaction point, it is impossible to avoid gaps completely. Most importantly in the regions around  $|\eta| = 1.4$  and  $|\eta| = 3.2$ , the calorimeter has inefficiencies due to service outlets. Jet mismeasurement can also be caused by jet leakage. Jet leakage can occur when jets deposit part of their energy outside the active material of the calorimeter, for example in the cryostat between the electromagnetic and hadronic calorimeter. Such energy deposits can be partly recovered by correcting jets that have large energy deposits in layers adjacent to the cryostat or support structure.

**Fake  $\cancel{E}_T$  from muons** Fake missing transverse energy can also be caused by muons escaping detection or by the reconstruction of fake or badly measured muons. The muon spectrometer contains some inefficient regions, most notably at  $\eta = 0$  and around the transition from the barrel to the endcap detectors. In these regions, a muon could escape detection and contribute to the missing transverse energy. The opposite is also possible: a low  $p_T$  muon can be incorrectly combined with noise hits to form a high  $p_T$  muon, or a high  $p_T$  jet that is not fully contained in the calorimeter could be reconstructed as a muon. The latter is commonly referred to jet punch-through. Monte Carlo studies show that the muon fake  $\cancel{E}_T$  is dominated by missed muons rather than fake muons [69]. This means that recovery of muons in problematic regions of the muon spectrometer, for example using the tagging methods discussed in section 4.3.2, is of vital importance.

**Instrumental  $\cancel{E}_T$**  Another possible source of fake  $\cancel{E}_T$  are instrumental effects. This includes issues such as badly modeled distributions of dead material in the detector or instrumental failures in the calorimeters. While the precise nature and magnitude of these problems is unknown, Monte Carlo simulations have been performed by inserting random defects into the calorimeters. Based on these studies, instrumental effects can be suppressed by imposing cuts on, for example, the ratio of electromagnetic to hadronic energy in a jet.

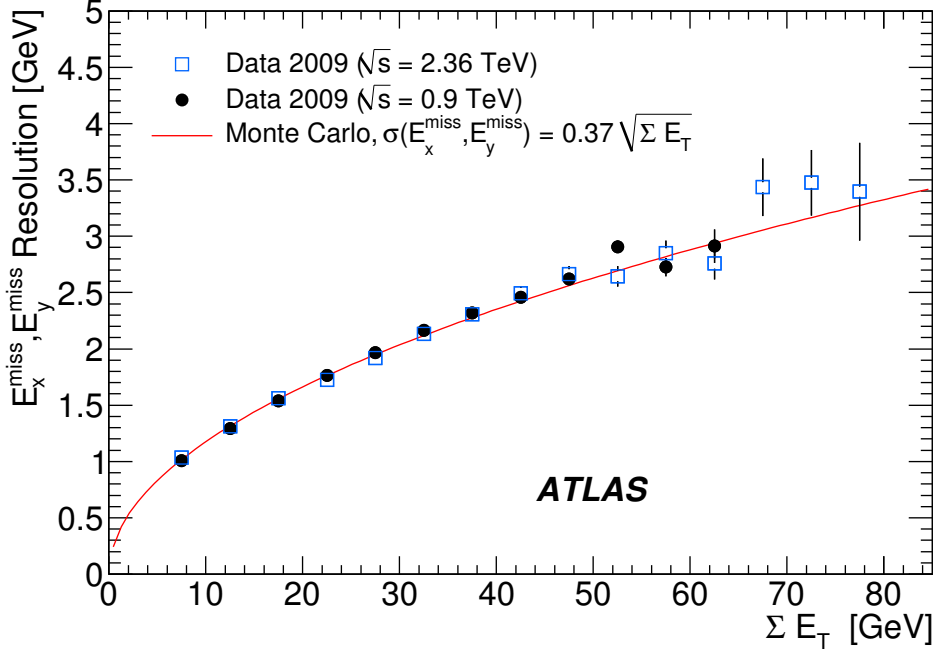


**Figure 4.6:**  $\cancel{E}_T$  resolution as a function of the total transverse energy,  $\sum E_T$ , for the 2009 dataset [70].

For the reconstruction of the missing transverse energy, three contributions are recognized. These are the calorimeter term, the cryostat term and the muon term:

$$\cancel{E}_{x,y}^{\text{final}} = \cancel{E}_{x,y}^{\text{calorimeter}} + \cancel{E}_{x,y}^{\text{cryostat}} + \cancel{E}_{x,y}^{\text{muon}}. \quad (4.2)$$

The reconstruction is based on summing the energies of the topological cell clusters,  $\cancel{E}_{x,y}^{\text{calorimeter}}$ . To correct the  $\cancel{E}_T$  for the energy lost due to jet leakage, the  $\cancel{E}_{x,y}^{\text{cryostat}}$  term is added. The cryostat term parameterizes the energy deposited in the cryostat between the electromagnetic and hadronic calorimeter based on the energy deposits in the adjacent calorimeter layers. The third term,  $\cancel{E}_{x,y}^{\text{muon}}$ , contains the muon contribution to the missing energy. Because the energy lost in the calorimeters is already included in the calorimeter term, the energy measurement provided by the muon spectrometer is used. To reject fake muons, however, muons that are within the acceptance of the inner detector ( $|\eta| < 2.5$ ) are required to have a matching inner detector track. Finally, a refinement step is performed for cells associated with a reconstructed high  $p_T$  object. For these cells the initial cell calibration is replaced by the energy calibration of the object, which is more accurately known. At this stage, the missing transverse energy is referred to as the refined final  $\cancel{E}_T$ .

The  $\cancel{E}_T$  resolution can be parameterized by [69]:

$$\sigma = a \sqrt{\sum E_T(\text{GeV})}, \quad (4.3)$$

with  $a$  a constant and  $\sum E_T$  the scalar sum of the total transverse energy.

Using minimum bias events, soft proton-proton interactions where no true missing energy is expected, an estimate of the  $\cancel{E}_T$  resolution can be obtained from early data [70]. Figure 4.6 shows the first resolution measurement, using the 2009 datasets. The data points show the results obtained for the two center of mass energies that were used:  $\sqrt{s} = 900 \text{ GeV}$  and  $\sqrt{s} = 2.36 \text{ TeV}$ . The fit was obtained by fitting equation 4.3 to the  $\cancel{E}_T$  resolution in Monte Carlo simulation.

## 4.4 Analysis frameworks

The Athena framework provides an environment for the full reconstruction of an event, which often causes Athena jobs to be rather large and complex. For this reason, several solutions have been developed within the Athena framework to provide an additional layer of abstraction. For the analysis presented in this thesis, the AMA framework [71] has been used.

The structure of the AMA framework is comparable to Athena itself. It uses a modular design with job steering through configuration files. However, with AMA the focus lies on the fast and easy creation of a highly configurable analysis and re-usability of developed analysis tools.

AMA can read a variety of input files. The objects in these files are then converted to labeled four-momentum vectors and made available to the user. Most of the particle and event selection tasks can be done from the configuration file using standard selection modules. For more complex selection tasks and the analysis itself, additional modules can be written. The final stage of the analysis is performed using the ROOT [72] framework in conjunction with the RooFit [73] data modeling toolkit.

# Chapter 5

## Atlantis event display

Modern particle detectors produce enormous amounts of data. Interpreting these data and deriving the physical quantities of interest is done by complex reconstruction and analysis algorithms running autonomously. To be able to trust the outcome, however, a physicist needs to be able to check every step in this process and verify the decisions and calculations made by the software.

This presents the challenge of efficiently transferring the massive amount of data in an event to the human brain. One of the best methods to achieve this transfer is to use a visual representation of the data. However, given the complexity of the detector, this is still far from a trivial task. Great care has to be taken that the data are not only displayed correctly, but also that they are interpreted correctly by the user. In this chapter the Atlantis event display and its approach to these issues will be discussed.

The author of this thesis has contributed to many different aspects of the Atlantis event display. Among others, this includes the visualization of tracks and track segments; the retrieval and visualization of the detector geometry; the visualization of individual cells and modules for hardware debugging purposes; the visualization of pixel and SCT hits; the visualization of several new reconstructed objects as part of the migration to the new event data model definition in Athena; and many efficiency improvements, for example the reduction of the event file size by implementing a mechanism for readout identifier decoding in Atlantis.

Because a full description of all these individual projects would lack a certain amount of coherence, and since there is currently no reference available providing a general overview of the Atlantis event display, it was instead chosen to write this chapter as a comprehensive discussion of the Atlantis software as a whole.

## 5.1 Event display requirements

Event displays are used at various stages in the processing of the detector data. Every such application poses its own set of requirements.

One of the first usages of visualization in a collider experiment is the detector monitoring. In the control room, a small sample of events is reviewed to determine if the detector is functioning correctly. The interesting data to visualize at this stage are the raw hits from the detector. It is especially important to have a clear view of the detector modules from which the data are coming. At this stage an event display can be crucial, for example, to detect problems in the electronics that prevent detector modules from being read out. Unless problems have been found, it is usually not necessary to have much interaction with the users of the event display. In general, a set of predefined views is used for detector monitoring. The views are chosen such that, together, they cover the important parts of the detector.

Next in the event processing chain is the reconstruction. The data from the detector are calibrated and the higher level objects, such as tracks and jets, are built. At this stage, visualization is used to check that the reconstruction software is functioning properly. Is every hit found and correctly associated to the track? Are outliers rejected as they should? Are trajectories that cross between two detector modules found correctly or could there be a problem with the alignment? Is the missing transverse energy correct or could it be caused by a mismeasurement of one of the jets? Being able to answer these questions using visual investigation requires a very detailed display of individual reconstructed objects and a clear visualization of how they are related to lower level objects and raw detector data.

Then there is the analysis stage. Here it becomes important to have an overview of the full event. Visualization can be used to investigate characteristics of certain event topologies in order to devise selection criteria. The event display can also be used to investigate events that exhibit strange features. These features often point back to problems in the reconstruction software or even the hardware, so it is essential to have access to the lower level objects and the raw hits as well.

Finally, event visualization is heavily used for presentations, publications and outreach. Presenting events to a non-expert audience calls for highly intuitive pictures, while at the same time the size and resolution of plots is often limited. Despite this, the speaker should still be able to convey the essence of an event to the audience without much additional explanation.

The Atlantis [74, 75] event display is a tool which aims to cater to the above require-

ments in a single program. Its fundamental goal is threefold:

- It should visualize complete ATLAS events. For a thorough investigation of an event it is necessary to display the raw hits as well as the higher level reconstructed objects from all subdetectors.
- The events should be comprehensible. The user should be provided with the tools that are necessary to understand the physics that occurs in an event.
- It should be fast. Investigating events is a very interactive job, so input from the user should be processed in nearly real time on an average desktop computer. This means that no complex reconstruction or calculation tasks can be done during the display of events.

## 5.2 Visualization methods

The most straightforward approach when trying to visualize data is often to make a picture that is as realistic as possible. However, for complex structures such as the hits and tracks in a particle detector, a three dimensional perspective view does not result in a clear picture. In such a picture, data are superimposed and the view of the inner regions of the detector is obstructed by the outer layers. Even in a cut-away perspective view, where parts of the detector are hidden to provide a view on the inner layers, it is virtually impossible to have a clear view of the event as a whole.

A first step towards solving this problem is to move from a three dimensional view to a two dimensional cross section picture. However, the amount of data that is visible in a cross section is limited. Many slices would be needed to obtain the full picture. An effective compromise is the combination of cross sections and projections onto the cross section plane. In this way, a few slices suffice to display the full detector.

This choice implies that the detector geometry cannot be visualized in detail, but this is not a problem for the goals set out earlier. When focusing on the measured data, the detector geometry acts merely as a context for the displayed measurements. This means it can be further simplified to the ideal detector geometry or, in the case of physics analysis, just the general outline of the subdetectors.

## 5.3 Data oriented projections

The projections used to visualize the detector data in two dimensional plots are what Atlantis refers to as *data oriented projections*. This emphasizes the fact that the pro-

jections are based on the coordinate measurements made in the different subdetectors of ATLAS. Many of the readout elements measure only two coordinates. In this case, projecting the measurements on a plane perpendicular to the remaining coordinate leads to a two dimensional plot in a natural way, without losing information. The coordinates that are measured by the detector, however, are in general not the Cartesian coordinates. As a result, this method can lead to plots that are less intuitive and require some training on the side of the user.

This section will discuss the data oriented projections that are available in Atlantis and how these projections help a physicist to investigate different aspects of an event.

### 5.3.1 $Y/X$ and $\phi/\rho$

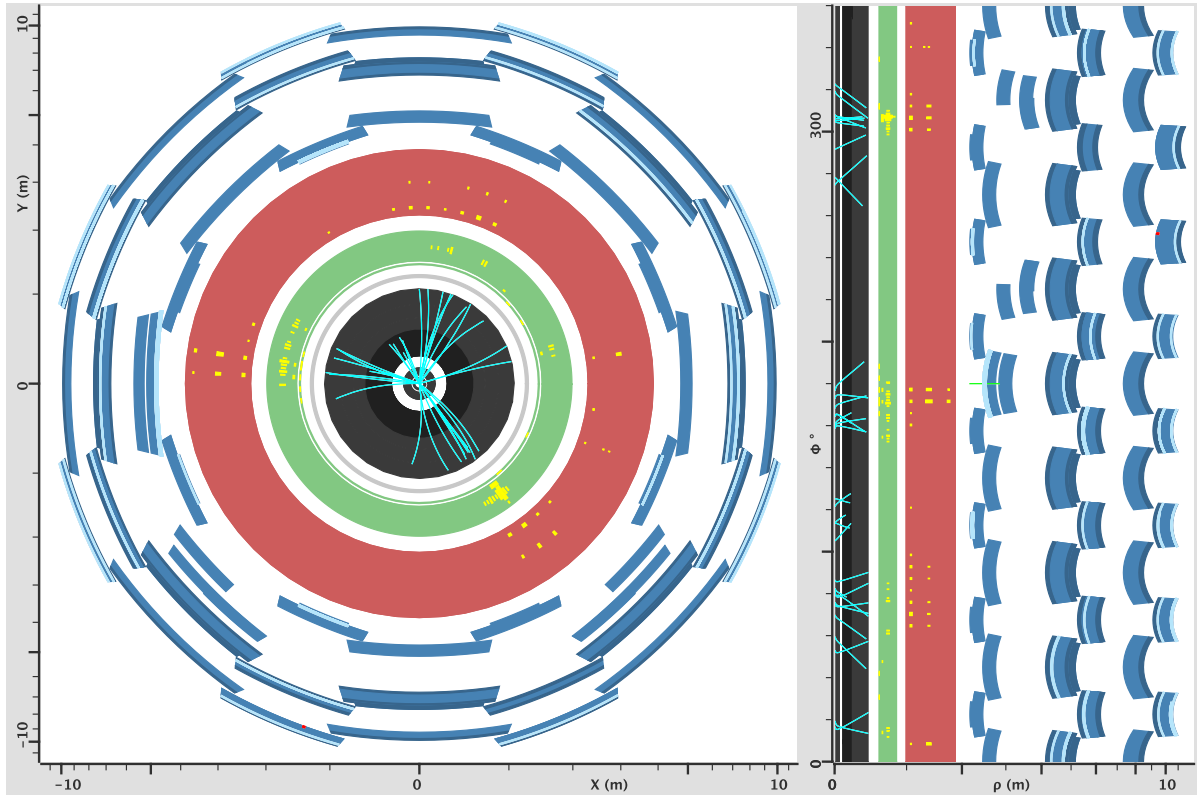


**Figure 5.1:**  $Y/X$  (left) and  $\phi/\rho$  (right) projections of a four-jet event. The  $Y/X$  projection uses the fisheye transformation to enhance the separation of tracks, while the  $\phi/\rho$  achieves this intrinsically. This event was taken from the second 7 TeV collision run.

The  $Y/X$  projection, shown in figure 5.1, is one of the most intuitive projections in Atlantis. In this projection the data from the endcaps are hidden and all the measure-

ments from the barrel are projected onto a plane perpendicular to the beam axis. In this way, the layered structure of the barrel subdetectors can be shown very well and particle trajectories can be followed from the point where they originate all the way through the muon system.

In the inner regions, the detector uses a very fine granularity. Further away from the beam axis, this granularity becomes more coarse. In the Y/X view, however, the inner detector occupies only a relatively small area of the picture. To better visualize the high hit density in the inner detector, the so-called *fisheye* transformation can be applied. This is a radial zoom that enlarges the center of the detector, while at the same time it shrinks the outer regions. The fisheye zoom transforms the radial coordinate as:

$$\rho \rightarrow \frac{1 + c_f \rho_{\max}}{1 + c_f \rho} \rho, \quad (5.1)$$

where  $c_f > 0$  is a constant that controls the degree of fisheye deformation and  $\rho_{\max}$  is set to the outer edge of the detector. The value of  $c_f$  is controlled by the user. The fisheye transformation greatly enhances the visibility of the inner detector hits, while also the calorimeter and the muon spectrometer remain fully visible.

The Y/X projection can also be used to display the endcap detectors. This can only be done in slices, because the endcap contains several layers that each have a different geometry. Nevertheless, these slices provide a good view of the endcap calorimeters and the wheels of the muon spectrometer.

Instead of using the fisheye transformation in the Y/X projection, the visibility of the inner detector hits can also be enhanced by using a slightly different projection. The same information as in the Y/X projection can be drawn using the polar coordinates  $\phi$  and  $\rho$ , as shown in figure 5.1. The circular cross section of the detector is then opened up and the concentric layers become rectangular in the  $\phi/\rho$  projection. This improves the angular separation in the inner detector, making it easier to distinguish the measurements. This is not an intuitive projection though. At small radii, points that are arbitrarily close together can still be drawn a large distance apart.

### 5.3.2 $\rho/Z$ and $X'/Z$

An intuitive projection complementary to the Y/X view is the projection parallel to the beam axis. However, this is not as straightforward as the Y/X projection. If the data are simply projected onto a plane, the measurements from different subdetectors will be superimposed. This can be solved by plotting  $\rho$  versus  $z$ , as shown in figure 5.2. To optimally display jets that are back-to-back, some minor improvements to this projection

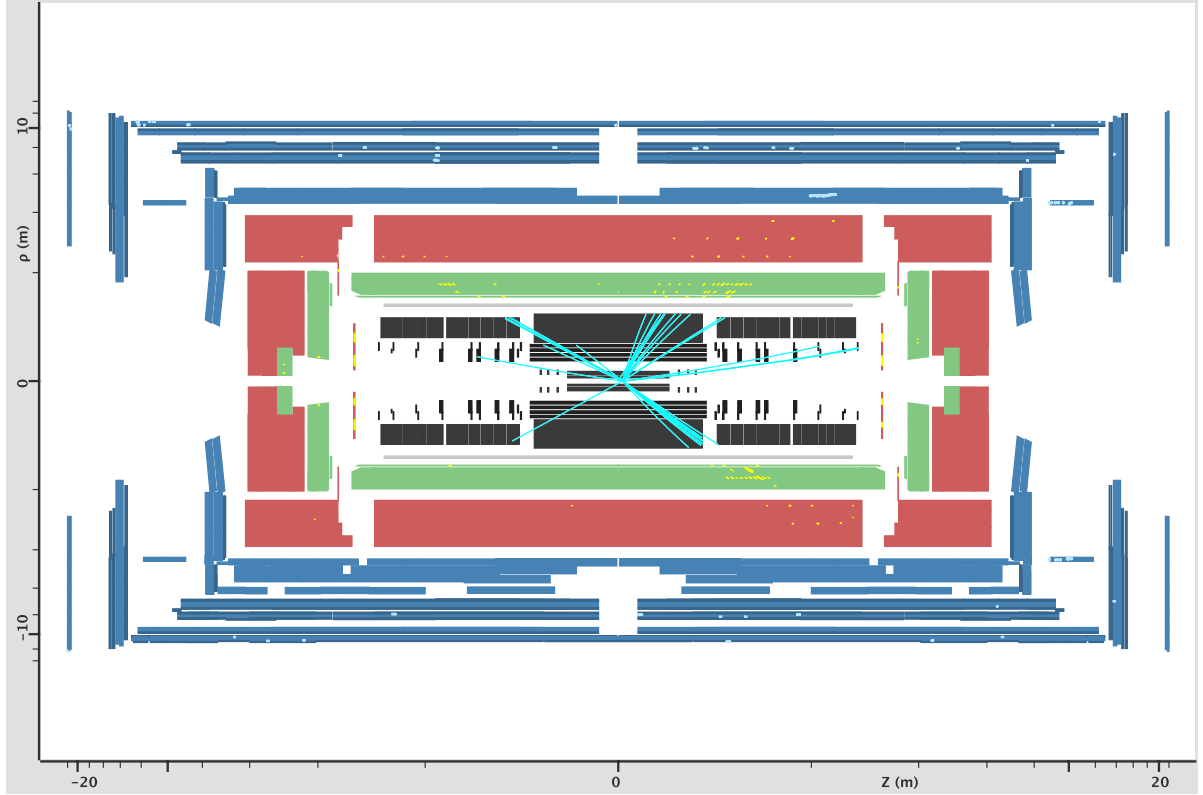


**Figure 5.2:**  $\rho/Z$  projection of the four-jet event from figure 5.1. Again, a fisheye transformation is applied to enhance the visibility of the inner detector.

can still be made. One improvement is to define a plane parallel to the beam axis, that divides the detector in two parts. Data from above this plane are drawn with a positive  $\rho$ -coordinate and data from below are drawn with a negative  $\rho$ -coordinate. The resulting  $\rho/Z$  projection has an optimal separation of reconstructed objects. If necessary, it can be adjusted by changing the  $\phi$ -angle of the dividing plane. The  $\rho/Z$  projection is the only projection that can show the full detector geometry in a single plot.

Just as for  $Y/X$ , the inner region can be enlarged at the expense of the outer regions by applying a fisheye zoom. A radial zoom in this plot would deform the detector, so a rectangular version is used that transforms the  $\rho$ - and  $z$ -coordinates separately.

The effectiveness of projecting the detector measurements in the  $\rho-z$  plane is a result of the cylindrical geometry of the detector. Approximating the detector with a perfect cylinder works well in most cases, as the detector has a very fine segmentation in  $\phi$ . In the muon spectrometer, however, there are only 16 azimuthal sectors. Because the MDT chambers do not measure the  $\phi$  coordinate, a fully accurate measurement of  $\rho$  is not available. The displayed  $\rho$ -coordinate is only valid for the middle of the tube.

This means that for tubes that were hit near the end there will be a slight discrepancy between the real and the displayed  $\rho$ -coordinate. This makes the  $\rho/Z$  plot unsuitable for visualizing the association between muon tracks and hits.

For studying muon track reconstruction the  $X'/Z$  projection is provided. In this projection the tracks and hits in a single muon  $\phi$ -sector are projected onto a plane in the center of the sector. In this way, the tracks are projected to match the projection of the hits and a proper comparison can be made.

### 5.3.3 $\phi/Z$

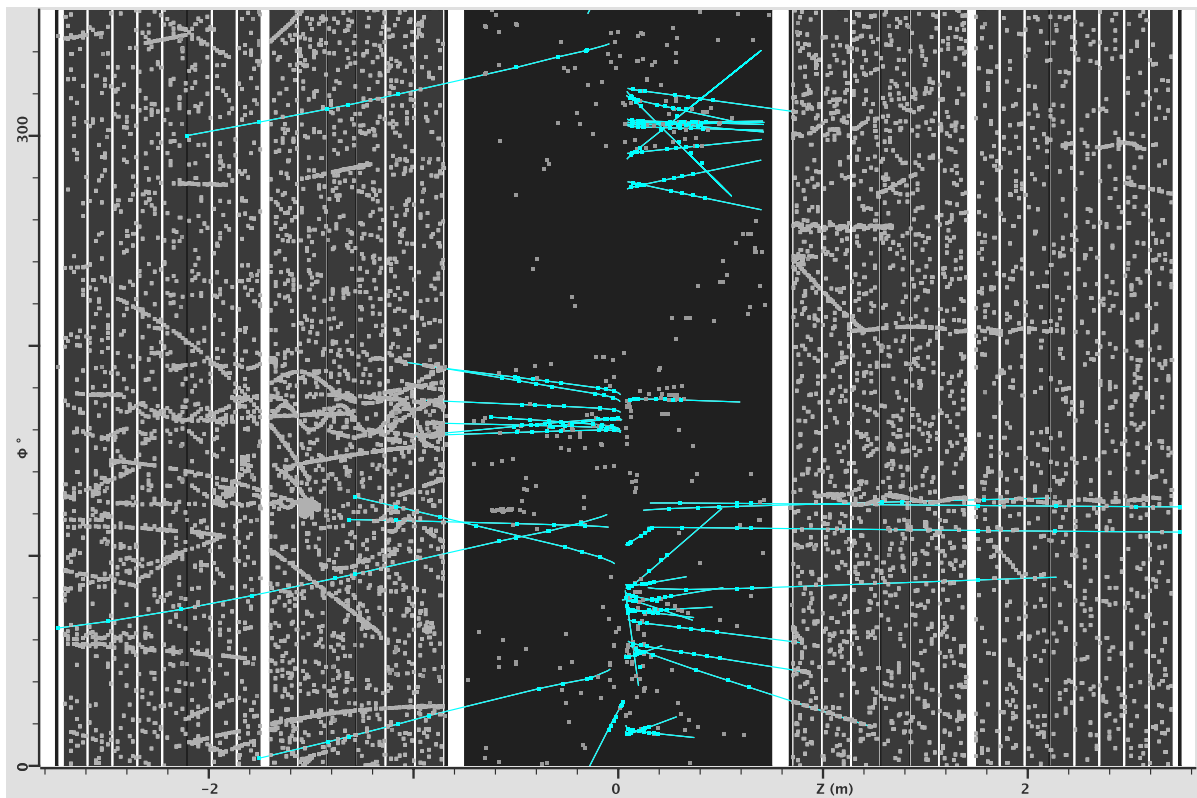


**Figure 5.3:** View of the pixel, SCT and two TRT endcap detectors in the  $\phi/Z$  projection. The TRT barrel is hidden, since this subdetector does not measure the  $z$ -coordinate. In this projection the tracks become more horizontal with increasing momentum. Furthermore, the direction of the track indicates the charge: for negatively charged particles  $\phi$  increases with  $|z|$ , while for positively charged particles  $\phi$  decreases. Many hits belonging to low momentum tracks can be seen in the TRT endcaps.

The intuitive  $Y/X$  and  $\rho/Z$  projections still leave some areas which are not fully

covered. In particular the visualization of the endcap detectors with a radial geometry. These can be visualized in the  $Y/X$  projection, but this projection does not show the whole endcap in a single picture. Also, it is difficult to visualize particle trajectories in the forward direction using the  $Y/X$  projection.

To provide a good visualization of the endcap detectors and the tracks going into the endcaps, the  $\phi/Z$  projection was introduced. This projection is shown in figure 5.3. It can be understood as the detector being projected onto a cylindrical surface around to the beam axis. This surface is then unfolded, resulting in the  $\phi/Z$  projection.

### 5.3.4 V-Plot

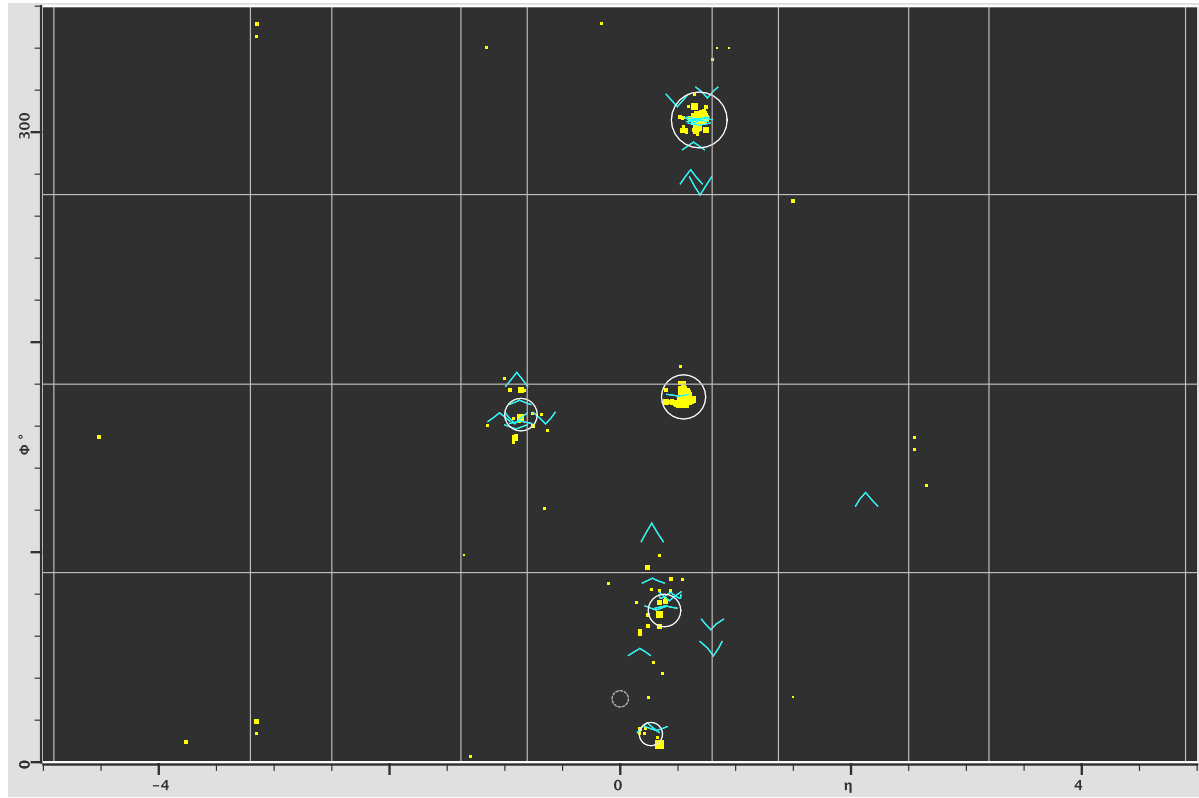


**Figure 5.4:** V-Plot showing the full coverage of the detector. The ‘V’-shaped tracks are drawn superimposed on the calorimeter cell energy deposits. The circles indicate the positions of the reconstructed jets, their radius representing the total energy of the jet. The dashed circle is the reconstructed missing energy.

The previous sections discussed the projections to visualize specific subdetectors. Together, these projections cover the full ATLAS detector and they allow a user with

little or no experience to visually investigate events. For the expert physicist, however, there is the need to incorporate more information into a picture. In this case, it is not a problem to require some training on the side of the user. Therefore some level of intuitiveness can be traded for a higher information content.

An interesting plot with a very high information density is the  $\phi/\eta$  projection. This projection is often referred to as the *V-Plot*, for reasons that will become clear later. Most of the techniques used in this plot were first introduced in the DALI [76] event display for the ALEPH experiment at CERN. An example of the V-Plot is shown in figure 5.4.

In the reconstruction and analysis software,  $\eta$  is defined with respect to the primary vertex position. The plane perpendicular to the beam axis and containing the vertex is described by  $\eta = 0$ . Therefore, a neutral particle coming from the primary vertex will have a trajectory with constant  $\phi$  and  $\eta$ . Such a particle would be represented in this projection by a single point. A charged particle will be bent in the plane perpendicular to the beam axis, so its  $\phi$  coordinate will change while  $\eta$  remains constant. Such a track will be projected as a short vertical line. The amount of bending in the solenoidal field is inversely proportional to the transverse momentum of the particle, so low momentum tracks will be longer than high momentum tracks.

A disadvantage of projecting tracks in this way is that it is impossible to see the direction of the track. However, depth information can be added quite easily by transforming the  $\eta$ -coordinate according to:

$$\eta \rightarrow \eta \pm k(\rho_{\max} - \rho). \quad (5.2)$$

Here  $\rho$  is the radial position of a point on the track,  $\rho_{\max}$  the outer radius of the inner detector and  $k$  an arbitrary constant. For an inner detector track ( $\rho < \rho_{\max}$ ) every point on the track is transformed into two new points, spaced apart by a small distance in  $\eta$ . This small distance is a measure for the distance of the point to the beam axis, thus incorporating depth information into the displayed track. The tracks will now be drawn in a ‘V’-shape, giving the plot its name. The end of the arms of the ‘V’ represents the point where the track originated, the real position being in the middle of the two points. The tip of the ‘V’ is the point where the track exits the inner detector and enters the calorimeter. The direction of the ‘V’ is determined by the bending direction, thus showing the charge of the particle. For positively charged particles the tip of the ‘V’ is pointing down, for negatively charged particles the tip is pointing up. Furthermore, the angle between the arms of the ‘V’ is a measure for the transverse momentum of the track. For low momentum tracks the angle will be small, while for high momentum

tracks it can be almost 180 degrees.

An interesting class of tracks to study in this projection are tracks that do not originate from the primary vertex. Far from the vertex, such a track is still pointing approximately towards the primary vertex, therefore in the  $\phi/\eta$  projection it will behave similarly to any other track. Close to the vertex, however, the  $\eta$ -coordinate will change rapidly as the track passes the primary vertex with a nonzero impact parameter. This creates a very distinct curve on one side of the track, making the V-Plot a very good tool to identify particles originating from a secondary decay.

Any three dimensional object in the inner detector can be transformed as described above, using equation 5.2. This allows the drawing of silicon tracker hits in the same plot, making it possible to use the  $\phi/\eta$  projection to check the hits that were used for the reconstruction of a track. Furthermore, hits belonging to a track that was not reconstructed will show up in a clear ‘V’-shape.

Another correlation that can be visualized very well in the  $\phi/\eta$  projection is the correlation between the inner detector tracks and the energy deposits in the calorimeter. Most of the calorimeter is built using a  $\phi\text{-}\eta$  geometry, making the cells in a layer appear as simple non-overlapping squares in this plot. In the normal view, the cells are drawn as a standard two dimensional box histogram. A particle trajectory which crosses a particular group of cells in the calorimeter will appear as a ‘V’-shaped track with its tip pointing into the energy deposit.

To study a particular jet in more detail, it is possible to zoom in on a certain area of the plot and to display the layers of the calorimeters separately in a series of plots. In the standard plot the inner detector tracks point towards the entry point into the calorimeter, but when the layers are displayed separately the tracks are extrapolated to the entry point into the selected layer. This way, the plots show the approximate progression of a track through the calorimeter. The use of multiple plots, however, introduces the difficulty of correlating the plots with each other. In most situations, it will be difficult to instantly locate a certain position in all of the plots. This can be solved by adding a visual aid in the form of the so-called *islands*. These islands are basically the outlines of the calorimeter clusters and are drawn in the background. The irregular background shape then provides enough reference for the user to quickly locate a position in the plots.

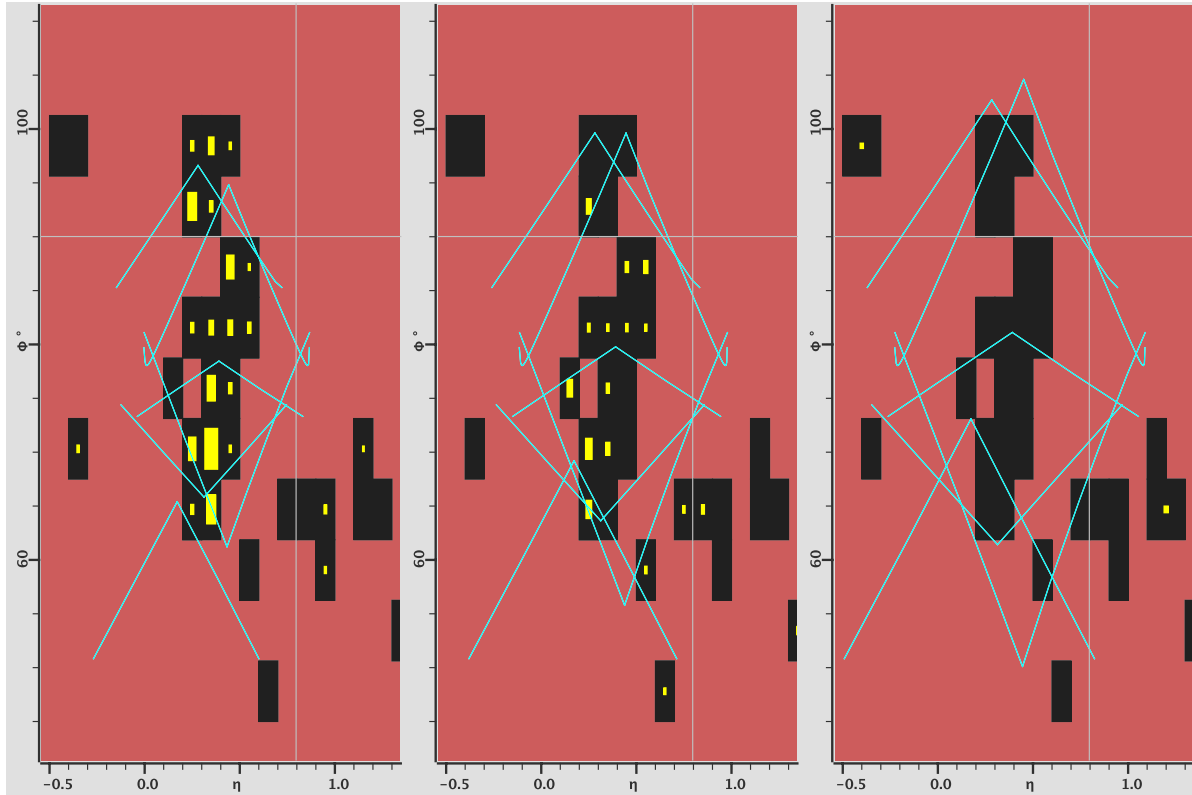


**Figure 5.5:** V-Plot showing tracks traversing three consecutive layers of the hadronic calorimeter. The tracks are extrapolated such that the tip of the ‘V’ shows the entry point into each layer. The colored fraction of a calorimeter cell indicates the amount of energy deposited relative to the cell with the highest energy deposit.

## 5.4 Interactive analysis

In addition to displaying event data, the Atlantis event display also provides some tools to perform simple analysis tasks on the presented data. These tools focus on helping the user understand the physics of the displayed event.

### 5.4.1 Invariant mass calculation

Whenever possible, four-momentum vectors of the reconstructed objects will be available in Atlantis. The user can group objects together and request Atlantis to calculate the invariant mass of the combination. A very instructive example of how such a simple operation can be of great help in the visual investigation of an event is a Higgs boson decaying into leptons. In a suspected  $H \rightarrow ZZ^{(*)} \rightarrow 4\ell$  event it enables the user to check whether the invariant mass of a lepton pair is indeed consistent with the mass

of the  $Z$  boson. Deviations could be caused by badly reconstructed leptons, wrong pairing or maybe a background event that passed the Higgs selection criteria. It would be extremely hard to obtain this information from a standard visualization.

### 5.4.2 Vertex fitting

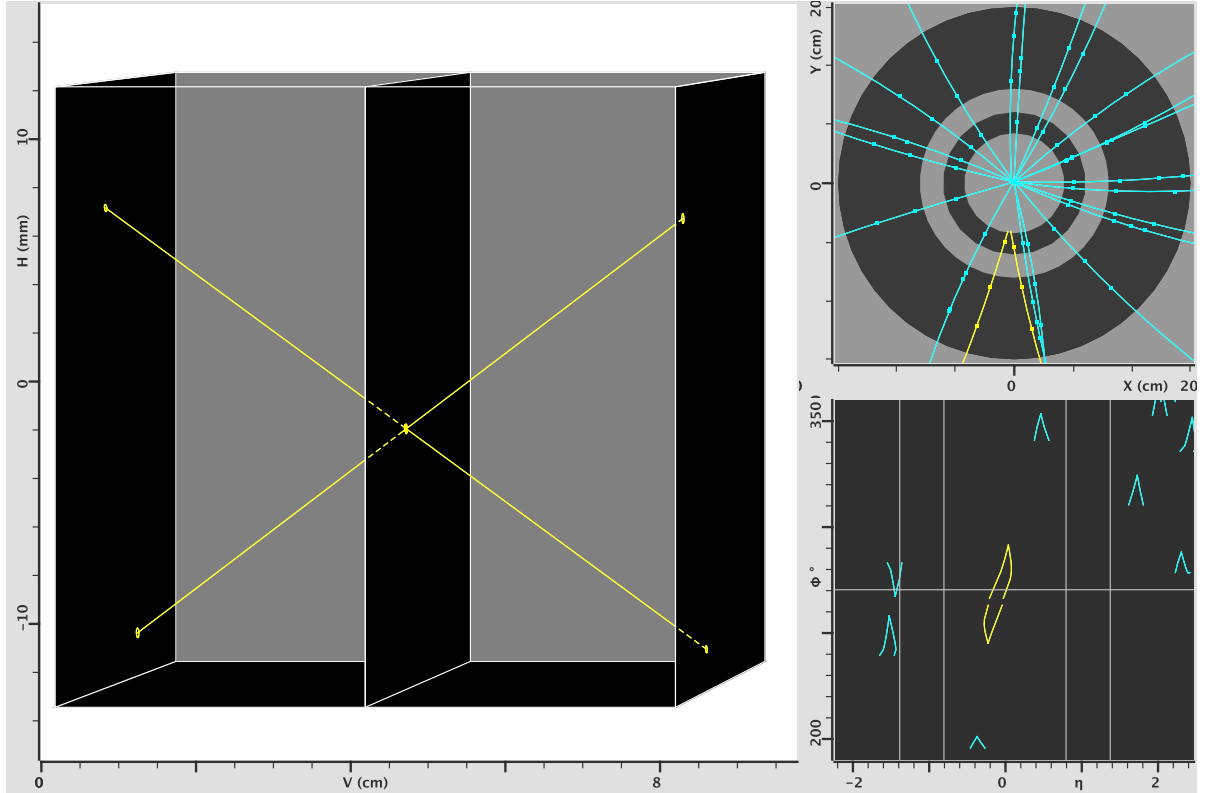


**Figure 5.6:** A secondary vertex fitted to a  $K_S^0 \rightarrow \pi^+\pi^-$  candidate in the 900 GeV collisions from December 2009. The 3D Box projection (left) shows a plane containing the primary vertex on the left and a plane containing the newly created secondary vertex in the middle. These planes are perpendicular to the direction of a neutral particle going through both vertices. The tracks are drawn with ellipses representing the measurement error in each of the planes. The V-Plot (bottom right) shows the deformation of the ‘V’-shape for these tracks. In the Y/X projection (top right) the vertex is shown in the transverse plane.

As discussed, the features of the V-Plot facilitate discovery of tracks that do not originate from the primary vertex. To investigate whether a group of such tracks originates from a common secondary vertex, a tool is provided to fit a vertex to a group of tracks. This tool is based on a Java implementation of the YT<sub>OP</sub> algorithm [77],

which was used in the ALEPH experiment. The group of tracks and the newly created vertex can then be investigated further in the so-called *3D Box* projection. This is a special three dimensional view in which only the tracks and the newly created vertex are displayed. Three vertical planes are shown, spaced apart by an equal distance. This distance is chosen such that the primary vertex is located in the leftmost plane and the newly created secondary vertex in the middle plane. The user can then rotate the tracks around an axis perpendicular to the planes to check the vertex fit. For an accurate perception of depth, the tracks do not extend beyond the image boundaries and end on the left and right planes. An example of a vertex display in the 3D Box projection is shown in figure 5.6.

### 5.4.3 Hit filtering

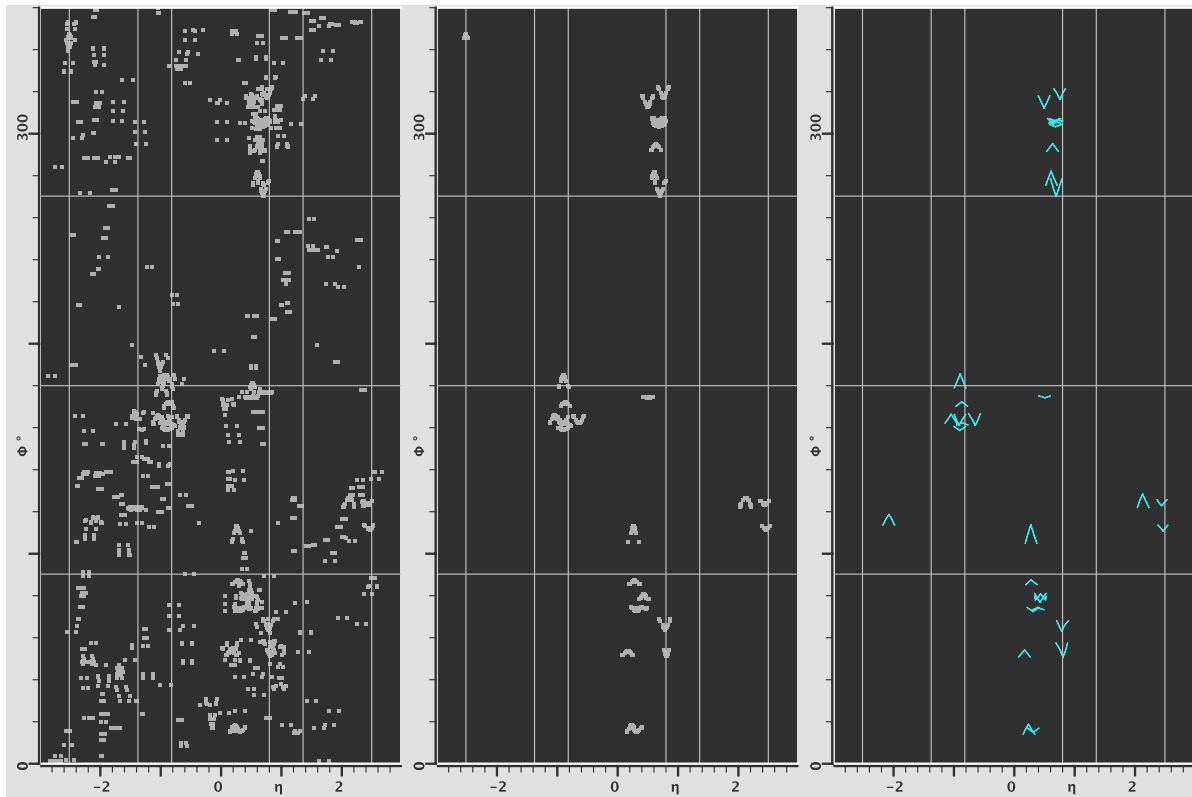


**Figure 5.7:** V-Plot demonstrating the internal hit filter. Silicon space points before filtering (left), after filtering (middle) and the reconstructed tracks (right). The bin size used for filtering was  $\Delta\eta \times \Delta\phi = 0.004 \times 0.2^\circ$ . A minimum of four hits was required for a bin to be accepted by the filter.

During high luminosity running of the LHC, the inner detector will experience high hit occupancies. For the event display user, this makes it much more difficult to see if tracks might have been missed by the reconstruction or even to compare tracks and hits in general.

Atlantis contains an internal hit filter capable of removing hits that are not consistent with a track originating from the primary vertex. This filter is based on an algorithm [78] used in the level 2 trigger. This algorithm makes use of the fact that a straight track pointing toward the primary vertex has constant  $\eta$ - and  $\phi$ -coordinates. When binning the inner detector hits in a 2-dimensional  $\eta$ - $\phi$  histogram, all hits belonging to a certain track will, due to bending, end up in a few neighboring bins. By requiring bins to exceed a certain number of hits before their contents are accepted, a large fraction of the noise hits can be rejected. The result of the filter is illustrated by figure 5.7, where a comparison is made between the filtered hits, the unfiltered hits and the reconstructed tracks.

## 5.5 Technical implementation

Visual investigation of events is a task that, ideally, should also be possible in an environment with limited or no network access. A physicist might occasionally want to work from a hotel room or update a presentation while traveling to a conference. However, running the full Athena framework on a normal desktop or laptop machine is impractical and running a graphical application on a remote machine puts high demands on the network connection. Therefore the choice was made to design the Atlantis event display as a standalone application.

### 5.5.1 Program structure

Atlantis is implemented in the Java programming language. Java is a relatively new object oriented programming language. One of the important advantages is that, after compiling, the same Java bytecode can run on many different operating systems. This makes it an excellent choice for the heterogeneous environment of the physicists' laptop and desktop computers.

In the Java language, classes are grouped in packages. This section will provide an overview of the structure of the program by discussing some of the packages within Atlantis. Atlantis consists of about 15 packages, with the core packages being:

`atlantis.parameters` The parameter tree plays a central role in Atlantis. This tree is

read from file when the program starts and can then be adjusted by the user. All the parameters for drawing geometry and event data, such as colors and cuts, are stored in this tree. Parameters are available to all classes in the program.

**atlantis.event** This package handles the event data. The event data are read from an event source and the corresponding Java classes are constructed. Data from the different subdetectors as well as the higher level reconstructed objects all have separate classes. Inheritance is used to minimize code duplication. An event data class returns an array of drawable objects for a specified projection.

**atlantis.geometry** The geometry package handles the drawing of the detector geometry. The three dimensional geometry information is read from file at the start of the program. This package constructs the Java classes for the different detectors. These classes return the drawable objects which represent the detector geometry for a given projection.

**atlantis.canvas** The canvas is the main window of the event display. It consists of a series of layered panels with predefined positions and sizes. The event and geometry data is drawn into these panels.

**atlantis.gui** The graphical user interface (GUI) package handles most of the interaction with the user. It displays the parameter tree in a graphical interface, allowing the user to manipulate the parameters. It also allows the user to select tools (zoom, pick, rubberband, etc.) to directly manipulate objects in the canvas.

**atlantis.interactions** Interactions are the manipulations available to the user to perform on the projected event or geometry data. Examples include zooming, rotating or more complex operations such as the fisheye transformation. The methods provided in this package act on the coordinates of the drawable objects before they are drawn.

**atlantis.list** Lists in Atlantis provide a way to combine data objects and perform operations on the combination. This includes operations such as summing calorimeter cell energies or invariant mass calculations on tracks.

**atlantis.graphics** The graphics package provides the methods that paint the drawable objects. It can produce pixel based output for creating normal image files or for displaying on a screen, but it can also create vector based output for high quality printing.

### 5.5.2 Event data access

Since Atlantis is a standalone application, all data necessary for displaying an event need to be converted from the C++ objects in Athena into a format Atlantis can handle. The JiveXML package in Athena provides this link between Athena and Atlantis.

JiveXML consists of a series of so-called data retrievers. A data retriever is a C++ class that retrieves one specific type of data for Atlantis. It reads the necessary objects from the transient data store and returns a subset of their parameters in a standardized format. The output from all data retrievers is then combined and formatted as XML. The output can either be written to file or sent to Atlantis over a network connection [79].

XML, an acronym for extensible markup language, is a widely used text based data format [80]. Tools to view, edit or extend XML data are available abundantly, making it a very easy format to work with. The basis of an XML document is formed by the so-called elements, which can contain other elements or textual data. This markup allows for a simple definition of a tree structure.

Every type of detector data is represented by an element in this tree. These elements contain parameter elements, one for every parameter that needs to be transferred to the event display program. Within these parameter elements is a space delimited array of values containing the actual data.

Duplicate data type elements within this tree are also allowed, the user can then choose which collection they want to display from inside Atlantis. This is mainly used for reconstructed objects such as tracks, where the output of multiple reconstruction algorithms can be stored in the event data and compared in the event display.

In this format, a set of four silicon space points would produce a data type element which looks like the following XML fragment:

```
<S3D count="4">
  <barcode>
    684 684 684 684
  </barcode>
  <clusters multiple="2">
    218936351 218935322 218936351 218935338
    218936365 218935322 218936365 218935338
  </clusters>
  <etaModule>
    0 0 0 0
  </etaModule>
```

---

```

<phiModule>
  25 25 25 25
</phiModule>
<x>
  -50.310535 -47.204992 -53.408140 -49.922278
</x>
<y>
  8.100264 7.600255 8.475154 7.921994
</y>
<z>
  273.293250 273.293250 273.293250 273.293250
</z>
</S3D>

```

These space points were taken from a simulated event, hence they have a `barcode` field that contains the identifier of the simulated particle that produced them. The simulated particle trajectories are stored elsewhere in the event file. In a similar way, the `clusters` field associates the space points to the raw silicon strip hits they were reconstructed from. The `etaModule` and `phiModule` fields identify the location of the inner detector module that contained the hits. The `x`, `y` and `z` fields, finally, provide the full spatial coordinates of the hit.

## 5.6 Visualization of the first collisions at 7 TeV

During the startup phase of the LHC, Atlantis has been used intensively to create event displays for the media and for other outreach purposes. The first months of operation have been essentially a journey through the history of particle physics. As more data became available, the particles of the Standard Model were rediscovered. This section will show some of the highlights of these rediscoveries, using displays of the first ATLAS events to demonstrate the features of the event display.

On the 5<sup>th</sup> of April 2010, six days after the 7 TeV-startup of LHC, one of the first  $W \rightarrow e\nu$  candidates was observed in the ATLAS detector. This event, shown in figure 5.8, contains an  $e^+$  with a transverse momentum of 34 GeV (yellow) and a missing transverse energy of 26 GeV (gray dashed line). The  $Y/X$  view on the left shows the electron passing through the inner detector. Also the corresponding energy deposit in the electromagnetic calorimeter is visible. The hits associated to the electron track are

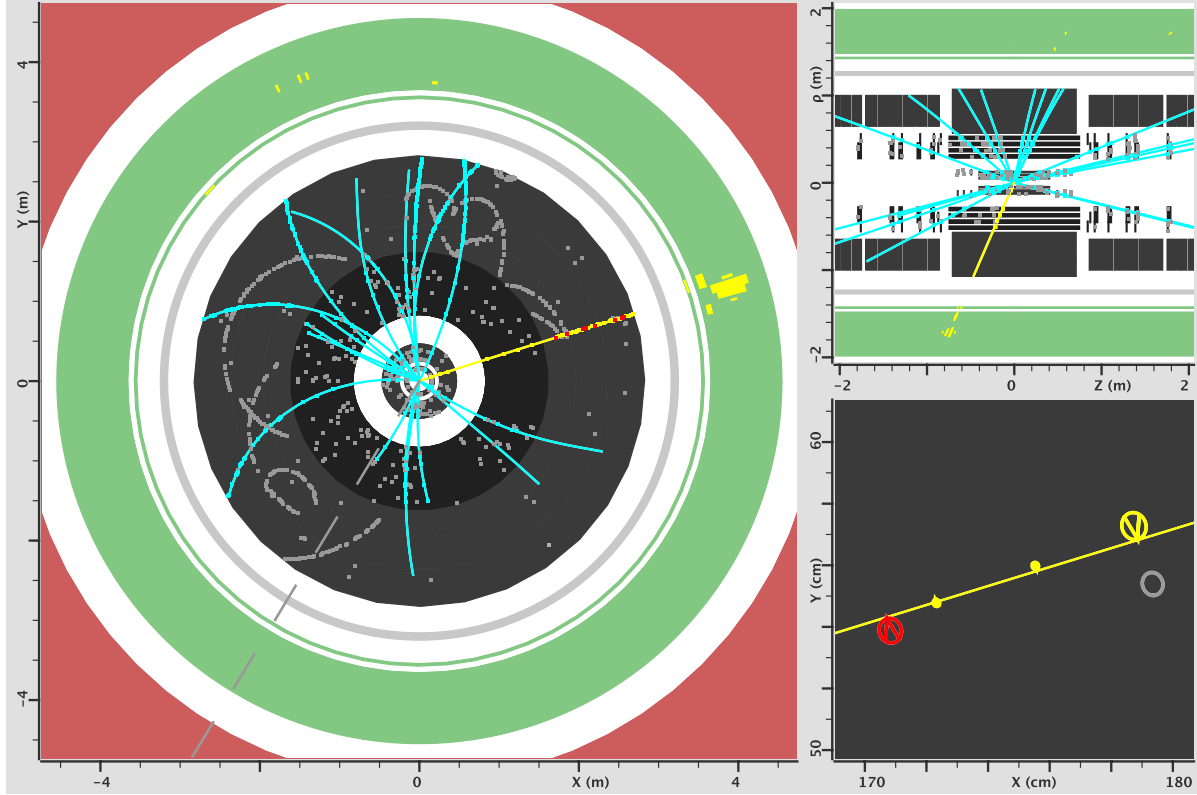


**Figure 5.8:** One of the first  $W^+ \rightarrow e^+ \nu_e$  candidates recorded by ATLAS. The  $Y/X$  view (left) shows the inner detector and electromagnetic calorimeter. The  $\rho/Z$  view (top right) shows a longitudinal view of the same region. The second inset (bottom left) shows a detailed view of the electron track passing through the TRT.

displayed in the same color as the track. The high threshold hits in the TRT, resulting from the transition radiation photons, are shown in red. A zoom of the first four TRT hits on the electron track is shown on the bottom right. This inset shows the TRT drift circles and the electron track. The left-right ambiguity that results from a drift circle measurement is resolved by the pattern recognition software. The decision of the pattern recognition is indicated by the arrows inside the drift circles, pointing toward the track.

Figure 5.9 shows a  $Z \rightarrow \mu\mu$  candidate recorded on the 10<sup>th</sup> of May. The negatively charged muon (orange) has a transverse momentum of 27 GeV. The positively charged muon (magenta) has a transverse momentum of 45 GeV. The invariant mass of the two muons is  $m_{\mu\mu} = 87$  GeV.

On the left, the two muons are shown in the  $\rho/Z$  view. The top right plot shows the  $Y/X$  view. The  $\mu^+$  leaves the interaction region in the forward direction, at  $\eta = 2.2$ . It can be seen to traverse the CSCs in the inner endcap station and the TGCs and MDT

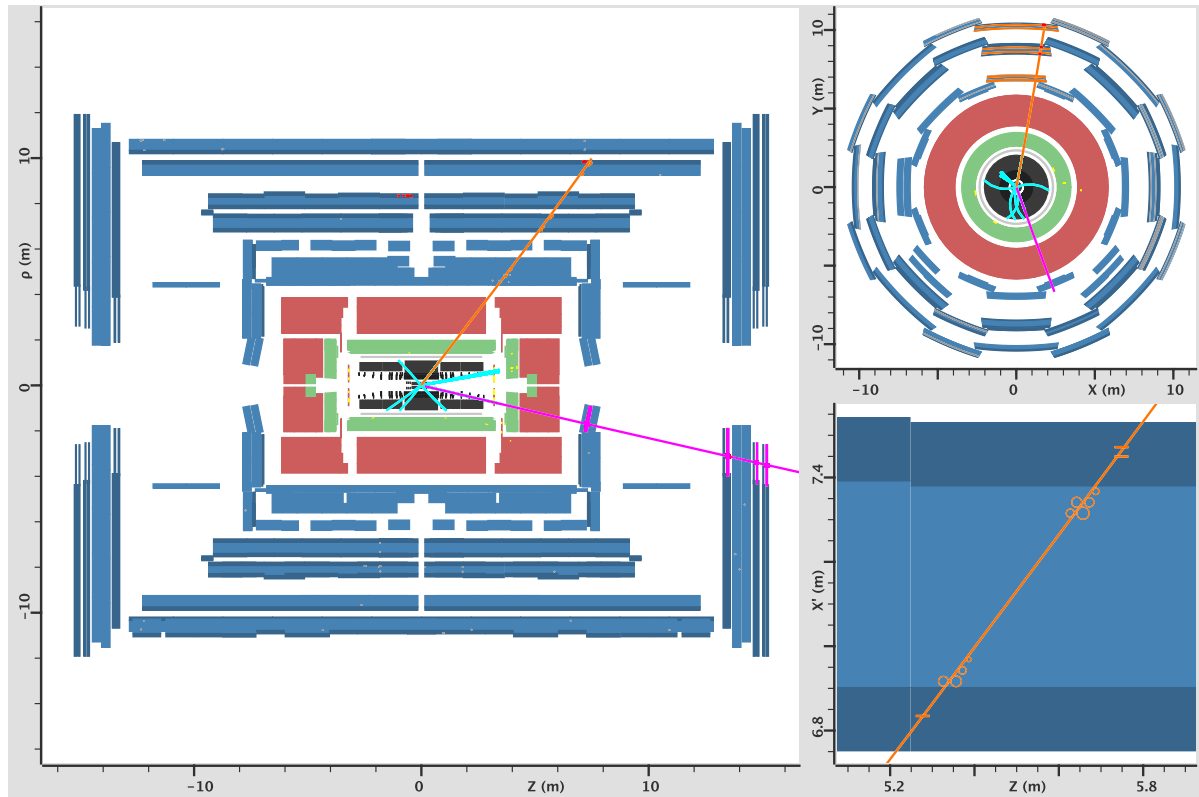


**Figure 5.9:** A  $Z^0 \rightarrow \mu^+\mu^-$  candidate. The  $\rho/Z$  view (left) shows one muon in the barrel (orange) and one in forward direction (magenta). The  $Y/X$  view on the top right shows a transverse view of the two muons. The zoomed view (bottom right) shows the  $X'/Z$  view of one of the muons traversing the middle muon station.

chambers in the middle endcap station. The outer endcap station is not shown in this picture. The  $\mu^-$ , which is more central, traverses the three barrel stations. The bottom right plot shows an  $X'/Z$  view of this muon as it traverses the middle barrel station. It shows an MDT chamber (light blue) with RPCs on both sides (dark blue). Three RPC trigger hits are visible, as well as nine drift circle measurements in the two MDT multilayers.

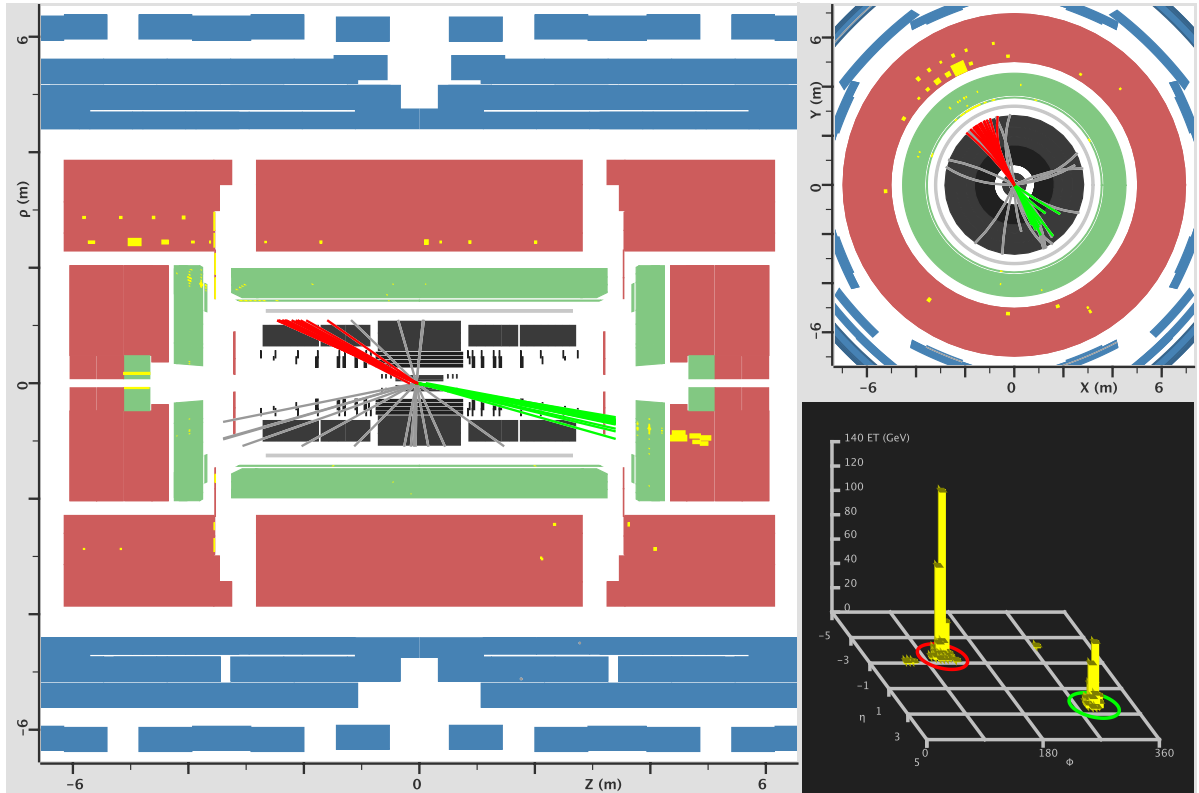


**Figure 5.10:** This event holds the record for the highest dijet invariant mass during the first six months of operation. The invariant mass of the two jets is  $m_{jj} = 2.55$  TeV. The event is shown in the  $\rho/Z$  projection (left) and  $Y/X$  projection (top right). The bottom right display shows the calorimeter cell energies as towers in a 3-dimensional representation.

On the 4<sup>th</sup> of July, ATLAS registered a dijet event with an invariant mass of 2.55 TeV. This event is shown in figure 5.10. The two jets have an  $E_T$  of 410 GeV (red) and 315 GeV (green). No other jets are present in the event with an  $E_T$  of more than 20 GeV. Also, the jets are well balanced, the missing transverse energy is only 45 GeV.

The  $\rho/Z$  view, displayed on the left, shows how the red jet deposited its energy in the transition region between the barrel and endcap calorimeters. The green jet, on the other hand, is fully contained in the electromagnetic and hadronic endcap calorimeters.

The top right plot shows the  $Y/X$  view of this event. The red jet can be visualized very well in this projection, but since the endcap calorimeters are not shown, the plot is less suitable for the green jet. The bottom right plot, shows the so-called *Lego Plot*. This is a three dimensional representation of an  $\eta\phi$  histogram, showing the energy deposits in the calorimeter cells. The colored circles indicate the positions of the reconstructed jets.

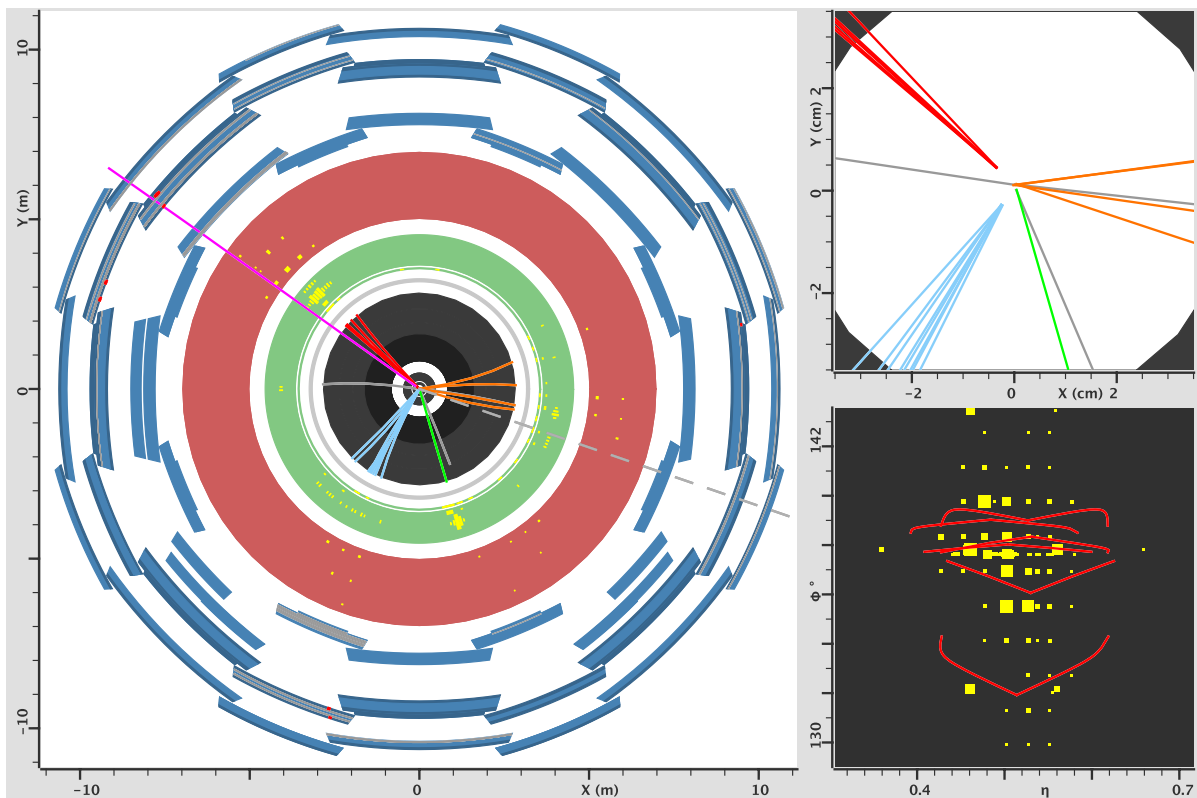


**Figure 5.11:** The first  $t\bar{t}$  candidate recorded by ATLAS with two  $b$ -tagged jets. The  $Y/X$  view (left) provides an overview of the event. Another  $Y/X$  view (top right) zooms into the vertex region to show the displaced vertices of the  $b$ -jets. The V-Plot (bottom right) shows one of the  $b$ -jets in  $\phi\text{-}\eta$ .

Figure 5.11 shows the first  $t\bar{t}$  candidate observed in ATLAS that has two  $b$ -tagged jets. It was recorded on the 8<sup>th</sup> of August. The  $b$ -jets, shown in red and blue, have an  $E_T$  of 175 and 48 GeV respectively. The red  $b$ -jet also contains a 53 GeV muon, shown in magenta. Furthermore, there is an isolated 55 GeV electron (green) and 108 GeV missing transverse energy (gray dashed line), presumably from the leptonic decay of a  $W^-$  boson.

The  $Y/X$  view on the left provides a general overview of the event. The inset at the top right zooms into the interaction region, inside the innermost layer of the Pixel detector. In this view, the displaced vertices of the  $b$ -decays can be seen very well. The bottom inset shows the tracks from one of the  $b$ -jets in the V-Plot. The fact that these tracks do not originate from the primary vertex can be seen by the deformation of the arms of the ‘V’-shaped tracks.

## 5.7 Conclusions and outlook

Visual investigation of events is an important tool for understanding and debugging the hardware and software at the different stages of data taking. The data oriented projections used in Atlantis prove to be an efficient way to provide the physicists with the necessary information.

The intuitive  $Y/X$  and  $\rho/Z$  projections provide simple and clear pictures for publications. When combined with the other projections, a good visualization is possible for all of the subdetectors in ATLAS. The  $\phi/\eta$  projection, or V-Plot, caters to the needs of the expert physicist who requires a complete and detailed picture of an event in order to understand the physics processes involved. This plot allows the user to check reconstructed tracks against inner detector hits and calorimeter energy deposits in one view. The characteristics of the ‘V’-shaped tracks provide a fast way to recognize track properties and possible secondary vertices. This is complemented by the tools Atlantis provides to fit vertices and calculate invariant masses, helping the user in determining the physics content of an event.

Visualization software has proven to be an invaluable tool in ATLAS and this will most likely remain so during the lifespan of the experiment. In the startup phase, the development of Atlantis has been focused mainly on its use as a monitoring tool. Over the next few years, however, the focus will most likely shift towards software debugging and assisting the physics analyses.

# Chapter 6

## Search for supersymmetry using $Z^0$ bosons

### 6.1 Introduction

In supersymmetric models where R-parity is conserved, supersymmetric particles can only be produced in pairs and they can only decay into another supersymmetric particle. As a consequence, there must be a lightest supersymmetric particle (LSP) that cannot decay into other particles and has to be stable..

Due to the strength of the QCD coupling, the production of supersymmetric particles will be dominated by QCD processes as soon as this is kinematically allowed. Therefore, a typical supersymmetric event starts out with a squark/gluino pair which is created in the initial collision. These heavy particles then cause a cascade decay to ever lighter supersymmetric particles, producing many high energy jets and possibly leptons in the process. At the end of the cascade, the supersymmetric particles have decayed into the LSP, which escapes unseen. An example of such a cascade is shown in figure 6.1.

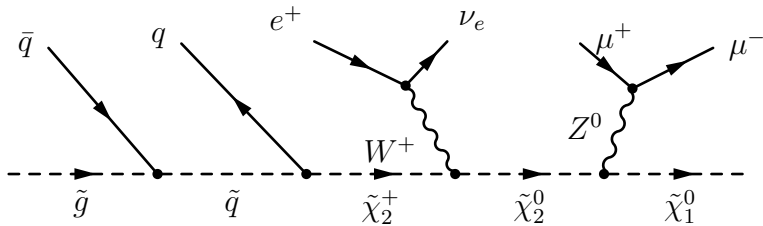


**Figure 6.1:** Feynman diagram showing a possible cascade decay of a gluino.

Assuming that the LSP is the lightest neutralino,  $\tilde{\chi}_1^0$ , an interesting decay process that may occur in the final step of the cascade is the decay of the next-to-lightest into

the lightest neutralino by emitting a Standard Model  $Z$  boson, with the  $Z$  boson in turn decaying leptonically. The lepton pair, which allows for a reconstruction of the  $Z^0$  invariant mass, provides a very powerful instrument to separate this channel from the background.

This chapter will present an analysis which focuses on the case where the  $Z^0$  decays into a muon pair, thus the channel:

$$\tilde{\chi}_2^0 \rightarrow Z^0 \tilde{\chi}_1^0 \rightarrow \mu^+ \mu^- \tilde{\chi}_1^0.$$

In particular, the potential of this channel to lead to a discovery of supersymmetry will be discussed.

Previous studies into this channel have been performed for  $Z^0 \rightarrow e^+ e^-$  [81], however the case of  $Z^0 \rightarrow \mu^+ \mu^-$  was not included. Moreover a full optimization for this particular channel has not yet been done in ATLAS. Similar studies for the CMS experiment [82–84] show that for some points in parameter space a discovery can be achieved with less than  $1 \text{ fb}^{-1}$  of data at 14 TeV.

## 6.2 Monte Carlo datasets

The characteristics of the signal events in question are several hard jets, an opposite sign muon pair with an invariant mass around the  $Z^0$  peak and considerable missing transverse energy. The background study will focus on the processes that mimic this signature, but differ on one of these properties. Mismeasurements, bad reconstruction or just the large cross sections involved can cause these events to pass the signal selection. Backgrounds that, in case of ideal reconstruction, would fail two or more of the selection cuts are expected to be negligible.

The background samples that were used are listed in table 6.1. The samples are all part of the official ATLAS 10 TeV Monte Carlo production of 2008. The majority of the samples have been simulated using the ATLFAST-II [62] fast detector simulation. For some samples, namely  $ZZ$ ,  $WW$  and  $W + b\bar{b} + N$  jets, no fast simulation samples were available and full simulation was used instead. The fully simulated samples contain fewer events, therefore the statistical uncertainty is somewhat larger. This substitution is not expected to have any effect on the analysis. Some samples, such as  $Z \rightarrow \mu\mu + N$  jets, have been split at generator level by the number of partons they contain. These samples are merged again using their respective cross sections and only the complete sample is used in the analysis.

**Table 6.1:** Background Monte Carlo samples used in the analysis. For every process the sample identifier in the official production, the generator which was used, the number of events and the next-to-leading order cross section is listed.

Sample name	Identifier	Generator	Events	Cross section (pb)
$t\bar{t}$ ( $\geq 1\ell$ )	105200	MC@NLO	4,989,425	205.48
$WW$ ( $\geq 1\ell$ )	105985	Herwig	50,000	15.61
$ZZ$ ( $\geq 1\ell$ )	105986	Herwig	10,000	1.36
$WZ$ ( $\geq 1\ell$ )	105987	Herwig	499,999	3.47
$W + b\bar{b} + N$ jets	106280	Alpgen	15,500	5.13
	106281	Alpgen	15,457	5.01
	106282	Alpgen	8,953	2.89
	106283	Alpgen	5,000	1.61
$Z \rightarrow \mu\mu + N$ jets	107660	Alpgen	270,500	900.20
	107661	Alpgen	62,000	205.20
	107662	Alpgen	208,500	69.40
	107663	Alpgen	65,000	21.60
	107664	Alpgen	18,500	6.10
	107665	Alpgen	5,500	1.70
$W \rightarrow \mu\nu + N$ jets	107690	Alpgen	3,048,663	10,125.70
	107691	Alpgen	562,324	2,155.50
	107692	Alpgen	1,874,381	682.30
	107693	Alpgen	563,498	202.00
	107694	Alpgen	153,000	55.50
	107695	Alpgen	44,500	16.30
$Z \rightarrow \mu\mu + b\bar{b} + N$ jets	109305	Alpgen	1,199,789	12.28
	109306	Alpgen	599,902	4.92
	109307	Alpgen	160,000	1.92
	109308	Alpgen	40,000	0.94

In order to obtain an overall background sample of the desired integrated luminosity  $\mathcal{L}$ , all the Monte Carlo samples are weighted according to their cross sections. The weight  $w_i$  of event  $i$  is given by:

$$w_i = \frac{\sigma_i}{N_i} \times \mathcal{L}, \quad (6.1)$$

where  $\sigma_i$  is the cross section of the sample the event belongs to and  $N_i$  the number of events the sample contains. Samples can be merged by weighting events in every subsample by their respective cross sections. After assigning event weights, the statistical uncertainty on an observed number of Monte Carlo events is given by

$$\sigma = \sqrt{\sum_i w_i^2}. \quad (6.2)$$

For readability of the results, some of the background samples will be combined. The  $WW$ ,  $ZZ$  and  $WZ$  samples are summed with their respective cross sections and combined into the diboson sample. Similarly,  $Z + \text{jets}$  will be used to refer to the combination of  $Z \rightarrow \mu\mu + N \text{jets}$  and  $Z \rightarrow \mu\mu + b\bar{b} + N \text{jets}$  and  $W + \text{jets}$  will be used to refer to the combination of  $W + b\bar{b} + N \text{jets}$  and  $W \rightarrow \mu\nu + N \text{jets}$ .

### 6.3 Parameter space analysis

The  $\tilde{\chi}_2^0$  particle is produced abundantly in most supersymmetric cascade decays. However, the decay of this neutralino to  $\tilde{\chi}_1^0$  by emitting a  $Z$  boson is limited to a small region in parameter space. Whether this process takes place or not depends strongly on the mass difference between the two neutralinos. This difference has to be greater than the  $Z^0$  boson mass for the channel to be kinematically allowed. However, when this mass difference becomes larger than the mass of the Higgs boson, a new decay mode opens up:  $\tilde{\chi}_2^0 \rightarrow h^0 \tilde{\chi}_1^0$ . Since the coupling of the neutralino to the Higgs boson is strong, this decay mode is favored and the decay via a  $Z$  boson will be heavily suppressed. Therefore, the region in parameter space where this channel plays an important role is the region where

$$m_Z < m_{\tilde{\chi}_2^0} - m_{\tilde{\chi}_1^0} < m_h.$$

To visualize the area of interest, a scan of the  $m_0$ - $m_{1/2}$  plane was performed using ISAJET [28] version 7.75. Figure 6.2 shows the branching ratio of the process  $\tilde{\chi}_2^0 \rightarrow Z^0 \tilde{\chi}_1^0$  when varying the universal scalar mass  $m_0$  and the universal gaugino mass  $m_{1/2}$  in steps of  $\Delta m_0 = 5 \text{ GeV}$  and  $\Delta m_{1/2} = 2 \text{ GeV}$ . The remaining mSUGRA parameters were kept

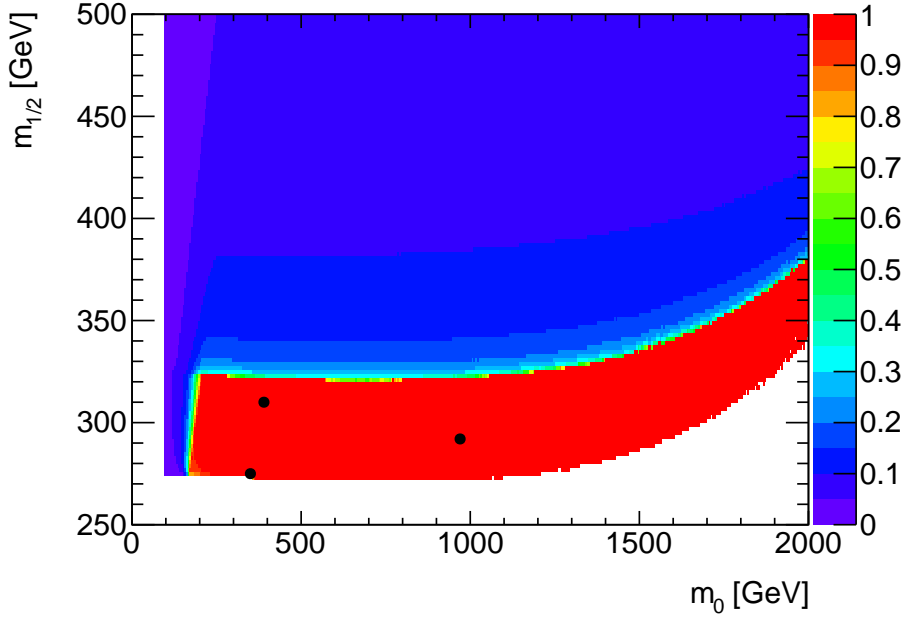


**Figure 6.2:** Branching ratio of the process  $\tilde{\chi}_2^0 \rightarrow Z^0 \tilde{\chi}_1^0$  as a function of the mSUGRA parameters  $m_0$  and  $m_{1/2}$ . The remaining parameters are fixed at  $\tan \beta = 10$ ,  $A_0 = 0$  GeV and  $\text{sign } \mu > 0$ .

constant at  $\tan \beta = 10$ ,  $A_0 = 0$  GeV and  $\text{sign } \mu > 0$ . The red band clearly shows the region where the above mass condition is satisfied, leading to a branching ratio that approaches unity. It also shows that the branching ratio decreases rapidly once the Higgs channel opens up for higher  $m_{1/2}$ . It should be noted, however, that the exact location of the region with high branching ratio depends on the mass spectrum generator used, especially for higher values of  $m_0$ . For a detailed comparison of the different spectrum generators see [85].

In order to demonstrate the methods in this analysis, a Monte Carlo signal sample is needed with its parameters chosen such that  $\text{BR}(\tilde{\chi}_2^0 \rightarrow Z^0 \tilde{\chi}_1^0) > 0.95$ . None of the mSUGRA points of the official ATLAS production [86] are located in this region of parameter space. However, the ATLAS SUSY working group has produced a grid of mSUGRA points [87]. For  $\tan \beta = 10$  and  $A_0 = 0$  GeV the signal grid consists of 40 points in the area  $m_0 < 2.5$  TeV and  $m_{1/2} < 500$  GeV, arranged along radial lines in the  $m_0$ - $m_{1/2}$  plane. This grid contains three points in the desired region, which will be used as signal for optimizing the selections for this analysis. The location of these three points has been indicated by the dots in figure 6.2 and their parameters are summarized in table 6.2.

**Table 6.2:** mSUGRA points from the signal grid where  $\text{BR}(\tilde{\chi}_2^0 \rightarrow Z^0 \tilde{\chi}_1^0) > 0.95$ .

Point	$m_0$ (GeV)	$m_{1/2}$ (GeV)	$A_0$ (GeV)	$\tan \beta$	sign $\mu$	$\sigma$ (pb)
1	350	275	0	10	+	5.42
2	390	310	0	10	+	2.81
3	970	292	0	10	+	1.35

## 6.4 Event selection

The analysis presented here uses the physics objects produced by the standard ATLAS reconstruction. To accommodate the many different analyses that are performed in the experiment, the object definitions are fairly loose. At the analysis level, more strict definitions can be imposed. In this analysis the objects have to meet the following kinematic and identification criteria:

**Muon** Only combined muons are considered, i.e. muons that have been reconstructed both in the inner tracker and the muon spectrometer. Their transverse momentum has to satisfy  $p_T > 20$  GeV. Furthermore the muon has to be isolated; in a cone of  $\sqrt{\Delta\phi^2 + \Delta\eta^2} < 0.2$  the excess energy deposit in the calorimeter has to be less than 10 GeV.

**Electron** The electrons are not used in the primary analysis, but only for the definition of a control sample. This permits a very conservative object selection. Electrons are required to be identified as tight isolated electrons. Similarly to muons,  $p_T > 20$  GeV is required. In the region between the barrel and endcap calorimeters,  $1.37 < |\eta| < 1.52$ , electron measurement is more complicated, therefore electrons in this region are rejected.

**Jet** For jet reconstruction the cone algorithm is used with a cone size of 0.4 and topological cell clustering. For their momentum,  $p_T > 20$  GeV is required.

**Missing transverse energy** The refined final missing  $E_T$  is used.

The event selection is done in two steps. First, a preselection is performed to reject event topologies that do not match the desired signal. The preselection requirements for an event are:

- It contains at least three jets;

- It contains two or more muons;
- The two highest  $p_T$  muons have opposite charge.

Selecting only the two highest  $p_T$  muons is done to avoid biasing the dimuon invariant mass spectrum. The number of signal events with more than two muons passing the selection criteria is small, so the loss of efficiency resulting from this selection is negligible.

In addition to the signal event selection, a separate control sample is obtained by repeating the preselection with one of the two muons replaced by an electron. Signal events are excluded from the control sample. The control sample will be used later to provide an estimate on the number of uncorrelated muon pairs.

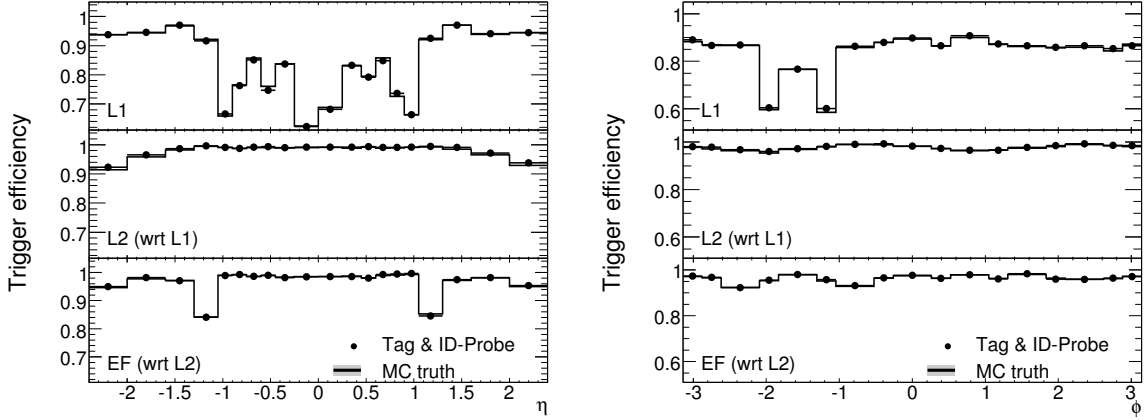
## 6.5 Trigger efficiency

The Monte Carlo data samples that were used do not include a simulation of the trigger response. In order to determine the effect of the trigger efficiency on the results of this analysis, an estimation of the efficiencies will be performed based on the CSC performance studies [88]. In the CSC notes, the trigger efficiency for the  $Z^0 \rightarrow \mu^+\mu^-$  decay is evaluated using the tag and probe method. Using a single muon trigger a tag muon is obtained. A second reconstructed muon, the probe muon, is then sought for that combines with the tag muon into a  $Z$  boson. In case a probe muon is found, it is evaluated whether or not it fired the muon trigger under consideration. This provides an estimate of the trigger's efficiency. The most important advantage of this method is that it can be easily performed on real and simulated data.

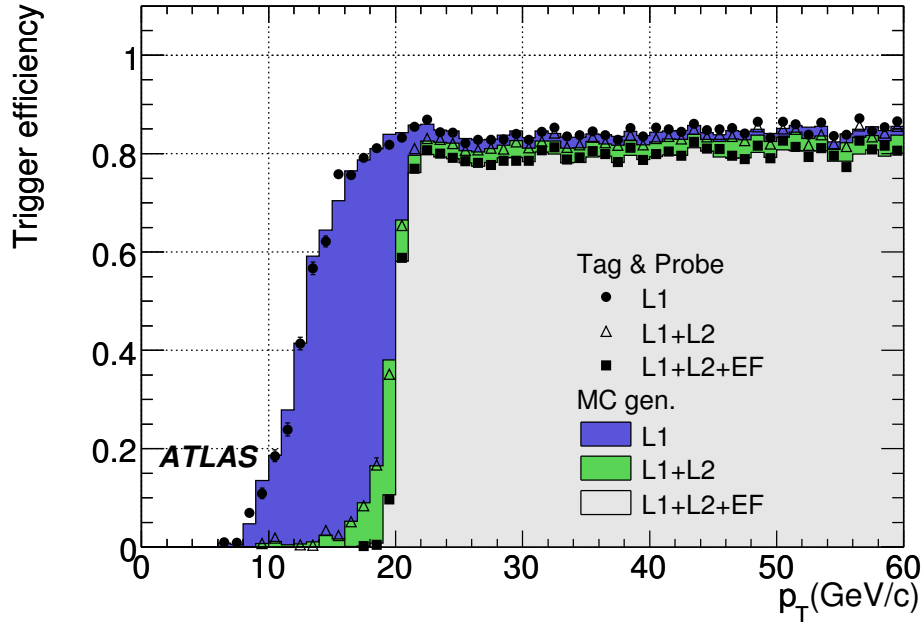
The trigger efficiency obtained for the 20 GeV single muon trigger (`mu20`) using this method is shown in figure 6.3. At L1 the loss of efficiency is mainly caused by the geometrical coverage of the trigger chambers. For example at  $\eta = 0$  there is a cabling duct and the support structure for the calorimeters is located around  $\phi = -\pi/2$ . Furthermore, a loss of efficiency at EF level can be seen in the region between the barrel and the end cap muon spectrometer. This is caused by inhomogeneities in the magnetic field that affect the track reconstruction performance. The overall `mu20` trigger efficiency is  $79.73 \pm 0.06$  (stat)  $\pm 0.58$  (syst) % [88].

Figure 6.4 shows the turn-on curve of the `mu20` trigger. At event filter level, the turn-on curve rises very steeply. The  $p_T$  dependence of the trigger efficiency for  $p_T > 20$  GeV is therefore not taken into account in this analysis.

The overall muon trigger efficiency is to a large extent determined by geometrical effects. Most notably is the dependence on the pseudorapidity,  $\eta$ . Since the  $\eta$  distribution



**Figure 6.3:** Trigger efficiencies for mu20 at the different trigger levels, as a function of  $\eta$  (left) and  $\phi$  (right). The L1 efficiency is calculated with respect to all reconstructed muons, the higher levels are calculated with respect to the previous level. A comparison with Monte Carlo truth is made to prove the validity of the tag and probe method. Figure prepared for [88], but not included in the final note.



**Figure 6.4:** Turn on curve for the mu20 trigger. The values obtained using the tag and probe method are shown for all trigger levels. This is again compared to Monte Carlo truth information. [88]

of reconstructed muons is similar in the signal and background samples, the trigger efficiency is not expected to influence the signal to background ratio. Furthermore, the variables used in this analysis show no significant dependence on the  $\eta$  coordinate of the individual muons. It is assumed in this chapter that the effect of the trigger efficiency can be parametrized by an overall efficiency factor. Moreover, for fake muons that pass the final event selection, the trigger rejection is not expected to be more efficient than for real muons. Therefore the same efficiency factor is applied to backgrounds that do not contain a real  $Z$  boson.

The analysis presented in this chapter requires the presence of two muons within the acceptance of the detector. It is assumed that, due to the presence of at least three jets in the event selection, the muons can be considered as independent. Calculating the probability of at least one of the muons passing the `mu20` trigger then leads to an event trigger efficiency of:

$$\epsilon_{\text{trigger}} = 95.89 \pm 0.04 \text{ (stat)} \pm 0.24 \text{ (syst)} \%. \quad (6.3)$$

This factor has been applied as a correction factor to the event count for all results presented in this chapter.

## 6.6 Signal characteristics

The characteristics of the signal allow the definition of an event selection that is highly optimized for signal events, while rejecting most of the background. As an example, the first point defined in table 6.2 will be considered. Figure 6.5 shows the invariant mass of the two highest  $p_T$ , oppositely charged muons, after the event preselection. For the signal, the  $Z^0$  mass peak is clearly visible, but it also shows large tails which contain mostly other leptonic SUSY decays. The background is composed of a part that peaks (dominated by  $Z + \text{jets}$ ) and a continuum (dominated by dileptonic  $t\bar{t}$ ).

Figure 6.6 shows the distribution of the missing transverse energy in signal and background events. The background is concentrated on the lower end of the spectrum and falls off very rapidly with increasing  $\cancel{E}_T$ . The signal, on the other hand, remains nearly constant over the full range, with the highest and lowest values differing by at most one order of magnitude. Even after only the preselection criteria are applied, the signal to background ratio is larger than unity for  $\cancel{E}_T > 250 \text{ GeV}$ .

Another distinguishable feature, often used to identify supersymmetric decay cascades, is the presence of several high- $p_T$  jets. Figure 6.7 shows the transverse momentum of the fourth highest  $p_T$  jet, for signal and background events that have at least 4 jets

that pass the preselection criteria. It can be seen that the jet  $p_T$  spectrum falls off more slowly with  $p_T$  for the signal sample than for the combined backgrounds. So, on average, signal events contain more hard jets than background events. This is further illustrated by figure 6.8. In this figure, the same procedure is repeated, but now for the  $p_T$  of the fifth highest  $p_T$  jet and requiring at least 5 jets that pass the preselection criteria.

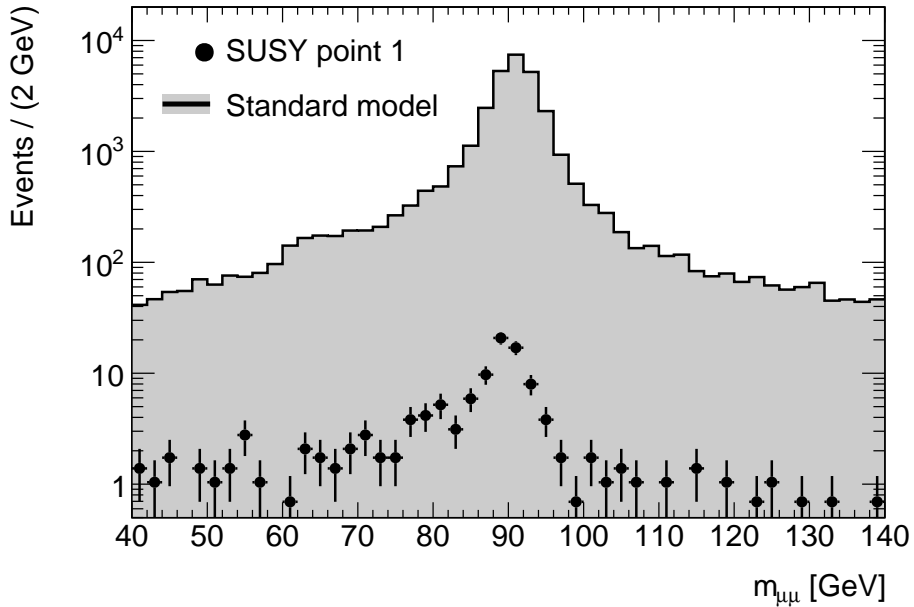


**Figure 6.5:** Di-lepton invariant mass distribution of all events after preselection.

The degree of certainty with which the signal can be observed above a remaining background level is expressed by the measure of the signal significance. The signal significance quantifies how much the background should have to deviate from the expected value in order to produce the observed signal. In general, a significance of 5 is required to claim the discovery of a new phenomenon. This means that the measured value is more than 5 standard deviations above the expected background level. In the case of a Gaussian distribution, the probability of such an excess occurring randomly is about 1 in 3 million.

The measured event counts are distributed according to a Poisson distribution. Hence, when observing  $n$  events, the likelihoods of the SUSY and the Standard Model only hypotheses are given by:

$$\mathcal{L}_{SUSY} = \frac{(s+b)^n e^{-(s+b)}}{n!}, \quad \mathcal{L}_{SM} = \frac{b^n e^{-b}}{n!}, \quad (6.4)$$

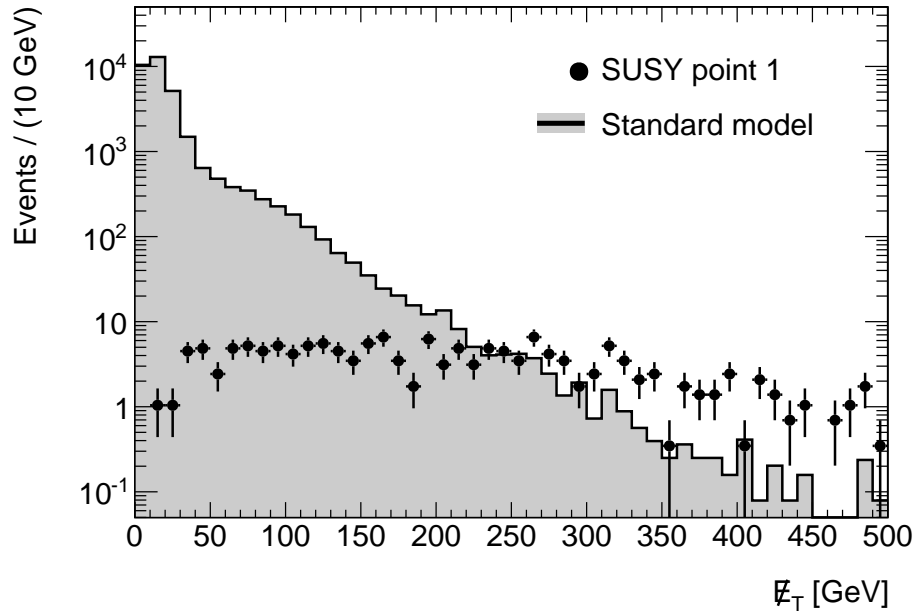


**Figure 6.6:** Missing  $E_T$  distribution of all events after preselection.

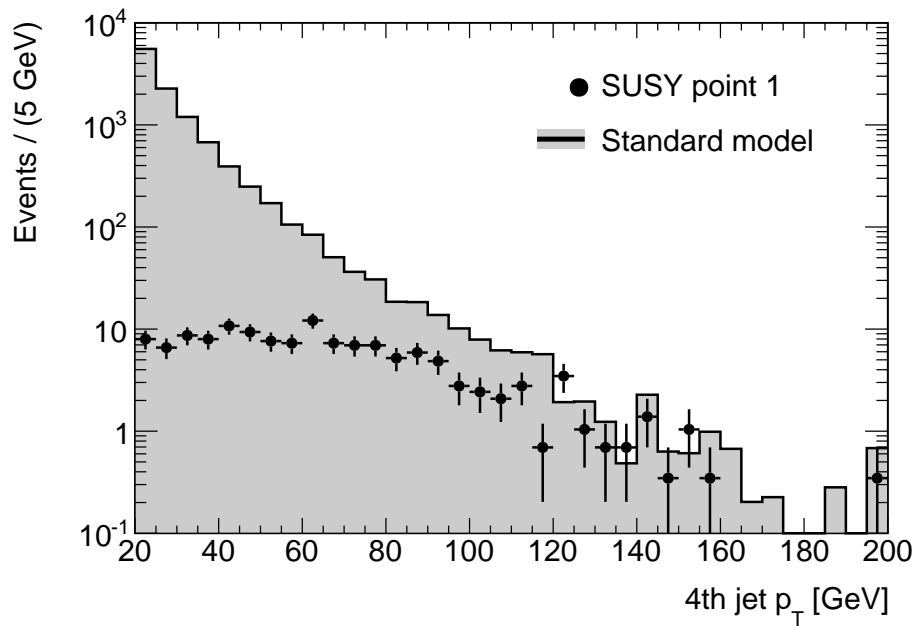


**Figure 6.7:** Transverse momentum of the fourth highest momentum jet after preselection. Events that do not contain at least 4 jets with  $p_T > 20$  GeV are not shown.

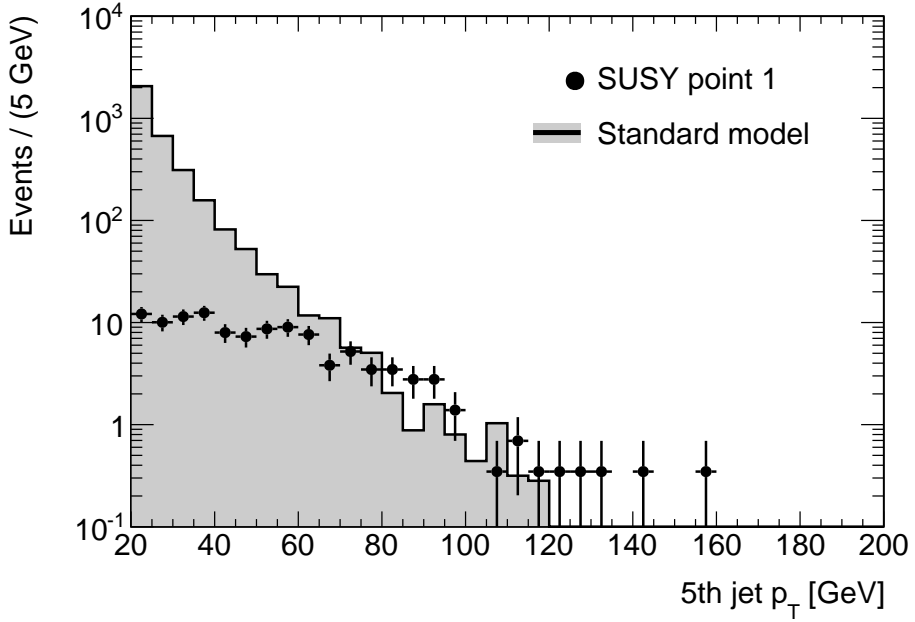


**Figure 6.8:** Transverse momentum of the fifth highest momentum jet after preselection. Events that do not contain at least 5 jets with  $p_T > 20$  GeV are not shown.

with  $b$  the expected number of background and  $s$  the expected number of signal events. Taking the observed number of events as  $n = s+b$ , the likelihood ratio  $Q = \mathcal{L}_{SUSY}/\mathcal{L}_{SM}$  leads to a significance estimator:

$$S_{cL} \equiv \sqrt{2 \ln Q} = \sqrt{2 \left( (s+b) \ln \left( 1 + \frac{s}{b} \right) - s \right)}. \quad (6.5)$$

For large statistics this estimator approaches the commonly used  $s/\sqrt{b}$ , however  $S_{cL}$  remains valid also for low statistics [82].

To evaluate the discovery potential, two methods will be discussed. The first is a simple event counting method based on the Monte Carlo data. The systematic uncertainties introduced by the use of Monte Carlo data constitute an important fraction of the overall uncertainty. In order to reduce this uncertainty, the second method is introduced. This is the simultaneous fit method, which uses a control sample to determine the background level from measured data instead of Monte Carlo simulation.

## 6.7 Counting method

The counting method is a fairly straightforward method. Using the characteristics of the signal discussed in the previous section, a set of selection cuts is devised. These cuts are then applied to the Monte Carlo samples. For each of the points in SUSY parameter space, the signal significance is calculated. The cuts are optimized by varying them until a maximum value of the significance is found.

### 6.7.1 Cut optimization

For the signal selection, the dilepton invariant mass is required to be within a 20 GeV window around the mass of the  $Z$  boson. This rejects most of the events that do not contain a true  $Z$  boson. Additional cuts are then imposed on the jet multiplicity, the jet transverse momentum and the missing transverse energy. To optimize the values of the latter three, a scan is performed for the missing transverse energy cut. The value of the missing energy cut is varied in the range of 50–200 GeV, while the remaining cuts are kept constant. This procedure is repeated requiring different numbers of jets and different jet transverse momenta.

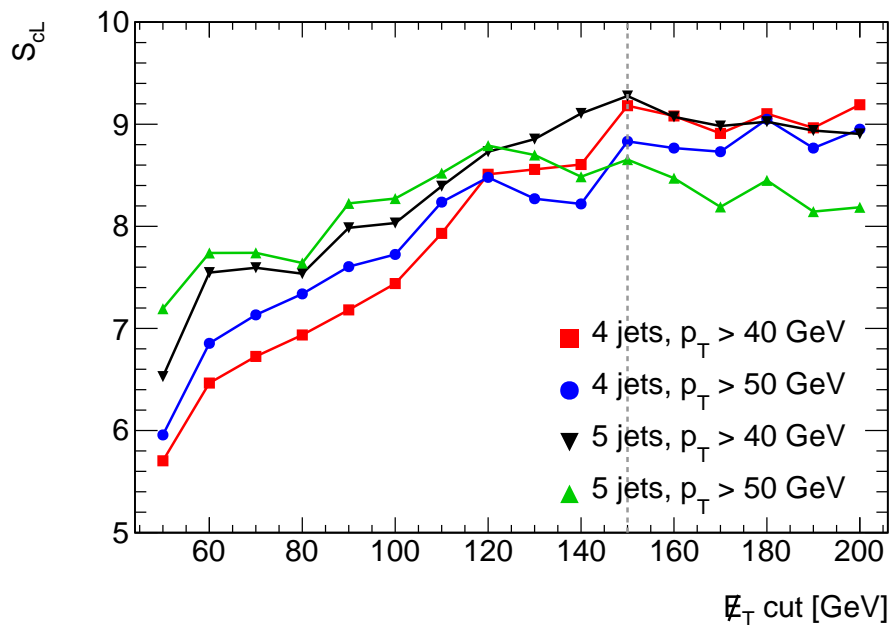


**Figure 6.9:** Optimization curves for SUSY point 1. The signal significance estimator  $S_{cL}$  is shown as a function of the missing transverse energy cut for different jet cuts. The optimal value for the missing transverse energy cut is indicated by the dashed vertical line.

**Table 6.3:** Cut flow after optimization of cuts for SUSY point 1. The number of events corresponds to an integrated luminosity of  $2\text{ fb}^{-1}$ . Note that no events from the  $W + \text{jets}$  sample passed the cut on missing transverse energy, therefore the event count is taken to be less than the weight of a single event.

Cut (GeV)	Point 1	$t\bar{t}$	$Z + \text{jets}$	$W + \text{jets}$	Diboson
Preselection	$156 \pm 7$	$3318 \pm 16$	$(294.8 \pm 2.0) \cdot 10^2$	$13 \pm 3$	$188 \pm 5$
$ m_{\mu\mu} - m_Z  < 10$	$74 \pm 5$	$506 \pm 6$	$(258.4 \pm 1.9) \cdot 10^2$	$4.0 \pm 1.6$	$158 \pm 5$
$\cancel{E}_T > 150$	$44 \pm 4$	$22.0 \pm 1.3$	$4.2 \pm 1.4$	$< 0.7$	$(36 \pm 7) \cdot 10^{-2}$
5 jets, $p_T > 40$	$22 \pm 3$	$1.4 \pm 0.3$	$< 4 \cdot 10^{-2}$	$< 0.7$	$(1.3 \pm 1.3) \cdot 10^{-2}$

Figure 6.9 shows the optimization curves obtained for the first signal point when requiring 4 or 5 jets with a minimum  $p_T$  of 40 or 50 GeV. The significance estimator  $S_{cL}$  is plotted as a function of the minimal required missing transverse energy. The four curves represent the different jet cuts. Table 6.3 shows the cut flow at the point of maximum  $S_{cL}$ . The cutflow shows that the  $|m_{\mu\mu} - m_Z| < 10$  GeV cut is less efficient for SUSY than it is for  $Z + \text{jets}$ . This is due to the fact that the SUSY sample also contains other dimuon final states, while for  $Z + \text{jets}$  virtually all muon pairs originate from the decay of a  $Z$  boson.

The figures 6.10 and 6.11 show the optimization of the cuts for the two other signal points. The cutflow for the optimal selection is summarized in tables 6.4 and 6.5. For signal points 1 and 2 the maximal significance is obtained for  $\cancel{E}_T > 150$  GeV and 5 jets with  $p_T > 40$  GeV. For point 3, the optimal jet  $p_T$  cut is slightly higher: 5 jets with  $p_T > 50$  GeV.

### 6.7.2 Systematic uncertainties

In the presence of systematic errors on the background estimate, the Poisson distribution in equation 6.4 should be convoluted with the probability distribution of the background estimate. This convolution can only be performed numerically. The significance obtained in this case, however, can be approximated by the estimator [82]:

$$S_{c12s} = 2 \left( \sqrt{s+b} - \sqrt{b} \right) \frac{b}{b + \Delta b^2}, \quad (6.6)$$

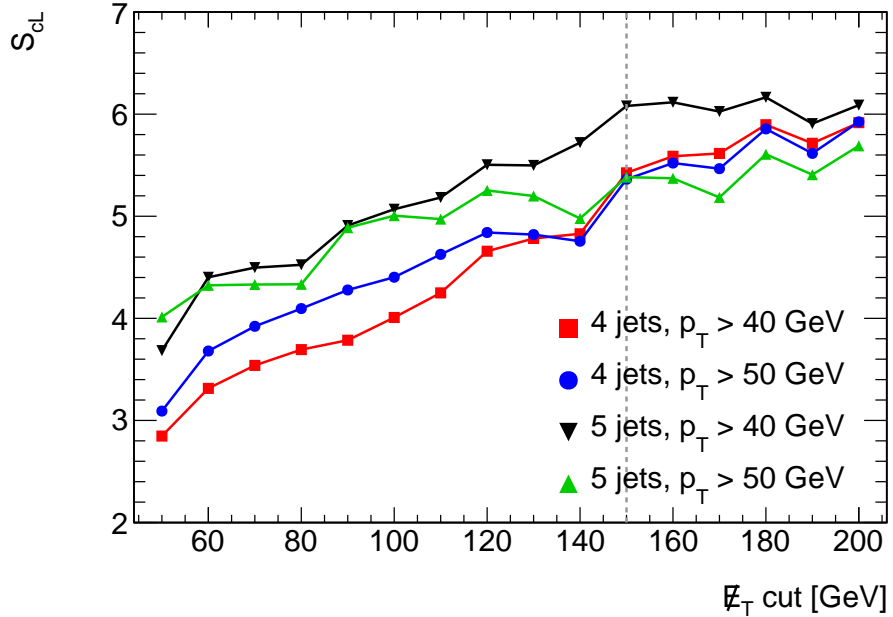


**Figure 6.10:** Optimization curves for SUSY point 2. The signal significance estimator  $S_{cL}$  is shown as a function of the missing transverse energy cut for different jet cuts. The optimal value for the missing transverse energy cut is indicated by the dashed vertical line.

**Table 6.4:** Cut flow after optimization of cuts for SUSY point 2 and an integrated luminosity of  $2 \text{ fb}^{-1}$ .

Cut (GeV)	Point 2	$t\bar{t}$	$Z + \text{jets}$	$W + \text{jets}$	Diboson
Preselection	$76 \pm 4$	$3318 \pm 16$	$(294.8 \pm 2.0) \cdot 10^2$	$13 \pm 3$	$188 \pm 5$
$ m_{\mu\mu} - m_Z  < 10$	$35 \pm 3$	$506 \pm 6$	$(258.4 \pm 1.9) \cdot 10^2$	$4.0 \pm 1.6$	$158 \pm 5$
$\cancel{E}_T > 150$	$23.5 \pm 2.1$	$22.0 \pm 1.3$	$4.2 \pm 1.4$	$< 0.7$	$(36 \pm 7) \cdot 10^{-2}$
5 jets, $p_T > 40$	$12.2 \pm 1.5$	$1.4 \pm 0.3$	$< 4 \cdot 10^{-2}$	$< 0.7$	$(1.3 \pm 1.3) \cdot 10^{-2}$

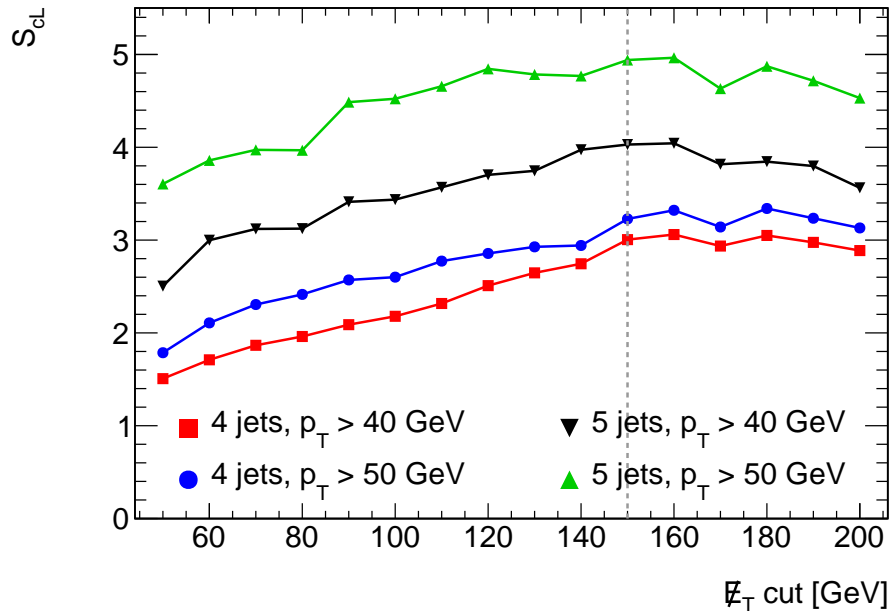


**Figure 6.11:** Optimization curves for SUSY point 3. The signal significance estimator  $S_{cL}$  is shown as a function of the missing transverse energy cut for different jet cuts. The optimal value for the missing transverse energy cut is indicated by the dashed vertical line.

**Table 6.5:** Cut flow after optimization of cuts for SUSY point 3 and an integrated luminosity of  $2 \text{ fb}^{-1}$ .

Cut (GeV)	Point 3	$t\bar{t}$	$Z + \text{jets}$	$W + \text{jets}$	Diboson
Pre-Selection	$32.0 \pm 1.7$	$3318 \pm 16$	$(294.8 \pm 2.0) \cdot 10^2$	$13 \pm 3$	$188 \pm 5$
$ m_{\mu\mu} - m_{Z^0}  < 10$	$18.6 \pm 1.3$	$506 \pm 6$	$(258.4 \pm 1.9) \cdot 10^2$	$4.0 \pm 1.6$	$158 \pm 5$
$\cancel{E}_T > 150$	$9.1 \pm 0.9$	$22.0 \pm 1.3$	$4.2 \pm 1.4$	$< 0.7$	$(36 \pm 7) \cdot 10^{-2}$
5 jets, $p_T > 50$	$6.8 \pm 0.8$	$0.55 \pm 0.21$	$< 4 \cdot 10^{-2}$	$< 0.7$	$(1.3 \pm 1.3) \cdot 10^{-2}$

with  $s$ ,  $b$  and  $\Delta b$  respectively the number of signal events, the number of background events and the systematic uncertainty on the number of background events.

The counting method is sensitive to several sources of systematic uncertainty. Firstly, the cross sections for the background processes. The background is dominated by dileptonic  $t\bar{t}$ , therefore the  $t\bar{t}$  cross section contributes most to the uncertainty on the background estimate. The dileptonic  $t\bar{t}$  cross section can be measured in ATLAS with an expected uncertainty of  $-19.5\% < \Delta\sigma/\sigma < 28.3\%$  for  $200\text{ pb}^{-1}$  of data [89]. With this amount of data, the uncertainty on the cross section is dominated by systematic errors. This uncertainty will be used to estimate the systematic uncertainty due to the  $t\bar{t}$  cross section in this analysis.

Other sources of systematic uncertainty are the variables that are used in the event selection, most importantly the jet energies and the missing transverse energy. To evaluate the effect of these systematic uncertainties, the energies of the reconstructed objects will be scaled up and down within their systematic error, after which the previously determined optimal cuts will be applied. The variation in the observed background level is then taken as the systematic uncertainty on the background level resulting from this particular source.

The uncertainty on the jet energy scale will be dominated by systematic errors after about  $300\text{ pb}^{-1}$  of data [90]. An uncertainty of  $\pm 5\%$  on the jet energy scale is assumed, similar to the CSC analyses [91]. This translates into a  $20\%$  uncertainty in the background level. In-situ methods for calibrating the scale of the  $\cancel{E}_T$  can achieve an expected precision of at least  $8\%$  with the first  $100\text{ pb}^{-1}$  of data [69], the resulting uncertainty on the background level is  $30\%$ .

The combination of these three systematic uncertainties leads to an additional uncertainty of about  $40\%$  on the predicted background level. This reduces the signal significance. However, it should be noted that the inclusion of the systematic uncertainty does not affect the position of the maximal significance as obtained earlier.

### 6.7.3 Obtained significance

Taking into account the systematic uncertainties, the statistical significance that can be obtained for the chosen signal samples using this method is listed in table 6.6. It is possible to make a  $5\sigma$  discovery for the first two points in SUSY parameter space with  $2\text{ fb}^{-1}$ . Due to the lower cross section in the third point, only a  $3.3\sigma$  signal excess can be observed in this case. More data would be needed for a conclusive discovery.

**Table 6.6:** Final significance results for the counting method when taking into account systematic uncertainties. The significance was calculated using the estimator  $S_{c12s}$ .

Sample	Signal events	Background events	Significance
Point 1	$22 \pm 3$	$1.4 \pm 0.3$ (stat) $\pm 0.6$ (syst)	5.9
Point 2	$12.2 \pm 1.5$	$1.4 \pm 0.3$ (stat) $\pm 0.6$ (syst)	4.1
Point 3	$6.8 \pm 0.8$	$0.57 \pm 0.21$ (stat) $\pm 0.23$ (syst)	3.6

## 6.8 Simultaneous background fit

In order to reduce the effect of systematic uncertainties, the use of Monte Carlo simulation has to be limited. The simultaneous fit method estimates the background level using a data-driven method, eliminating the need to use absolute numbers provided by the Monte Carlo simulation.

### 6.8.1 Irreducible backgrounds

From tables 6.3–6.5 it follows that the most important irreducible background in this analysis is  $t\bar{t}$ , in particular the dileptonic decay. In this channel, both of the top quarks decay into a bottom quark and a  $W$  boson. In the case where the decay of each of the  $W$  bosons produces a muon, such an event would pass the preselection criteria. Since the leptons in this case are not the decay products of a  $Z$  boson, this background is greatly reduced by the  $Z^0$  mass constraint which is applied. However, due to the large cross section of  $t\bar{t}$ , a considerable amount of events is still expected to be inside the  $Z^0$  mass window.

### 6.8.2 Data-driven background estimation

To incorporate the irreducible  $t\bar{t}$  background into the analysis, an effort will be made to estimate the number of background events passing the selection cuts using a data-driven method. The key ingredient in this estimation method is the fact that the  $W^\pm$  bosons in dileptonic  $t\bar{t}$  decay into opposite sign leptons, but not necessarily of the same flavor.

Theoretically,  $\text{BR}(W^\pm \rightarrow \mu^\pm)$  is approximately equal to  $\text{BR}(W^\pm \rightarrow e^\pm)$ . Therefore, the number of  $e\mu$  pairs produced in  $t\bar{t}$  should be about twice the number of  $\mu\mu$  pairs. Because the detector acceptance and reconstruction efficiency for electrons and muons

**Table 6.7:** Selection cuts used as a starting point for the simultaneous fit.

Cut (GeV)	$t\bar{t}$	$Z + \text{jets}$	$W + \text{jets}$	Diboson
Preselection	$3318 \pm 16$	$(294.8 \pm 2.0) \cdot 10^2$	$13 \pm 3$	$188 \pm 5$
$ m_{\mu\mu} - m_Z  < 10$	$506 \pm 6$	$(258.4 \pm 1.9) \cdot 10^2$	$4.0 \pm 1.6$	$158 \pm 5$
4 jets, $p_T > 40$	$53.9 \pm 2.1$	$727 \pm 22$	$0.7 \pm 0.7$	$3.7 \pm 0.7$

**Table 6.8:** Composition of the control sample.

Cut (GeV)	$t\bar{t}$	$Z + \text{jets}$	$W + \text{jets}$	Diboson
Preselection	$5850 \pm 21$	$12 \pm 3$	$68 \pm 7$	$9.1 \pm 1.1$
4 jets, $p_T > 40$	$670 \pm 7$	$(20 \pm 9) \cdot 10^{-2}$	$2.7 \pm 1.4$	$0.4 \pm 0.3$

is quite different, it is difficult to use the absolute number. It is, however, possible to use the  $e\mu$  channel to determine the distribution shape of variables in the  $\mu\mu$  channel.

The Standard Model background in the dimuon channel is dominated by  $t\bar{t}$  and  $Z + \text{jets}$  events. An optimal separation between  $t\bar{t}$ ,  $Z + \text{jets}$  and SUSY can be seen in the  $\cancel{E}_T$  distribution, hence this is the distribution that will be fitted. To limit the dependence on a particular choice of a point in SUSY parameter space, a loose set of cuts will be used as the starting point for the fit. The cut flow for these cuts is summarized in table 6.7.

The selection cuts used on the control sample are less strict than on the signal sample to increase the amount of statistics. This results in a better fit, provided that the shape of the distribution is not altered by the different selection cuts. Figure 6.12 shows a comparison of the  $\cancel{E}_T$  shape of the  $t\bar{t}$  events in the signal and control samples. Both distributions have been normalized to unity for comparison. The selection cuts used for the control sample are summarized in table 6.8. After the selection cuts, the sample is dominated by  $t\bar{t}$ , as required for the control sample.

### 6.8.3 Fitting procedure

Figure 6.13 shows the  $\cancel{E}_T$  distribution for the dominant backgrounds, after the cuts of table 6.7 have been applied. The distributions of  $Z + \text{jets}$  and  $t\bar{t}$  show a very similar

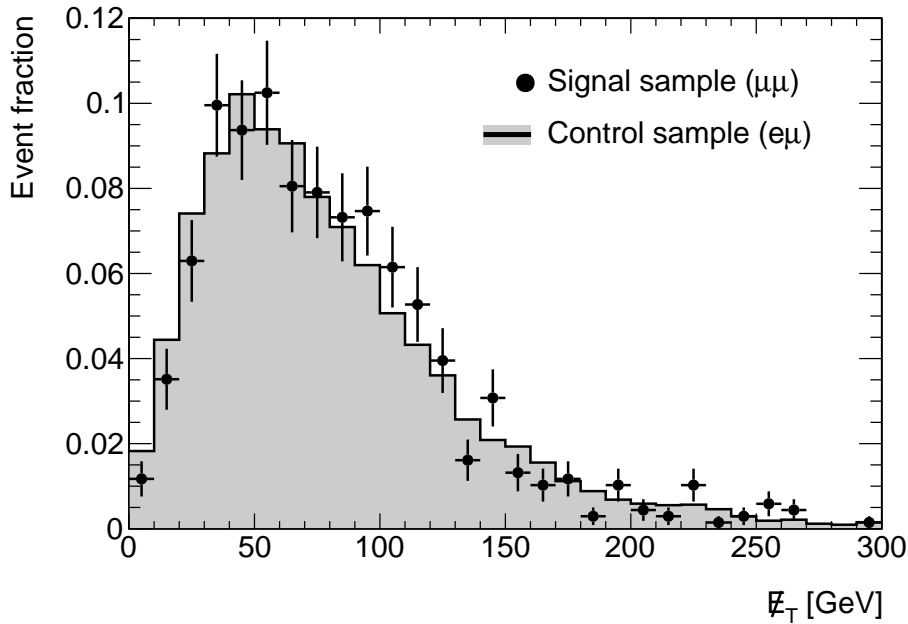


**Figure 6.12:** Shape of the  $E_T$  distribution of  $t\bar{t}$  events in the signal and control sample. Both distributions are normalized to unity. Due to looser cuts, the amount of statistics in the control sample is much higher.

behavior. The number of events decreases exponentially with  $E_T$ , while on the lower end of the spectrum there is a cutoff because of the event selection. Furthermore, the  $Z + \text{jets}$  is mostly concentrated in the region where  $E_T < 80 \text{ GeV}$ , while  $t\bar{t}$  (and possibly SUSY) extend to much higher values. This makes it possible to separate the  $Z + \text{jets}$  background from  $t\bar{t}$  in the fit.

To describe the backgrounds, the probability distribution:

$$P(x; \alpha, \mu, \sigma) = \left( \operatorname{erf} \left( \frac{x - \mu}{\sigma} \right) + 1 \right) \exp \left( -\frac{x}{\alpha} \right), \quad (6.7)$$

is used as an Ansatz, with  $\operatorname{erf}(x)$  the Gauss error function, defined as:

$$\operatorname{erf}(x) = \frac{2}{\sqrt{\pi}} \int_0^x e^{-t^2} dt. \quad (6.8)$$

For values of  $x$  where  $x - \mu \gg \sigma$  the Gauss error function approaches unity, leading to a simple exponential decay distribution with decay constant  $\alpha$ . For low values of  $x$ , the error function provides a turn-on curve centered at  $\mu$  with a width of  $\sigma$ . The probability density function of equation 6.7 is in good agreement with the Monte Carlo  $E_T$  spectrum of the  $Z + \text{jets}$  and  $t\bar{t}$  samples. A combined fit on these two samples results in a  $\chi^2/N_{\text{DoF}} = 2.5$  and yields the correct  $Z + \text{jets}$  to  $t\bar{t}$  ratio.

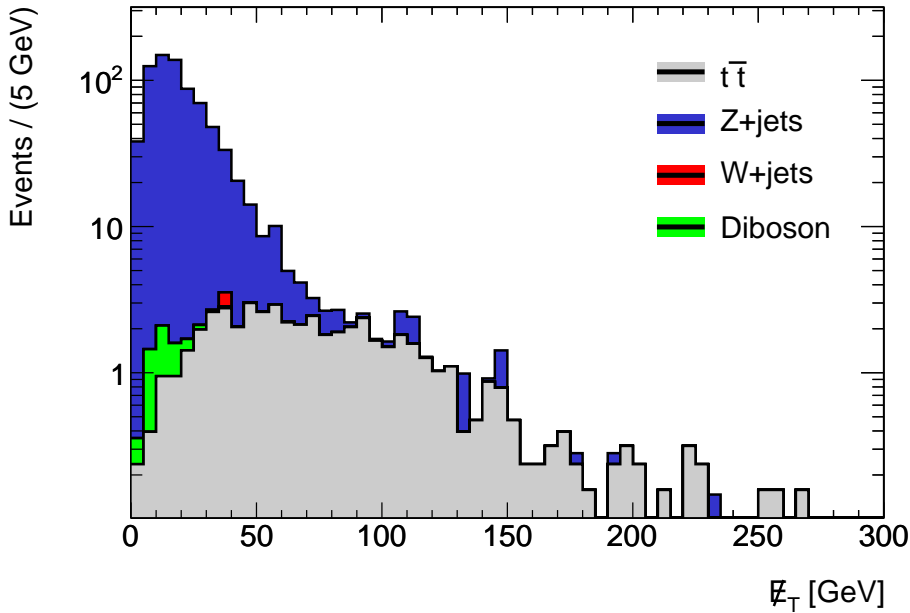


**Figure 6.13:**  $\mathcal{E}_T$  distribution of the various Standard Model backgrounds after the cuts of table 6.7 have been applied. The  $Z + \text{jets}$  contribution dominates at low values, while at high values of  $\mathcal{E}_T$  the background is almost entirely composed of dileptonic  $t\bar{t}$ .

For the simultaneous fit, two instances of the distribution of equation 6.7 are summed. The first will fit the  $Z + \text{jets}$  contribution in the signal sample, while the second will fit the  $t\bar{t}$  contribution in both the signal and control samples simultaneously. The simultaneous fit of  $t\bar{t}$  in the signal and control samples makes it possible to fit the number of events in the presence of other backgrounds.

To limit the effect of possible SUSY contaminations on the fit, sideband regions are defined in both the signal and control samples. In the signal sample, only the region  $\mathcal{E}_T < 110 \text{ GeV}$  is used for the fit. In the control sample, this sideband region extends up to  $\mathcal{E}_T < 200 \text{ GeV}$ . In both sideband regions, the amount of events is dominated by  $t\bar{t}$  and  $Z + \text{jets}$ , the effect of possible signal events is small.

The results of the simultaneous fit, in the case of a signal that consists of SUSY point 1, is shown in figure 6.14 for the control sample and figure 6.15 for the signal sample.

In order to quantize the significance of the event excess that can be seen in figure 6.15, the fit parameters are used to estimate the number of background events in the region of  $\mathcal{E}_T > 180 \text{ GeV}$ , which will be referred to as the signal region. The measured number of signal events is then defined as the measured number of events in this region, minus

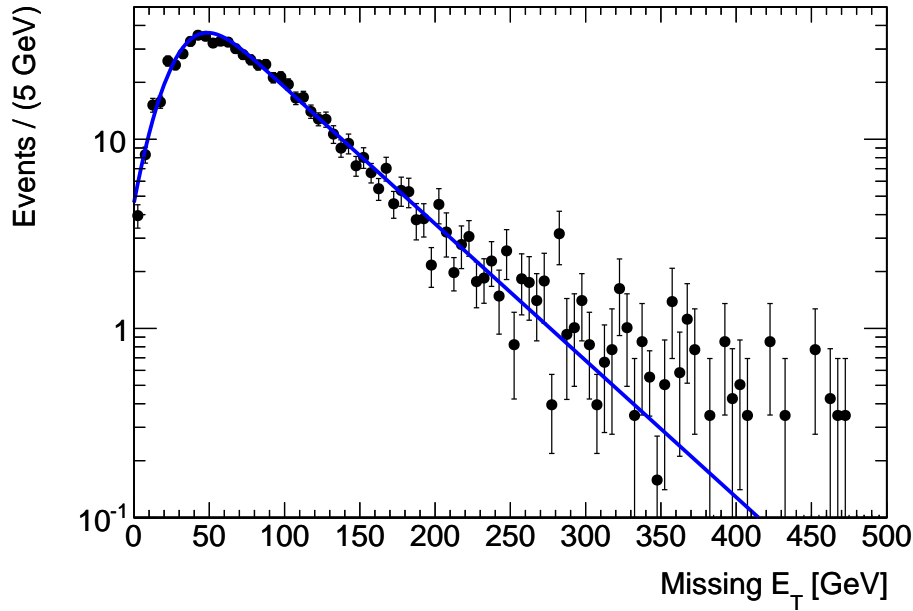


**Figure 6.14:** The control sample for SUSY point 1, fitted with the distribution of equation 6.7.

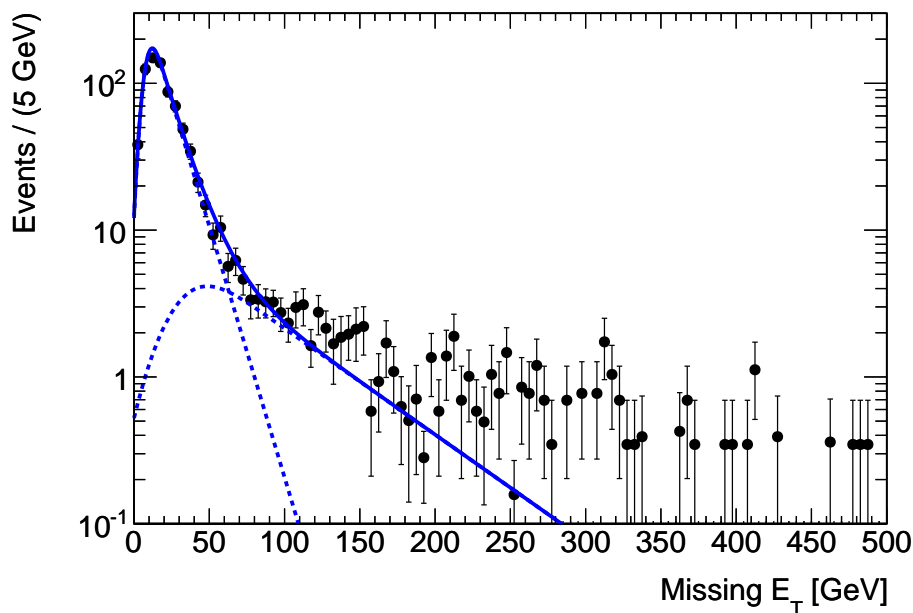


**Figure 6.15:** The fit in the signal sample for SUSY point 1. The  $t\bar{t}$  curve is fitted simultaneously in the signal and control samples. A second instance of the distribution of equation 6.7 is then fitted to the peak of  $Z + \text{jets}$ .

the background estimate.

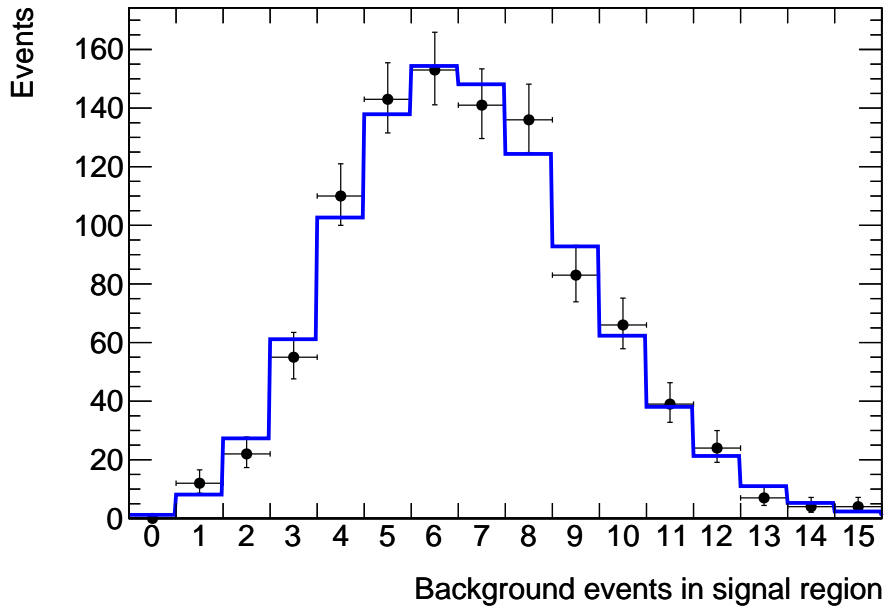


**Figure 6.16:** The observed number of background events in the region  $E_T > 180 \text{ GeV}$  for 10,000 toy Monte Carlo experiments, drawn from the fitted distribution in figure 6.15. The fit shown is a Poisson distribution with expectation value  $\mu = 6.8$ .

To obtain the uncertainty on the background estimate, a toy Monte Carlo experiment is performed. Using the fitted distribution shown in figure 6.15, 10,000 samples are drawn that each contain the same number of events as the original dataset. For each of these toy MC samples, the number of events in the signal region is then counted, resulting in 10,000 background estimates. The distribution of these estimates is shown in figure 6.16. This figure shows that the estimate follows a Poisson distribution with expectation value  $\mu = 6.8$ . Using the standard deviation of the obtained Poisson distribution as the uncertainty on the background estimate, the significance of the chosen mSUGRA points can be calculated.

#### 6.8.4 Systematic uncertainties

The simultaneous fit method does not directly rely on Monte Carlo for its prediction. Because of its data driven background estimate, the sensitivity to the aforementioned sources of systematic uncertainty is much smaller. The effects of the variations in the  $t\bar{t}$  cross section, jet energy scale and missing energy scale on the results of the fit are

**Table 6.9:** Effect of various sources of systematic uncertainty on the background event estimate.

	Estimated background	True background
Initial	$3.3 \pm 1.8$	3.0
$t\bar{t}$ cross section $-19.5\%$	$2.6 \pm 1.6$	2.5
$t\bar{t}$ cross section $+28.3\%$	$4.2 \pm 2.0$	3.8
Jet energy scale $-5\%$	$2.8 \pm 1.7$	2.9
Jet energy scale $+5\%$	$3.8 \pm 2.0$	3.4
Missing energy scale $-8\%$	$2.6 \pm 1.6$	2.5
Missing energy scale $+8\%$	$3.8 \pm 1.9$	3.7

summarized in table 6.9. The background event estimate follows the true number of events. The event count estimates obtained from the fit are in good agreement with the true values.

It should be noted, however, that in the presence of SUSY signal, this method suffers from overestimation of the background level. A fraction of the signal events will be wrongly attributed to the background, leading to a systematic underestimation of the signal significance.

It is possible to incorporate the presence of signal into the fit. From figure 6.6 it can be seen that the signal events approximately follow a uniform distribution up to  $\cancel{E}_T = 350$  GeV. If this uniform distribution is included in the fit, the overestimation can be avoided.

Nevertheless, this assumption limits the applicability of the search method. Until now, only the  $\cancel{E}_T$  distributions of known Standard Model processes have been used in the fit. Large missing transverse energy is a direct result of R-parity conservation in supersymmetric models. Searching for an excess of events after subtracting the known Standard Model processes would be a generally valid approach. Including a supersymmetry contribution in the simultaneous fit would limit the validity of this method to regions in parameter space that have similar signatures to the points that have been studied here. The extent of these regions would need further study, but it is likely to be much smaller than the region where the original method is valid. Therefore it was chosen to keep this analysis as general as possible by fitting only the known Standard Model backgrounds.

**Table 6.10:** Obtained significance when using the simultaneous fit method. The significance is calculated as  $s/\sigma_b$ , with  $s$  the number of signal events and  $\sigma_b$  the statistical uncertainty on the number of background events, as determined from the toy Monte Carlo. The true number of background events in this case was 3.0.

Sample	Signal events	True signal events	Background events	Significance
Point 1	$23 \pm 5$	27	$6 \pm 3$	9.0
Point 2	$13 \pm 4$	15	$5.0 \pm 2.2$	5.8
Point 3	$5.6 \pm 2.4$	6.7	$3.9 \pm 2.0$	2.4

### 6.8.5 Obtained significance

When applying the simultaneous fit method to the three selected signal samples, the signal significance that can be obtained is listed in table 6.10. When comparing these results to the results of the counting method in table 6.6, it can be seen that removing the systematic uncertainty on the background level has indeed led to a higher signal significance for most points.

However, for the third signal point, the significance has decreased. This is caused by the overestimation of the background level in the presence of signal events, as mentioned in the previous section. The overestimation is proportional to the number of signal events, while the systematic error on the Monte Carlo background level is proportional to the number of background events. Because of the low signal and background levels, the effect of the latter turns out to be less important than the overestimation.

## 6.9 Dependence on $\tan\beta$

The influence of the parameter  $\tan\beta$ , the ratio of the vacuum expectation values of the two Higgs doublets, is evaluated by repeating the simultaneous fit on a second set of signal points. In this second set, the value of  $\tan\beta$  has been increased to 50, while the remaining mSUGRA parameters have been kept constant. The parameters and cross sections of these new points, denoted 1b–3b, are summarized in table 6.11.

The effect of the change in  $\tan\beta$  on the branching ratio of  $\tilde{\chi}_2^0 \rightarrow Z^0 \tilde{\chi}_1^0$  is illustrated in figure 6.17. It shows that, while the region with high branching ratio has shifted, the behavior is essentially the same. The three chosen signal points all remain inside the region where  $\text{BR}(\tilde{\chi}_2^0 \rightarrow Z^0 \tilde{\chi}_1^0) > 0.95$ .

**Table 6.11:** mSUGRA points from the signal grid where  $\text{BR}(\tilde{\chi}_2^0 \rightarrow Z^0 \tilde{\chi}_1^0) > 0.95$  for  $\tan \beta = 50$ .

Point	$m_0$ (GeV)	$m_{1/2}$ (GeV)	$A_0$ (GeV)	$\tan \beta$	sign $\mu$	$\sigma$ (pb)
1b	350	275	0	50	+	5.48
2b	390	310	0	50	+	2.83
3b	970	292	0	50	+	1.38

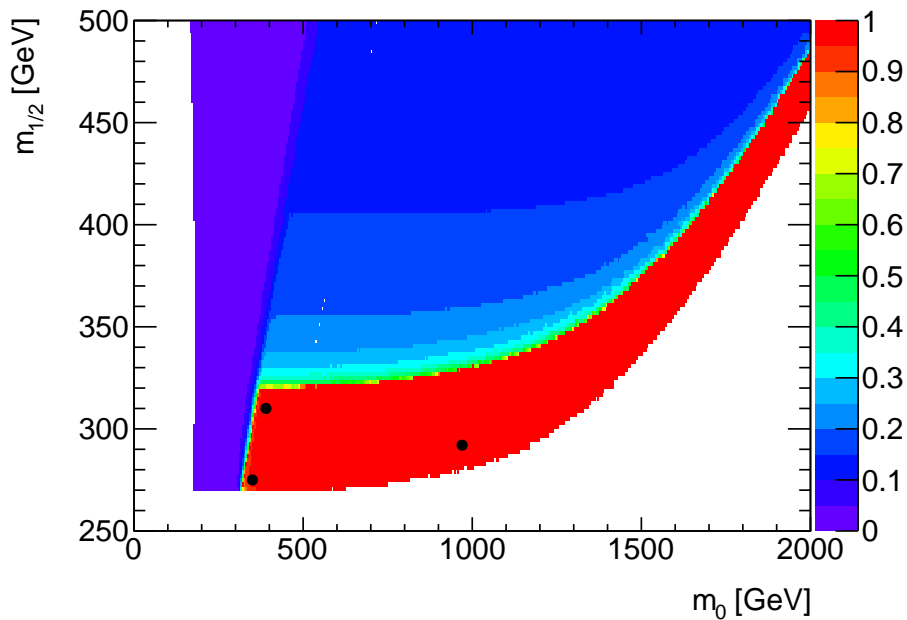


**Figure 6.17:** Branching ratio of the process  $\tilde{\chi}_2^0 \rightarrow Z^0 \tilde{\chi}_1^0$  as a function of the mSUGRA parameters  $m_0$  and  $m_{1/2}$ . The remaining parameters are fixed at  $\tan \beta = 50$ ,  $A_0 = 0$  GeV and  $\text{sign } \mu > 0$ .

**Table 6.12:** Obtained significance when using the simultaneous fit method on the  $\tan \beta = 50$  signal samples.

Sample	Signal events	True signal events	Background events	Significance
Point 1b	$24 \pm 5$	27	$6 \pm 3$	9.6
Point 2b	$12 \pm 3$	14	$4.7 \pm 2.2$	5.5
Point 3b	$5.6 \pm 2.4$	7.2	$4.6 \pm 2.2$	2.6

The results of performing the simultaneous fit method on these three points is summarized in table 6.12. The effect of the change in  $\tan \beta$  on the results of the simultaneous fit is negligible. Within the region of  $\text{BR}(\tilde{\chi}_2^0 \rightarrow Z^0 \tilde{\chi}_1^0) > 0.95$ , the largest effect of  $\tan \beta$  on this analysis is via the change in signal cross section. However, for points near the edge of the region, a change in  $\tan \beta$  can lead to a mass spectrum where the  $\tilde{\chi}_2^0 \rightarrow Z^0 \tilde{\chi}_1^0$  channel is no longer kinematically allowed.

## 6.10 Conclusions

The analysis presented in this chapter investigates the possibility of a discovery of supersymmetry using the  $\tilde{\chi}_2^0 \rightarrow Z^0 \tilde{\chi}_1^0 \rightarrow \mu^+ \mu^- \tilde{\chi}_1^0$  channel. Assuming an available integrated luminosity of  $2 \text{ fb}^{-1}$  at a center of mass energy of  $10 \text{ TeV}$ , two methods are discussed to detect the  $Z^0$  and missing transverse energy signature in the presence of the Standard Model backgrounds.

The first method is a basic event counting method. It shows that by imposing a strict set of cuts an excess of events above the Standard Model expectations can already be observed. However, this method depends on Monte Carlo simulation for an estimate of the number of Standard Model events that pass the event selection. This introduces considerable systematic uncertainties into the analysis, resulting in a degradation of the discovery potential. The mSUGRA signal point with  $m_0 = 350 \text{ GeV}$ ,  $m_{1/2} = 275 \text{ GeV}$ ,  $A_0 = 0 \text{ GeV}$ ,  $\text{sign } \mu > 0$  and  $\tan \beta = 10$  can be observed with a significance of 5.9.

To reduce the influence of the uncertainty on the Monte Carlo estimates, the simultaneous fit method is introduced. This method defined a control sample, with an opposite sign muon-electron pair instead of a muon-muon pair in the final state. This control sample can be used to estimate the level of the main irreducible background, dileptonic  $t\bar{t}$ , from data instead of simulation. The simultaneous fit method fits the  $\cancel{E}_T$

spectrum in the signal and control samples simultaneously. By requiring the dileptonic  $t\bar{t}$  contribution in both samples to have the same shape, the number of Standard Model events in the signal region can be estimated. The search for supersymmetry will then concentrate in finding a significant excess of events above the Standard Model estimate. This method will enhance the visible signal for the aforementioned point in parameter space and leads to a signal significance of 9.0.

Based on the results presented in this chapter, the channel  $\tilde{\chi}_2^0 \rightarrow Z^0 \tilde{\chi}_1^0 \rightarrow \mu^+ \mu^- \tilde{\chi}_1^0$  appears to be a promising channel for early SUSY searches. The signature it provides is reasonably clean and well visible above the background. Furthermore, the strong dependence on the position in the  $m_0$ - $m_{1/2}$  plane means that this channel can provide important information on the value of these parameters.

# References

- [1] M. Kobayashi and T. Maskawa, *CP-Violation in the Renormalizable Theory of Weak Interaction*, Progress of Theoretical Physics, **49**(2), (1973), 652–657.
- [2] S. L. Glashow, *Partial Symmetries of Weak Interactions*, Nucl. Phys., **22**, (1961), 579–588.
- [3] S. Weinberg, *A Model of Leptons*, Phys. Rev. Lett., **19**, (1967), 1264–1266.
- [4] The UA1 Collaboration, G. Arnison et al., *Experimental Observation of Isolated Large Transverse Energy Electrons with Associated Missing Energy at  $\sqrt{s} = 540$  GeV*, Phys. Lett., **B122**(1), (1983), 103–116.
- [5] The UA1 Collaboration, G. Arnison et al., *Experimental Observation of Lepton Pairs of Invariant Mass Around 95 GeV/c<sup>2</sup> at the CERN SPS Collider*, Phys. Lett., **B126**(5), (1983), 398–410.
- [6] The UA2 Collaboration, P. Bagnaia et al., *Evidence for  $Z^0 \rightarrow e^+e^-$  at the CERN  $\bar{p}p$  Collider*, Phys. Lett., **B129**(1-2), (1983), 130–140.
- [7] The DØ Collaboration, S. Abachi et al., *Search for High Mass Top Quark Production in  $p\bar{p}$  Collisions at  $\sqrt{s} = 1.8$  TeV*, Phys. Rev. Lett., **74**(13), (1995), 2422–2426.
- [8] The CDF Collaboration, F. Abe et al., *Observation of Top Quark Production in  $p\bar{p}$  Collisions with the Collider Detector at Fermilab*, Phys. Rev. Lett., **74**(14), (1995), 2626–2631.
- [9] The DONUT Collaboration, K. Kodama et al., *Observation of Tau Neutrino Interactions*, Phys. Lett., **B504**(3), (2001), 218–224.
- [10] The ALEPH, DELPHI, L3 and OPAL Collaboration, *Search for the Standard Model Higgs Boson at LEP*, Phys. Lett., **B565**, (2003), 61–75.

- [11] The CDF and DØ Collaboration, *Combined CDF and DØ Upper Limits on Standard Model Higgs-Boson Production with up to 6.7 fb<sup>-1</sup> of Data*, in *35th International Conference on High Energy Physics (ICHEP)* (2010).
- [12] The ALEPH, CDF, DØ, DELPHI, L3, OPAL and SLD Collaboration, *Precision Electroweak Measurements and Constraints on the Standard Model*, 0911.2604v2, <http://arxiv.org/abs/0911.2604v2>.
- [13] M. E. Peskin and D. V. Schroeder, *An Introduction to Quantum Field Theory*, Perseus Books (2008).
- [14] D. J. Griffiths, *Introduction to Elementary Particles*, Wiley (1987).
- [15] P. W. Higgs, *Broken Symmetries, Massless Particles and Gauge Fields*, Phys. Lett., **12**(2), (1964), 132–133.
- [16] P. W. Higgs, *Broken Symmetries and the Masses of Gauge Bosons*, Phys. Rev. Lett., **13**, (1964), 508–509.
- [17] P. W. Higgs, *Spontaneous Symmetry Breakdown without Massless Bosons*, Phys. Rev., **145**(4), (1966), 1156–1163.
- [18] F. Englert and R. Brout, *Broken Symmetry and the Mass of Gauge Vector Mesons*, Phys. Rev. Lett., **13**(9), (1964), 321–323.
- [19] G. S. Guralnik, C. R. Hagen and T. W. B. Kibble, *Global Conservation Laws and Massless Particles*, Phys. Rev. Lett., **13**(20), (1964), 585–587.
- [20] The Super-Kamiokande Collaboration, Y. Fukuda et al., *Evidence for Oscillation of Atmospheric Neutrinos*, Phys. Rev. Lett., **81**(8), (1998), 1562–1567.
- [21] The WMAP Collaboration, E. Komatsu et al., *Five-Year Wilkinson Microwave Anisotropy Probe (WMAP) Observations: Cosmological Interpretation*, The Astrophysical Journal Supplement Series, **180**(2), (2009), 330.
- [22] H. P. Nilles, *Supersymmetry, Supergravity and Particle Physics*, Phys. Rep., **110**(1-2), (1984), 1–162.
- [23] H. E. Haber and G. L. Kane, *The Search for Supersymmetry – Probing Physics Beyond the Standard Model*, Phys. Rep., **117**(2-4), (1985), 75–263.
- [24] S. P. Martin, *A Supersymmetry Primer*, hep-ph/9709356v5, <http://arxiv.org/abs/hep-ph/9709356v5>.

- [25] I. J. R. Aitchison, *Supersymmetry and the MSSM: An Elementary Introduction*, hep-ph/0505105v1, <http://arxiv.org/abs/hep-ph/0505105v1>.
- [26] The SNO Collaboration, S. N. Ahmed et al., *Constraints on Nucleon Decay via Invisible Modes from the Sudbury Neutrino Observatory*, Phys. Rev. Lett., **92**(10), (2004), 102004.
- [27] S. P. Martin and M. T. Vaughn, *Two-Loop Renormalization Group Equations for Soft Supersymmetry-Breaking Couplings*, Phys. Rev. D, **50**(3), (1994), 2282–2292.
- [28] H. Baer et al., *ISAJET 7.69: A Monte Carlo Event Generator for  $pp$ ,  $\bar{p}p$ , and  $e^+e^-$  Reactions*, hep-ph/0312045v1, <http://arxiv.org/abs/hep-ph/0312045v1>.
- [29] W. Porod, *SPheno, A Program for Calculating Supersymmetric Spectra, SUSY Particle Decays and SUSY Particle Production at  $e^+e^-$  Colliders*, Computer Physics Communications, **153**, (2003), 275–315.
- [30] A. Djouadi, J. L. Kneur and G. Moultaka, *SuSpect: A Fortran Code for the Supersymmetric and Higgs Particle Spectrum in the MSSM*, Computer Physics Communications, **176**, (2007), 426–455.
- [31] B. Allanach, *SOFTSUSY: A Program for Calculating Supersymmetric Spectra*, Computer Physics Communications, **143**, (2002), 305–331.
- [32] The WMAP Collaboration, E. Komatsu et al., *Seven-Year Wilkinson Microwave Anisotropy Probe (WMAP) Observations: Cosmological Interpretation*, 1001.4538v2, <http://arxiv.org/abs/1001.4538v2>.
- [33] G. Bélanger et al., *WMAP Constraints on SUGRA Models with Non-Universal Gaugino Masses and Prospects for Direct Detection*, Nucl. Phys., **B706**(1-2), (2005), 411–454.
- [34] G. Bélanger, *Dark matter and the LHC*, Nucl. Phys. B. Proc. Suppl., **B194**, (2009), 5–10.
- [35] G. Caceres and D. Hooper, *Neutralino Dark Matter as the Source of the WMAP Haze*, Phys. Rev. D, **78**(12), (2008), 123512.
- [36] I. Niessen, *Supersymmetric Phenomenology in the mSUGRA Parameter Space*, Master's thesis, Radboud University, Nijmegen (2008).

- [37] J. Ellis, K. Olive and Y. Santoso, *Calculations of Neutralino-Stop Coannihilation in the CMSSM*, Astroparticle Physics, **18**(4), (2003), 395–432.
- [38] A. Djouadi, *The Anatomy of Electro-Weak Symmetry Breaking II: The Higgs Bosons in the Minimal Supersymmetric Model*, Phys. Rept., **459**, (2008), 1–241.
- [39] B. C. Allanach et al., *Precise Determination of the Neutral Higgs Boson Masses in the MSSM*, Journal of High Energy Physics, **2004**(09), (2004), 044.
- [40] L. R. Evans and P. Bryant, *LHC Machine*, Journal of Instrumentation, **3**, (2008), S08001.
- [41] The ATLAS Collaboration, G. Aad et al., *The ATLAS Experiment at the CERN Large Hadron Collider*, Journal of Instrumentation, **3**, (2008), S08003.
- [42] The CMS Collaboration, S. Chatrchyan et al., *The CMS Experiment at the CERN LHC*, Journal of Instrumentation, **3**, (2008), S08004.
- [43] The LHCb Collaboration, A. Augusto Alves Jr. et al., *The LHCb Detector at the LHC*, Journal of Instrumentation, **3**, (2008), S08005.
- [44] The ALICE Collaboration, K. Aamodt et al., *The ALICE experiment at the CERN LHC*, Journal of Instrumentation, **3**, (2008), S08002.
- [45] The TOTEM Collaboration, G. Anelli et al., *The TOTEM Experiment at the CERN Large Hadron Collider*, Journal of Instrumentation, **3**, (2008), S08007.
- [46] The LHCf Collaboration, O. Adriani et al., *The LHCf Detector at the CERN Large Hadron Collider*, Journal of Instrumentation, **3**, (2008), S08006.
- [47] The ATLAS Collaboration, G. Aad et al., *Expected Performance of the ATLAS Experiment: Detector, Trigger and Physics*, chapter Dilepton Resonances at High Mass, pp. 1696–1725, CERN-OPEN-2008-020, CERN, Geneva (2008).
- [48] E. E. van der Kraaij, *First Top Quark Physics with ATLAS – A Prospect*, Ph.D. thesis, University of Amsterdam (2009).
- [49] C. A. Magrath, *The Heart of ATLAS – Commissioning and Performance of the ATLAS Silicon Tracker*, Ph.D. thesis, Radboud University (2009).
- [50] The ATLAS Collaboration, *ATLAS Liquid-Argon Calorimeter: Technical Design Report*, Technical Report ATLAS-TDR-002, CERN, Geneva (1996).

- 
- [51] The ATLAS Collaboration, *ATLAS Tile Calorimeter: Technical Design Report*, Technical Report ATLAS-TDR-003, CERN, Geneva (1996).
  - [52] The ATLAS Collaboration, *Athena Developers Guide*.
  - [53] G. Barrand et al., *GAUDI – A Software Architecture and Framework for Building HEP Data Processing Applications*, Computer Physics Communications, **140**(1-2), (2001), 45–55.
  - [54] *Python Programming Language*, <http://www.python.org/>.
  - [55] P. Calafiura et al., *The StoreGate: a Data Model for the Atlas Software Architecture*, ATLAS Internal Note ATL-SOFT-2003-009, CERN, Geneva (2003).
  - [56] M. Dobbs et al., *Les Houches Guidebook to Monte Carlo Generators for Hadron Collider Physics*, hep-ph/0403045v2, <http://arxiv.org/abs/hep-ph/0403045v2>.
  - [57] M. Mangano et al., *ALPGEN, a Generator for Hard Multiparton Processes in Hadronic Collisions*, Journal of High Energy Physics, **2003**(07), (2003), 001.
  - [58] T. Sjöstrand et al., *High-Energy-Physics Event Generation with PYTHIA 6.1*, Computer Physics Communications, **135**(2), (2001), 238–259.
  - [59] G. Corcella et al., *HERWIG 6: An Event Generator for Hadron Emission Reactions with Interfering Gluons (Including Supersymmetric Processes)*, Journal of High Energy Physics, **2001**(01), (2001), 010.
  - [60] S. Frixione, P. Nason and B. Webber, *Matching NLO QCD and Parton Showers in Heavy Flavour Production*, Journal of High Energy Physics, **2003**(08), (2003), 007.
  - [61] S. Agostinelli et al., *GEANT4: A Simulation Toolkit*, Nuclear Instruments & Methods In Physics Research, **A506**(3), (2003), 250–303.
  - [62] D. Adams et al., *The ATLFAST-II Performance in Release 14 –Particle Signatures and Selected Benchmark Processes–*, ATLAS Note ATL-COM-PHYS-2009-554, CERN, Geneva (2009).
  - [63] M. Dührssen, *The Fast Calorimeter Simulation FastCaloSim*, ATLAS Note ATL-COM-PHYS-2008-093, CERN, Geneva (2008).
  - [64] Z. van Kesteren, *Identification of Muons in ATLAS*, Ph.D. thesis, University of Amsterdam (2010).

- [65] G. Ordóñez Sans, *Muon Identification in the ATLAS Calorimeters*, Ph.D. thesis, Radboud University, Nijmegen, The Netherlands (2009).
- [66] J. Snuverink, *The ATLAS Muon Spectrometer: Commissioning and Tracking*, Ph.D. thesis, University of Twente (2009).
- [67] The ATLAS Collaboration, G. Aad et al., *Expected Performance of the ATLAS Experiment: Detector, Trigger and Physics*, chapter Jet Reconstruction Performance, pp. 262–297, CERN-OPEN-2008-020, CERN, Geneva (2008).
- [68] M. Cacciari, G. P. Salam and G. Soyez, *The anti- $k_T$  jet clustering algorithm*, Journal of High Energy Physics, **2008**(04), (2008), 063.
- [69] The ATLAS Collaboration, G. Aad et al., *Expected Performance of the ATLAS Experiment: Detector, Trigger and Physics*, chapter Measurement of Missing Transverse Energy, pp. 368–396, CERN-OPEN-2008-020, CERN, Geneva (2008).
- [70] The ATLAS Collaboration, G. Aad et al., *Performance of the ATLAS Detector using First Collision Data*, Journal of High Energy Physics, **2010**(09), (2010), 056.
- [71] *Atlas Modular Analysis Framework (AMA)*, <https://twiki.cern.ch/twiki/bin/view/AtlasProtected/AMAMainPage>.
- [72] R. Brun and F. Rademakers, *ROOT – An Object Oriented Data Analysis Framework*, Nuclear Instruments & Methods In Physics Research, **A389**(1-2), (1997), 81–86.
- [73] W. Verkerke and D. Kirkby, *The RooFit Toolkit for Data Modeling*, `physics/0306116`, <http://arxiv.org/abs/physics/0306116>.
- [74] *Atlantis, Event Display for ATLAS*, <http://cern.ch/atlantis/>.
- [75] J. Drohan et al., *The Atlantis Event Visualisation Program for the ATLAS Experiment*, in *Computing in High Energy Physics and Nuclear Physics 2004*, p. 361 (2005).
- [76] H. Drevermann, D. Kuhn and B. S. Nilsson, *Event Display: Can We See What We Want to See?*, in *18th CERN School of Computing*, CERN-ECP-95-025, pp. 17–64 (1995).
- [77] G. Lutz, *Topological Vertex Search in Collider Experiments*, Nuclear Instruments & Methods In Physics Research, **A337**(1), (1993), 66–94.

- [78] N. Konstantinidis and H. Drevermann, *Fast Tracking in Hadron Collider Experiments*, in *Advanced Computing and Analysis Techniques in Physics Research: VII International Workshop; ACAT 2000*, volume 583, pp. 130–132, AIP (2001).
- [79] Z. Maxa et al., *Event Visualisation for the ATLAS Experiment - The Technologies Involved*, in *15th International Conference on Computing In High Energy and Nuclear Physics*, pp. 167–169 (2006).
- [80] World Wide Web Consortium, *Extensible Markup Language*, <http://www.w3.org/TR/xml/>.
- [81] F. Hubaut and P. Pralavorio, *Early SUSY Search in Final States with Z Bosons*, ATLAS Internal Note ATL-PHYS-INT-2008-014 (2008).
- [82] The CMS Collaboration, D. Acosta et al., *CMS Technical Design Report, Volume II: Physics Performance*, Journal of Physics G, **34**, (2007), 995–1579.
- [83] S. Kyriazopoulou and C. Markou, *Search for SUSY in Final States with Z Bosons*, CMS Note 2006/116 (2006).
- [84] K. Theofilatos et al., *SUSY Searches in the  $Z^0 + \geq 3 \text{ jets} + E_T$  Final State with Data-Driven Backgorund Estimation*, CMS Analysis Note AN-2009/132 (2009).
- [85] B. Allanach, S. Kraml and W. Porod, *Comparison of SUSY Mass Spectrum Calculations*, hep-ph/0207314v1, <http://arxiv.org/abs/hep-ph/0207314v1>.
- [86] The ATLAS Collaboration, G. Aad et al., *Expected Performance of the ATLAS Experiment: Detector, Trigger and Physics*, chapter Supersymmetry Searches, pp. 1514–1524, CERN-OPEN-2008-020, CERN, Geneva (2008).
- [87] *SUSY Signal Grid Production*, <https://twiki.cern.ch/twiki/bin/view/AtlasProtected/SUSYSignalProduction>.
- [88] The ATLAS Collaboration, G. Aad et al., *Expected Performance of the ATLAS Experiment: Detector, Trigger and Physics*, chapter Performance of the Muon Trigger Slice with Simulated Data, pp. 647–682, CERN-OPEN-2008-020, CERN, Geneva (2008).
- [89] The ATLAS Collaboration, *Prospects for Measuring Top Pair Prduction in the Dilepton Channel with Early ATLAS Data at  $\sqrt{10}$  TeV*, Atlas Note ATL-PHYS-PUB-2009-086, CERN (2009).

- [90] The ATLAS Collaboration, G. Aad et al., *Expected Performance of the ATLAS Experiment: Detector, Trigger and Physics*, chapter Jet Energy Scale: In-situ Calibration Strategies, pp. 335–367, CERN-OPEN-2008-020, CERN, Geneva (2008).
- [91] The ATLAS Collaboration, G. Aad et al., *Expected Performance of the ATLAS Experiment: Detector, Trigger and Physics*, CERN-OPEN-2008-020, CERN, Geneva (2008).

# Summary

The elementary particles and the fundamental forces between them are described by the Standard Model of particle physics. This has been a very successful theory, providing very accurate predictions that have almost all been confirmed experimentally. It is because of this that the Higgs boson predicted by the Standard Model has led to one of the biggest particle searches ever conducted. Several generations of particle collision experiments have set limits on its mass, but so far it has not been observed.

The Large Hadron Collider (LHC) at the CERN laboratory near Geneva, Switzerland is the world's largest and most energetic particle accelerator. Located in an underground tunnel that measures 26.7 km in circumference, it is designed to collide proton beams at a center of mass energy of 14 TeV. At the points where these collisions occur, large particle detectors measure the trajectories and properties of the particles that escape from the collision. By carefully studying these particles, physicists can derive information about the processes that happened in the initial collision.

While the Higgs boson has been a major motivation for the construction of the LHC, it is by no means the only motivation. Over the years, experimental observations have been made that suggest that the Standard Model as we know it is not yet complete. For example, cosmological measurements have shown that only 4.4 % of the Universe consists of the “ordinary” matter that is described by the Standard Model. Another 21.4 % is made up of unknown matter that interacts only gravitationally (dark matter), and the remainder is an even more mysterious form of energy (dark energy). Together with theoretical arguments about certain aspects of the Standard Model being mathematically inelegant, this has inspired many new theories for physics beyond the Standard Model.

One of the possible new theories is supersymmetry. This theory predicts that for every known particle there is a supersymmetric partner particle. These extra particles can resolve some of the mathematical issues in the Standard Model, but if one of the supersymmetric particles is stable, it could also offer an explanation for the existence of dark matter.

The ATLAS detector is one of the two general purpose detectors at the LHC. It

was designed to be able to measure a very broad spectrum of physics processes. The detector, measuring 40 m in length and 20 m in diameter, is constructed in layers around the interaction point. Each of these layers, or subdetectors, measures different properties of the outgoing particles, allowing them to be reconstructed and identified.

An important instrument for debugging both detector hardware and reconstruction software is visual investigation of collision events. Part of this thesis discusses the Atlantis event display and the techniques it uses. The total number of readout channels in the ATLAS detector is close to 100 million, which makes the visual representation of events quite challenging.

Atlantis approaches this issue by using so-called data-oriented projections. Rather than using a three dimensional view of the detector, it uses a series of two dimensional projections. These projections are based on the coordinates that are measured in the different subdetectors. Most of the subdetectors measure only two coordinates, therefore projecting along the third coordinate provides the best possible view of that particular subdetector. The higher level reconstructed objects, such as particle trajectories or space points, have fully defined spatial coordinates and can be projected into each of the subdetector projections. This allows a very detailed visualization of the connection between reconstructed objects and the raw detector information that the objects were created from.

The set of projections is complemented by projections such as the V-Plot, which aims to provide an overview of the full event in a single projection, and several tools allowing the user to perform interactive analysis tasks such as invariant mass calculations or vertex fits. The combination of these tools in a single software package makes Atlantis an important tool for visualizing event data at every stage in the reconstruction process.

The last part of this thesis discusses the prospects for discovery of supersymmetry by searching for the decay  $\tilde{\chi}_2^0 \rightarrow Z^0 \tilde{\chi}_1^0 \rightarrow \mu^+ \mu^- \tilde{\chi}_1^0$  in the minimal supergravity model (mSUGRA). In this decay channel the next to lightest neutral supersymmetric particle (neutralino) decays into the lightest neutralino and a Standard Model  $Z$  boson, this  $Z$  boson in turn decays into two muons. The results presented are based on a Monte Carlo simulation study performed using the equivalent of  $2 \text{ fb}^{-1}$  of collected data at a center of mass energy of 10 TeV.

The branching ratio of the channel  $\tilde{\chi}_2^0 \rightarrow Z^0 \tilde{\chi}_1^0$  is determined most importantly by the mass difference between the two neutralinos. This difference has to be larger than the mass off the  $Z$  boson for the decay to be kinematically allowed, but it has to be smaller than the mass of the Higgs boson such that the much stronger decay  $\tilde{\chi}_2^0 \rightarrow h^0 \tilde{\chi}_1^0$  is not possible. In the region where these conditions are satisfied the branching ratio is

close to 1, while outside this region it decreases rapidly. To demonstrate the methods of the analysis, three signal points have been chosen inside this region.

The production of supersymmetric particles is dominated by squark/gluino pairs, the supersymmetric partners of the quarks and gluons. These heavy particles then decay via a cascade of ever lighter supersymmetric particles, eventually producing the lightest neutralino which is stable and escapes detection. This leads to events with typically a large number of energetic jets and a considerable energy imbalance due to the missing neutralino. The  $Z$  boson decaying into muons in the aforementioned decay channel provides a powerful way to suppress the backgrounds to this signal, leaving top pair production ( $t\bar{t}$ ) and normal  $Z$  boson production in conjunction with jets as the main backgrounds.

Two methods are discussed to observe evidence of  $\tilde{\chi}_2^0 \rightarrow Z^0 \tilde{\chi}_1^0 \rightarrow \mu^+ \mu^- \tilde{\chi}_1^0$  in the presence of these backgrounds. The first is a counting method fully based on the Monte Carlo simulation. A set of event selection cuts is derived that maximizes the significance of the signal events in the presence of the expected backgrounds. Since the significance of the observed signal is strongly determined by the possible fluctuations of the backgrounds, the uncertainty on the cross section of the background processes greatly reduces the discovery potential. Using this method the mSUGRA signal point with  $m_0 = 350 \text{ GeV}$ ,  $m_{1/2} = 275 \text{ GeV}$ ,  $A_0 = 0 \text{ GeV}$ ,  $\text{sign } \mu > 0$  and  $\tan \beta = 10$  can be observed with a statistical significance of 5.9.

To reduce the effect of the uncertainty on the background levels, a second method is introduced that performs a data-driven estimate of the number of background events. This method utilizes the fact that the most important background,  $t\bar{t}$ , produces  $\mu\mu/ee$  pairs and  $e\mu$  pairs in equal amounts. A control sample is created by repeating the signal selection, but replacing one of the muons by an electron. To separate the backgrounds from the signal, a fit is performed to the missing transverse energy spectrum using the control sample to constrain the  $t\bar{t}$  contribution. Any excess of events in the  $\mu\mu$  channel is attributed to the presence of supersymmetry. The much better estimate of the  $t\bar{t}$  background in this method leads to a much improved signal significance. For the aforementioned point, the signal significance increases to 9.0.

Based on these results, it can be concluded that the  $\tilde{\chi}_2^0 \rightarrow Z^0 \tilde{\chi}_1^0 \rightarrow \mu^+ \mu^- \tilde{\chi}_1^0$  channel appears to be an interesting channel for early supersymmetry searches. It provides a reasonable clean signature that is well visible above the background. In addition to that, the strong dependence on the mass difference between the next to lightest and lightest neutralino means that the (non-)presence of this channel can provide valuable information on the supersymmetry mass parameters.



# Samenvatting

De elementaire deeltjes en de fundamentele krachten tussen deze deeltjes worden beschreven door het Standaard Model van de deeltjesfysica. Dit is een enorm succesvolle theorie gebleken, met vele zeer nauwkeurige voorspellingen die bijna allemaal experimenteel bevestigd zijn. Het is vanwege dit succes dat het door het Standaard Model voorspelde Higgs deeltje heeft geleid tot een van de grootste zoektochten in de geschiedenis van de deeltjesfysica. Meerdere generaties botsingsexperimenten hebben limieten gesteld op de massa van het Higgs deeltje, maar tot dusver is het deeltje niet gevonden.

De Large Hadron Collider (LHC) bij het CERN laboratorium in Genève, Zwitserland is 's-werelds grootste en meest energetische deeltjesversneller. Deze versneller bevindt zich in een ondergrondse tunnel met een omtrek van 26,7 km en is ontworpen om bundels met protonen te laten botsen met een zwaartepuntsenergie van 14 TeV. Op de punten waar deze botsingen plaatsvinden bevinden zich grote deeltjesdetectoren die de sporen en eigenschappen meten van de deeltjes die bij de botsing vrijkomen. Door deze deeltjes nauwkeurig te analyseren kunnen fysici meer te weten komen over de processen die plaatsvonden tijdens de botsing.

Hoewel het Higgs deeltje een belangrijke motivatie is geweest voor de bouw van de LHC is het zeker niet de enige motivatie. In de afgelopen decennia zijn er experimentele observaties gedaan die erop wijzen dat het Standaard Model zoals we dat nu kennen nog niet compleet is. Zo zijn er bijvoorbeeld kosmologische waarnemingen die hebben aangetoond dat het Universum voor slechts 4,4% bestaat uit de “normale” materie die door het Standaard Model beschreven wordt. Nog eens 21,4% bestaat uit een onbekende vorm van materie die alleen gravitationele interacties heeft (donkere materie), en de rest wordt gevormd door een nog mysterieuze vorm van energie (donkere energie). Samen met enkele theoretische argumenten met betrekking tot aspecten van het Standaard Model die mathematisch onelegant zijn heeft dit geleid tot vele nieuwe theorieën voor de fysica voorbij het Standaard Model.

Een van die mogelijke nieuwe theorieën is supersymmetrie. Supersymmetrie voorspelt dat er voor elk deeltje dat we op dit moment kennen een supersymmetrisch partner

deeltje bestaat. Deze nieuwe deeltjes lossen een deel van de mathematische problemen in het Standaard Model op, als een van de supersymmetrische deeltjes echter stabiel is zou dit ook het bestaan van donkere materie kunnen verklaren.

De ATLAS detector is een van de twee algemene detectoren bij de LHC. De detector is ontworpen om een zo breed mogelijk spectrum van fysische processen waar te kunnen nemen. De detector, 40 m in lengte en 20 m in doorsnee, is gebouwd in lagen rondom het interactiepunt. Elke laag, of subdetector, meet andere eigenschappen van de uitgaande deeltjes waardoor deze kunnen worden gereconstrueerd en geïdentificeerd.

Een belangrijk instrument voor het debuggen van zowel de detector hardware als de reconstructie software is visuele inspectie van botsingen. Een deel van dit proefschrift beschrijft het Atlantis event display en de technieken die het gebruikt. Aangezien het totale aantal uitleeskanalen in de detector rond de 100 miljoen ligt is het maken van een visuele representatie van een botsing verre van triviaal.

Atlantis lost dit probleem op met de zogenaamde data georiënteerde projecties. In plaats van een drie dimensionale weergave van de detector gebruikt Atlantis een verzameling twee dimensionale projecties. Deze projecties zijn gebaseerd op de coördinaten die gemeten worden in de verschillende subdetectoren. De meeste subdetectoren meten slechts twee coördinaten, in dat geval levert het projecteren van de data langs de derde coördinaat de best mogelijke weergave van een bepaalde subdetector op. De gereconstrueerde objecten zoals deeltjessporen of gereconstrueerde punten in de ruimte hebben volledig gedefinieerde ruimtelijke coördinaten en kunnen op dezelfde wijze geprojecteerd worden. Dit maakt het mogelijk om de relatie tussen gereconstrueerde objecten en de ruwe informatie uit de detector waar de objecten uit opgebouwd zijn zeer gedetailleerd weer te geven.

De verzameling projecties in Atlantis wordt verder aangevuld met projecties zoals de V-Plot, waarmee gepoogd wordt een volledig botsingsevent in een enkel plaatje weer te geven, en diverse hulpmiddelen voor interactieve analysetaken zoals het berekenen van invariante massa of het fitten van vertices. De combinatie van al deze instrumenten in een enkel software pakket maken Atlantis tot een belangrijk hulpmiddel in alle stadia van het reconstructie proces.

Het laatste deel van dit proefschrift bespreekt de vooruitzichten voor de ontdekking van supersymmetrie door te zoeken naar het deeltjesverval  $\tilde{\chi}_2^0 \rightarrow Z^0 \tilde{\chi}_1^0 \rightarrow \mu^+ \mu^- \tilde{\chi}_1^0$  in het minimale supergravity model (mSUGRA). In dit vervalskanaal vervalt het op een na lichtste neutrale supersymmetrische deeltje (neutralino) in het lichtste neutralino en een Standaard Model  $Z$  boson, waarbij dit  $Z$  boson vervolgens weer vervalt in twee muonen. De resultaten die hier worden gepresenteerd zijn gebaseerd op een Monte Carlo

simulatie studie, gebruikmakend van het equivalent van  $2\text{ fb}^{-1}$  aan verzamelde data bij een zwaartepuntsenergie van  $10\text{ TeV}$ .

De vertakkingsverhouding van het verval  $\tilde{\chi}_2^0 \rightarrow Z^0 \tilde{\chi}_1^0$  wordt voornamelijk bepaald door het verschil in massa tussen de twee neutralino's. Dit verschil moet groter zijn dan de massa van het  $Z$  boson om dit verval kinematisch mogelijk te maken, maar het dient kleiner te zijn dan de massa van het Higgs boson zodat het veel dominantere vervalskanaal  $\tilde{\chi}_2^0 \rightarrow h^0 \tilde{\chi}_1^0$  niet mogelijk is. In het gebied waar aan deze condities voldaan wordt is de vertakkingsverhouding vrijwel 1, terwijl deze daarbuiten zeer snel afneemt. Om de methoden van deze analyse te demonstreren zijn drie signaal punten gekozen die aan deze condities voldoen.

De productie van supersymmetrische deeltjes vindt voornamelijk plaats in de vorm van squark/gluino paren, de supersymmetrische partners van de quarks en gluonen. Deze zware deeltjes vervallen vervolgens via een cascade van steeds lichtere supersymmetrische deeltjes in het stabiele lichtste neutralino, dat ontsnapt zonder gedetecteerd te worden. Dit leidt in het algemeen tot botsingsevents met een groot aantal energetische jets en een aanzienlijke energie onbalans vanwege het ontbrekende neutralino. Het  $Z$  boson dat vervalt in twee muonen in het eerder genoemde vervalskanaal biedt een effectieve methode om dit signaal van de achtergrond te scheiden, waarna top paar productie ( $t\bar{t}$ ) en normale  $Z$  boson productie in combinatie met jets overblijven als de belangrijkste achtergrondprocessen.

Twee methoden worden behandeld om het vervalskanaal  $\tilde{\chi}_2^0 \rightarrow Z^0 \tilde{\chi}_1^0 \rightarrow \mu^+ \mu^- \tilde{\chi}_1^0$  waar te nemen in de aanwezigheid van deze achtergronden. De eerste methode is een telmethode die volledig gebaseerd is op de Monte Carlo simulatie. In deze methode worden selectie criteria afgeleid die de statistische significantie van het signaal in de aanwezigheid van de achtergronden maximaliseren. Aangezien de significantie van het signaal wordt bepaald door de mogelijke fluctuaties in de achtergronden beïnvloedt de onzekerheid op de werkzame doorsnede van de achtergrondprocessen de maximaal haalbare significantie sterk. Door middel van deze methode kan het mSUGRA signaal punt met  $m_0 = 350\text{ GeV}$ ,  $m_{1/2} = 275\text{ GeV}$ ,  $A_0 = 0\text{ GeV}$ ,  $\text{sign } \mu > 0$  en  $\tan \beta = 10$  worden waargenomen met een statistische significantie van 5.9.

Om het effect van de onzekerheid in het niveau van de achtergrond te beperken wordt een tweede methode geïntroduceerd die gebruikt maakt van de data zelf om het achtergrondniveau te schatten. Deze methode is gebaseerd op het feit dat de belangrijkste achtergrond,  $t\bar{t}$ , in gelijke hoeveelheid  $\mu\mu/ee$  en  $e\mu$  paren produceert. Door de signaal selectie te herhalen, maar nu met een van de muonen vervangen door een electron wordt een controle sample verkregen. Om het signaal van de achtergrond te scheiden wordt

een fit gedaan van het missing energy spectrum, waarbij het controle sample wordt gebruikt om de  $t\bar{t}$  bijdrage vast te leggen. Als er een overschot van botsingsevents wordt waargenomen in het  $\mu\mu$  kanaal dan wijst dit op de aanwezigheid van supersymmetrie. De betere schatting van de  $t\bar{t}$  achtergrond die deze methode oplevert zorgt ervoor dat het eerder genoemde mSUGRA punt nu kan worden waargenomen met een statistische significantie van 9.0.

Op basis van deze resultaten kan worden geconcludeerd dat het vervalskanaal  $\tilde{\chi}_2^0 \rightarrow Z^0 \tilde{\chi}_1^0 \rightarrow \mu^+ \mu^- \tilde{\chi}_1^0$  mogelijk interessant is voor de eerste ontdekking van supersymmetrie. Het vervalskanaal heeft vrij duidelijke kenmerken die goed zichtbaar zijn boven de achtergrond. Bovendien betekent de sterke afhankelijkheid van het massaverschil tussen de twee lichtste neutralino's dat dit kanaal belangrijke informatie zou kunnen verschaffen over de massa parameters van supersymmetrie.

# Curriculum vitae

Eric Jansen was born on July 21<sup>st</sup> 1981 in Zevenaar, the Netherlands. He obtained his VWO diploma from the Candea College in 1999 and then went to Nijmegen to study physics and astronomy at the Radboud University. During the last year of his studies, he joined the experimental high-energy physics group to work on the visualization and alignment of the muon chambers in a testbeam setup for the ATLAS experiment.

He completed his master's thesis in 2005 and subsequently joined the experimental high-energy physics group in Nijmegen as a PhD student. During his PhD, he was based at CERN for 18 months where he worked on event visualization with groups from London and Birmingham, as well as on supersymmetry analysis within the Radboud University/Nikhef group. He was teaching assistant for several bachelor and master courses at the university, ranging from C-programming and a course on electronics to general relativity.

Since 2010, he has been working at CERN as a postdoctoral research associate for University College London. He is currently involved in the measurement of  $b$ -jets in first data and is responsible for the online event visualization in the ATLAS control room.